行政院國家科學委員會補助專題研究計畫成果報告

※※※※※※※※※※※※※※※※※※※※※※※※※※※※※※
※　　　　　　　　　　　　　　　　　　　　　　　　　　　　　※
※　　　　主客體偶合激發態質子轉移系統研究　　　　　※
※　　　　　　　　　　　　　　　　　　　　　　　　　　　　　※
※※※※※※※※※※※※※※※※※※※※※※※※※※※※※※

計畫類別：☑個別型計畫　　□整合型計畫
計畫編號：NSC 90 － 2113 － M － 002 － 055 －
執行期間： 90 年 8 月 1 日至 91 年 7 月 31 日

計畫主持人：周 必 泰
共同主持人：
計畫參與人員：葉慧君、吳國瑞、陳俊彥、許晉豪、邱朝順、周和均

本成果報告包括以下應繳交之附件：
　　　□赴國外出差或研習心得報告一份
　　　□赴大陸地區出差或研習心得報告一份
　　　□出席國際學術會議心得報告及發表之論文各一份
　　　□國際合作研究計畫國外研究報告書一份

執行單位：國 立 台 灣 大 學 化 學 系

中 華 民 國　　91 年 12 月 23 日
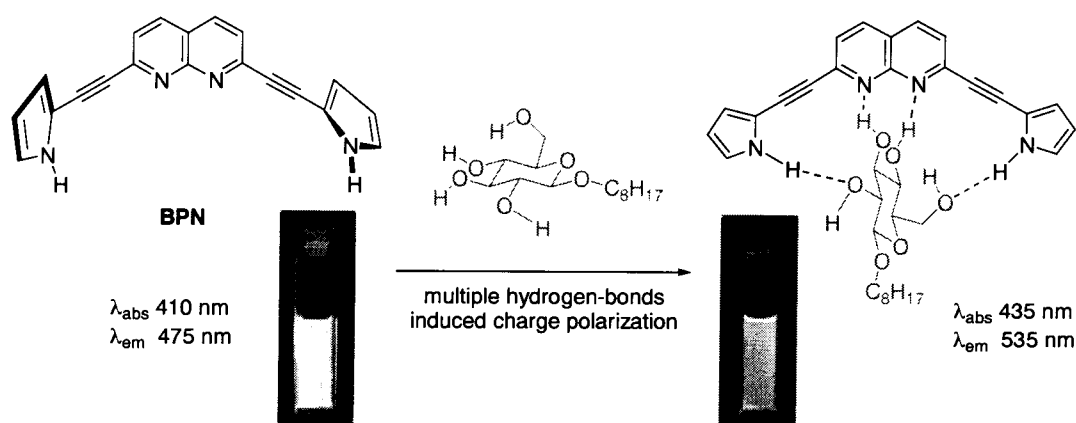
主客體偶合激發態質子轉移系統研究
NSC-90-2113-M-002-055
周必泰

成果報告

這一年多來我們在經過多年的努力後，已經可以generalized許多azaindoles以及adenine衍生物的質子轉移機制實際上是和amino-imino tautomerism在本質上是相同的。實驗上我們在2000年獲得許多直接的證據（***J. Phys. Chem. B*** **2000**, *104*, 7818, ***J. Phys. Chem. A*** **2000**, *104*, 8863）。這個機制亦引發我們和系上彭旭明老師合作設計一系列多環aminopyridine衍生物，利用自身proton donor/acceptor的雙性，得到多氫鍵複體，並藉由各種的光譜動力學來解析出環數和複體形成之間的熱力學對應關係（***J. Am. Chem. Soc.*** **2002**, *124*,
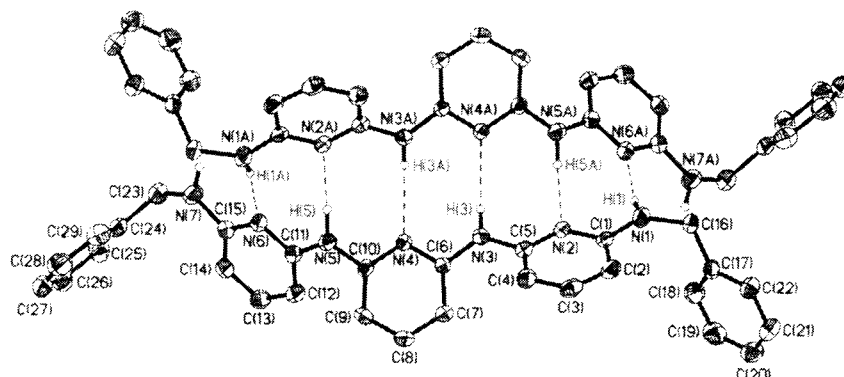
這結果在多氫鍵基礎研究上是一大突破，主因是一般氫鍵的結合並

不太考慮 entropy 的影響，但在多氫鍵的自組結合上當氫鍵數超過 n

＝ 4 後即變成主要的影響因素. 我們根據這原理進一步應用到多氫鍵

辨識上利用設計合成的分子 2,7-Bis-(1*H*-pyrrol-2-yl)ethynyl-1,8-

naphthyridine 成功的達到高靈敏具選擇性辨識 glucose 的效能 (*Org.*

Lett. **2002,** *4,* 3107).

BPN

λ_{abs} 410 nm
λ_{em} 475 nm

multiple hydrogen-bonds
induced charge polarization

C_8H_{17}

λ_{abs} 435 nm
λ_{em} 535 nm

在一系列的研究當中，我們也在國際間首次利用 3-取代基的影

響將azaindoles雙體的單晶解析出。一般azaindoles的單晶皆是

tetramer的形式，故在固態無法進行雙質子轉移。我們利用3-

methyl-7-azaindoles的雙體單晶做變溫(298-8 K)的steady-state 以及相

對的時間解析動力學在國際上第一個成功的解出激發態雙質子轉移

對azaindoles而言確實有能障在3-methyl-7-azaindole 氘取代中由質子

穿遂的理論中求出約為1.76 kcal/mol （***J. Phys. Chem. A 2002, 106,***

8006） ，更重要的是雙質子轉移機制應為one-step reaction， 這結果

也平息了近十年對7-azaindole雙體質子轉移動力學的爭執。

ΔE ~ 0.58 kcal/mol for 3MAI-h
~ 1.73 kcal/mol for 3MAI-d
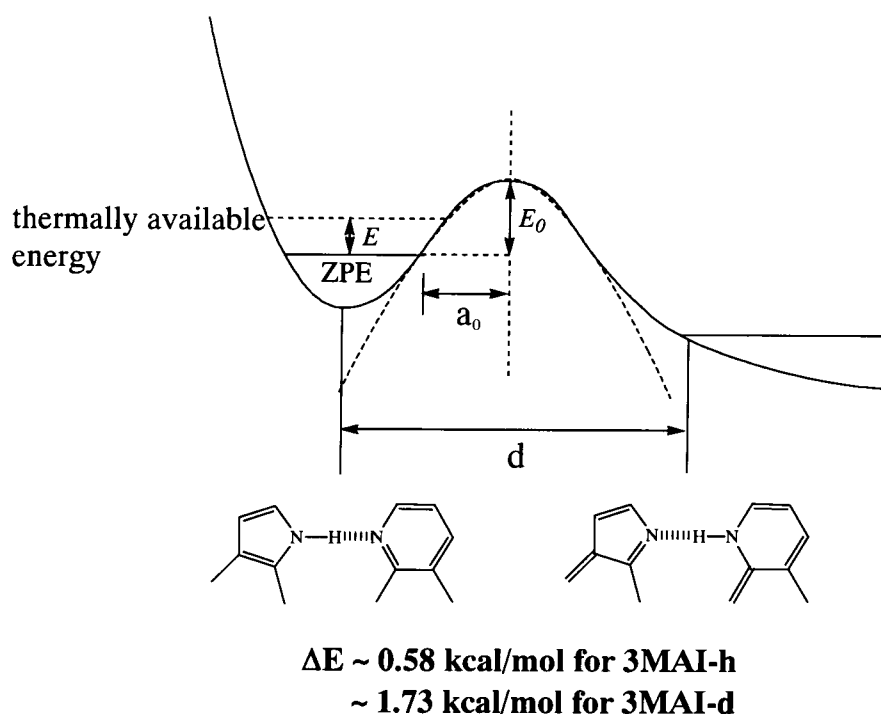
另一方面，2001年我們利用組合化學的新概念挑選出azaindoles的3-cyano衍生物(3CAI)來研究在水中的質子轉移動力學。為了mimic在生化環境中的突變現象，在physiological溶液中進行質子轉移是充分且必要的條件。我們利用時間解析光子計數偵測方式，解析出溶劑(水)催化激發態質子轉移速率在900 ps^{-1}左右,且有非常顯著的氘（deuterium）同位素效應(~3.5 ns^{-1})。利用溶劑偶合的動力學概念，我們清楚的導證出質子轉移中首先須經過一個快速的熱力學平衡步驟，達到一個所謂的溶質/溶劑最佳氫鍵狀態（環狀氫鍵結構）然後進行質子轉移。過去二十年來在azaindoles在水中的質子轉移一直無法被解析出的原因是質子轉移異構物的生成速率比消失速率快許多，致使tautomer的產生量微不足道。利用能階增大，熱緩解速率變慢的原理，3CAI 完全解析出這十幾年來在水中不正常光物理的謎團(***J. Am. Chem. Soc.*** **2001,** *123,* 3599)。我們最近已更進一步利用不同水的比例的時間解析雙質子轉移，求出平均每一個3CAI分子需要雙質子轉移時大約需要1.5 個水分子，顯示出應有1:1

以及1:2 3CAI/H$_2$O cyclic complex 參與雙質子轉移機制，我們經由

molecular dynamics及ab. initio的計算很精準的解釋了在溶液中幾個

H$_2$O catalyzed激發態質子轉移系統，證明我們實驗上的觀點和理論

的一致性。並藉由分子合成設計的突破來證明質子／電子偶和在質

子轉移反應方面的重要性。目前已將論文將送至***J. Am. Chem. Soc.***

發表。

我們另一個突破研究方向是利用超快速飛秒(femtosecond)雷射

系統，並且利用fluorescence upconversion的技術解析出β-carboline

的激發態內質子轉移動力學，在常溫其質子轉移速率約~1.2 ps^{-1}，

並結論β-carboline 激發態雙質子轉移能障約是1.5 kcal/mol左右，而

反應是由一些in-plane，large amplitude的振動模式所觸發。

今年我們激發態電子轉移的研究上也有相當大的突破由於並

不在這計畫主體中，此不詳述。*有關成果的詳細內容請參見下一*

頁2002年後發表(或已被接受即將發表)之12篇論文, 另三篇論文正

在審查中.

82 "Self-Complementarity of Oligo-α-aminopyridines: A New Class of Hydrogen-Bonded Ladders" M. K. Leung*, A. B. Mandal1, C. C. Wang G. H. Lee, S. M. Peng*, C. L. Cheng, G. R. Her, I. Chao, H. F. Lu, Y. C. Sun, P. T. Chou*_J. Am. Chem. Soc._ 2002, *124*, 4287-4297.

83 "Comment on "Highly Efficient White Organic Electroluminescence from a Double-Layer Device Based on a Boron Hydroxyphenylpyridine Complex" Pi-Tai Chou*, Chung-Chih Cheng, Chau-Shuen Chiou, Guo-Ray Wu *Angew. Chem. Int. Ed.* 2002, *41*, 2273.

84 "Proton-transfer tautomerism in 10-hydroxybenzo[*h*]quinolines; Heavy atom effects and non-hydrogen-bonded photorotamer formation in 77 K glassy matrices" Pi-Tai Chou*, Guo-Ray Wu, Yun-I Liu, Wei-Shan Yu and Chau-Shuen Chiou, *J. Phys. Chem. A* 2002, *106*, 5967.

85 "Excited-State Double Proton Transfer on 3-Methyl-7-Azaindole in a Single Crystal; Deuterium Isotope/Tunneling Effect" W. S. Yu, C. C. Cheng, C. P. Chang, G. R. Wu, C. H. Hsu, P. T. Chou*, *J. Phys. Chem. A* 2002, *106*, 8006-8012.

86 "Double Proton vs. Charge Transfer in 4-(N-substituted amino)-1H-Pyrrolo[2, 3-b]Pyridines" P. T. Chou*, Y. I. Liu, F. T. Hung, W. S. Yu_J. Phys. Chem. B_ 2002, *106*, 12713-12722..

87 "Syntheses and Spectroscopic Studies of Spirobifluorene-bridged Bipolar Systems; Photoinduced Electron Transfer Reactions " Y. Y. Chien, K. T. Wong*, P. T. Chou* and Y. M. Cheng *Chem. Commun.* 2002, 2874.

88 "2,7-Bis-(1*H*-pyrrol-2-yl)ethynyl-1,8-naphthyridine: A Highly Selective Fluorescent Probe for Glucopyranoside", Jen-Hai Liao, Chao-Tsen Chen*, He-Chun Chou, Chung-Chih Cheng, Pi-Tai Chou*, and Jim-Min Fang*, *Org. Lett.* 2002, *4*, 3107-3110.

89 "Photoinduced Electron Transfer Reactions Across Rigid Linear Spacer Groups of High Symmetry" K. Y. Chen, T. J. Chow,* P. T. Chou*, Y. M. Cheng and S. H, Tsai, *Tetrahedron Lett.* 2002, *43*, 8115.

90 "The Ground and Excited-State Acetic Acid Catalyzed Double Proton Transfer in 2-Aminopyridine" F. T. Hung*, W. P. Hu*, T. H. Li, C. C. Cheng and Pi-Tai Chou*, *J. Phys. Chem. A* 2002, *in press*.

91 "Dynamics of Ground-State Reverse Proton Transfer in the 7-Azaindole/Carboxylic acid System" W. P. Hu*,[1], R. M. You,[1] S. Y. Yen,[1] F. T. Hung,[2] W. S. Yu[3] and P. T. Chou*,[3] *Chem. Phys. Lett.* 2002, *in press*.

92 "Studies of the Triplet States of Proton-Transfer Tautomers in Salicylaldehydes" P. T. Chou*, C. Y. Wei, G. R. Wu and W. S. Yu, *Chem. Phys. Lett.* 2002, *in press*.

ARTICLES

Excited-State Double-Proton Transfer on 3-Methyl-7-azaindole in a Single Crystal: Deuterium Isotope/Tunneling Effect

Wei-Shan Yu,[†] Chung-Chih Cheng,[‡] Chen-Pin Chang,[‡] Guo-Ray Wu,[†] Chin-Hao Hsu,[†] and Pi-Tai Chou*,[†,§]

Department of Chemistry, National Chung-Cheng University, Chia-Yi, Taiwan, Republic of China, Department of Chemistry, Fu Jen Catholic University, Shin Chuang, Taiwan, Republic of China, and Department of Chemistry, National Taiwan University, Taipei, Taiwan, Republic of China

Unlike 7-azaindole consisting of the tetrameric configuration, 3-methyl-7-azaindole (3MAI) exists solely as intact double hydrogen-bonded dimeric forms in a single crystal. Both steady-state and time-resolved measurements down to 8.0 K reveal remarkable deuterium isotope effects on the rate of excited-state double proton transfer (ESDPT) in the N(1)-deuterated 3MAI (3MAI-*d*) single crystal. The rates of ESDPT for the 3MAI-*d* dimer resolved at <150 K are mainly governed by the proton tunneling mechanism. At <12 K, the nearly temperature-independent ESDPT dynamics lead us to qualitatively deduce a barrier height of ~1.73 kcal/mol for the 3MAI-*d* dimer. The results provide an ideal model to investigate the intrinsic ESDPT dynamics for 7-azaindole analogues in which the structural information is well documented.

I. Introduction

The excited-state double proton transfer (ESDPT)[1−3] in the 7-azaindole (7AI) dimer (Figure 1) has long been recognized as a prototype to mimic the photoinduced mutation of the DNA base pair.[4,5] Much research has focused on the dynamics of ESDPT, especially in solution phase.[6−10] Early studies have revealed that the rate of proton transfer is within $0.3-1.0 \times 10^{12}$ s^{-1} for the 7AI dimer in nonpolar solvents.[6,7] Recently, 0.2-ps and 1.1-ps dynamics were resolved by Takeuchi and Tahara[8] and first assigned to the rates of internal conversion and proton transfer, respectively, based on a concerted ESDPT model. Subsequently, Chachisvilis et al.[9] reported the 1-ps and 12-ps dynamics and interpreted on the basis of nonconcerted double proton-transfer reaction, but it was then claimed that the 12-ps component is due to the vibrational cooling.[10] Then, Fiebig et al. reassigned the 0.2-ps and 1-ps components to the two-steps double proton transfer[11] and concluded that both trajectories of the symmetric and asymmetric vibrational motion coupled with the solvent dynamics must be considered for the ESDPT in the solution phase. Only when the internal energy is small, such as at sufficiently low temperatures, can one examine the process of tunneling and nonconcertedness. Despite different viewpoints on the mechanism, both claimed observation of the kinetic isotope effects on the rate of ESDPT at ambient temperature.

Temperature-dependent ESDPT dynamics on 7AI were once suggested to be inaccessible due to the formation of thermodynamically more favorable oligomers at low temperature.[12,13]
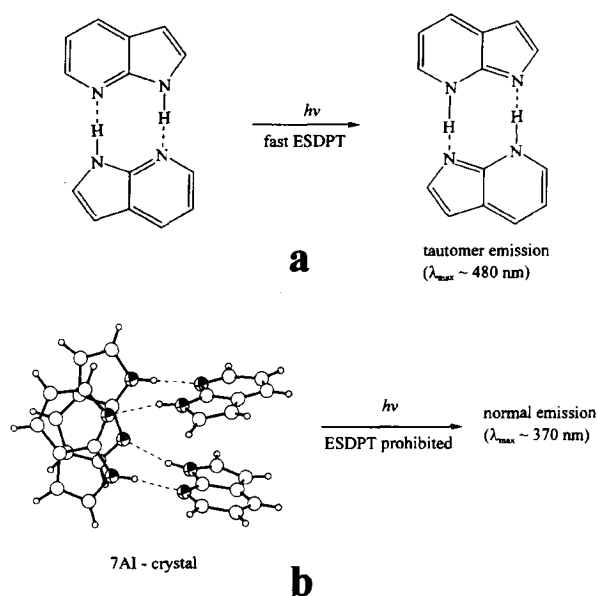

Figure 1. Differences in photophysical properties for the 7AI-associated structures: a. the dual hydrogen-bonded dimer (in solution) and b. tetramer (in a single crystal).

In a 77 K methylcyclohexane glass containing concentrated 7AI, the dominant steady-state emission maximum at ~460 nm was reported to originate from phosphorescence of the oligomers in which the cooperative double proton transfer is prohibited.[12,13] Recently, via a clever approach of applying sufficiently low 7AI concentrations, Catalán and Kasha[14] were able to resolve the dimeric form at low temperature and to study its corre-

* To whom correspondence should be addressed.
† Department of Chemistry, National Chung-Cheng University.
‡ Department of Chemistry, Fu Jen Catholic University.
§ Department of Chemistry, National Taiwan University.

3-Methyl-7-azaindole in a Single Crystal

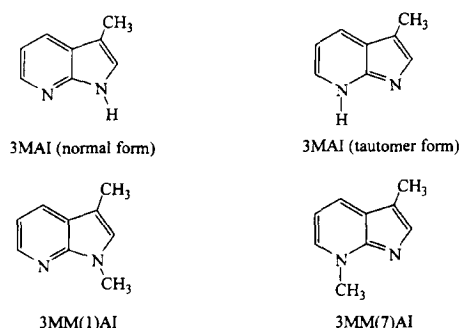*J. Phys. Chem. A, Vol. 106, No. 35, 2002* **8007**

Figure 2. Structures of 3MAI and their corresponding proton-transfer isomer as well as methylated derivatives.

sponding proton-transfer spectroscopy. Instead of the exclusive proton-transfer tautomer fluorescence in the 7AI dimer, the appearance of normal dimeric fluorescence at <200 K for the deuterated 7AI rendered a convincing deuterium isotope effect on the ESDPT dynamics[14] (hereafter N(1)-protonated and deuterated-7AI analogues are denoted by the suffix -h and -d, respectively). However, from the thermodynamic point of view, the hydrogen-bonding equilibrium should be dominated by the enthalpic factor and hence favors the oligomer formation at sufficiently low temperatures (e.g., 77 K and lower). It is thus rather difficult to determine the lower-limit temperature at which the existence of dual hydrogen-bonded dimer is free from the interference of oligomers. This in combination with possible perturbations resulting from solvent dielectric relaxation and/ or viscosity (e.g., solvent cage) may further smear and complicate the ESDPT dynamics.

From yet another approach, the hydrogen bond in the solid state can be well-characterized.[15] It has been demonstrated that the hydrogen-bonding structure in the single crystal provides an ideal model for investigating proton-transfer dynamics free from the solvent perturbation.[16,17] Unfortunately, the crystal structure of 7AI reveals tetrameric units of approximate S_4 symmetry, in which molecules are associated by means of four complementary N—H⋯N hydrogen bonds[18] (Figure 1b). As a result the cooperative ESDPT is prohibited. Recently, we have found that chemical modification at the C(3)-position of 7AI, forming 3-iodo-7-azaindole (3IAI), exhibited a dimeric structure in the single crystal. Steady-state approaches have shown the dominant ESDPT process even at 10 K for the 3IAI-h dimer, resulting in a unique tautomer emission.[19] Unfortunately, studies on ESDPT dynamics of 3IAI, particularly the deuterium isotope effect, were rather difficult due to its photochemical liability as well as fast S_1—T_1 intersystem crossing enhanced by the iodine heavy atom effect.[19,20] Thus, chemical modifications on 7AI suitable for investigating intrinsic ESDPT in the single-crystal became one of our focuses. In this study 3-methyl-7-azaindole (3MAI, Figure 2) was synthesized, of which the photostability is superior to that of 3IAI. Furthermore, unlike 3IAI where the association of iodine substituents induces strong perturbation due to the enhanced spin—orbit coupling and resonance effects, the much more inert methyl substitution in 3MAI provides an ideal model to mimic the intrinsic ESDPT dynamics of the 7AI dimer.

2. Experimental Section

2.1. Materials. *Synthesis of 3-methyl-7-azaindole (3MAI).* A precursor 7-azaindole-3-carboxaldehyde has to be prepared prior to the synthesis of 3MAI, which was synthesized according to the previous report.[21] Subsequently, a solution of semicarbazide

hydrochloride (1.35 g) and sodium acetate trihydrate (2.3 g) was added to a solution containing 7-azaindole-3-carboxalde-hyde (0.80 g) in 80 mL of boiling water. After the appearance of a transitory yellow coloration, a white solid gradually precipitated. The mixture was then heated on the steam-bath for ~15 min, then cooled to yield semicarbazone (1.1 g). Semicarbazone (1.1 g) was added to a solution containing sodium (0.96 g) in dry diethylene glycol (40 mL). The solution was refluxed at 205 °C under nitrogen atmosphere for 1h, and the mixture was cooled and poured into ~230 mL of water containing 3.1 g of glacial acetic acid. The resulting solution, which contained solid in suspension, was extracted with ether. The extracts were then washed with water, dried, and evaporated. The crude product was chromatographed on silica gel (eluent: ethyl acetate) to obtain 0.41 g (55%) 3MAI. ^{1}H NMR (400 MHz), δ 9.66 (s, 1H), 8.28 (dd, J = 1.6, 4.8 Hz, 1H), 7.89 (dd, J = 1.4, 7.6 Hz, 1H), 7.08(s, 1H), 7.04 (dd, J = 4.4, 8.0 Hz, 1H), 2.31(s, 3H). A single crystal of 3MAI-h with dimensions of ~0.50 × 0.45 × 0.45 mm³ was obtained by slow evaporation in a CH₃OH solution. To obtain the 3MAI-d single crystal, a similar recrystalization procedure was repeated three times in the CD₃OD solution under the N₂ atmosphere. After monitoring the disappearance of the N(1)—H proton in ^{1}H NMR (in CDCl₃), we concluded that ~95% of the N—H proton had been deuterated. The transfer of 3MAI-d to the cryostat was handled in a N₂ filled drybox to avoid the D/H exchange on the surface of the crystal.

The compound 1,3-dimethyl-7-azaindole (3MM(1)AI, Figure 2) was synthesized by adding sodium hydride (57%, 60 mg) to the THF solution containing 3MAI (0.15 g), followed by the addition of methyl iodide (30 mg). ^{1}H NMR (CDCl₃, 400 MHz), δ 2.32 (s, 3H), 4.10 (s, 3H), 7.0 (s, 1H), 7.17 (t, 1H), 8.05 (d, J = 7.2 Hz, 1H), 8.33 (d, J = 5.2 Hz, 1H). The compound 3,7-dimethyl-1H-pyrrolo[2,3-b]pyridine (3MM(7)AI, Figure 2) was synthesized by the reaction of 3MAI (0.12 g) and CH₃I (0.58 g) in THF under a N₂ atmosphere. NaOH (2.5 N, 3 mL) was then added and the mixture was stirred for ~20 min to obtain 3MM(7)AI (60 mg). ^{1}H NMR (CDCl₃, 400 MHz), δ 2.37 (s, 3H), 4.74(s, 3H); 7.37(t, 1H); 7.55(s, 1H); 7.98(d, J = 7.64 Hz, 1H); 8.34(d, J = 6.8 Hz, 1H).

2.2. Measurements. A closed-helium-cycle cryostat (Oxford, Model CCC1104) was used for the temperature-dependent study in the range of 298—8 K. The solid sample (i.e., single crystal) was placed tightly between two thin quartz plates that came into close contact with the Indium part of the cooling compart-ment to ensure maximum thermal conduction. The solid sample was excited by the fourth harmonic (266 nm) of the Nd:YAG laser under a front-face configuration. The resulting fluorescence was detected by an intensified charge coupled detector (ICCD, Princeton Instrument, Model 576G/1) coupled with a polychro-mator in which the grating is blazed with a maximum of 500 nm. Occasionally, to obtain excitation spectra the output of an Nd:YAG (355 nm, 8 ns, Continuum Surlite II) pumped optical parametric oscillator was tuned between 650 and 720 nm and was then frequency doubled by a BBO crystal to obtain a tunable 325—360 nm excitation frequency. The intensity of the laser pulse was measured by a joule meter, which was then normal-ized to obtain the corrected excitation spectra. A combination of filters was used in front of the exit polychromator to isolate the emission wavelengths of interest. The crystal orientation was 45° with respect to the direction of the excitation light.

Detailed fluorescence lifetime measurement has been de-scribed in the previous report.[22] Briefly, a third harmonic of the Ti—Sapphire oscillator (100 fs, 82 MHz, Spectra Physics)

8008 *J. Phys. Chem. A, Vol. 106, No. 35, 2002*

Yu et al.

a

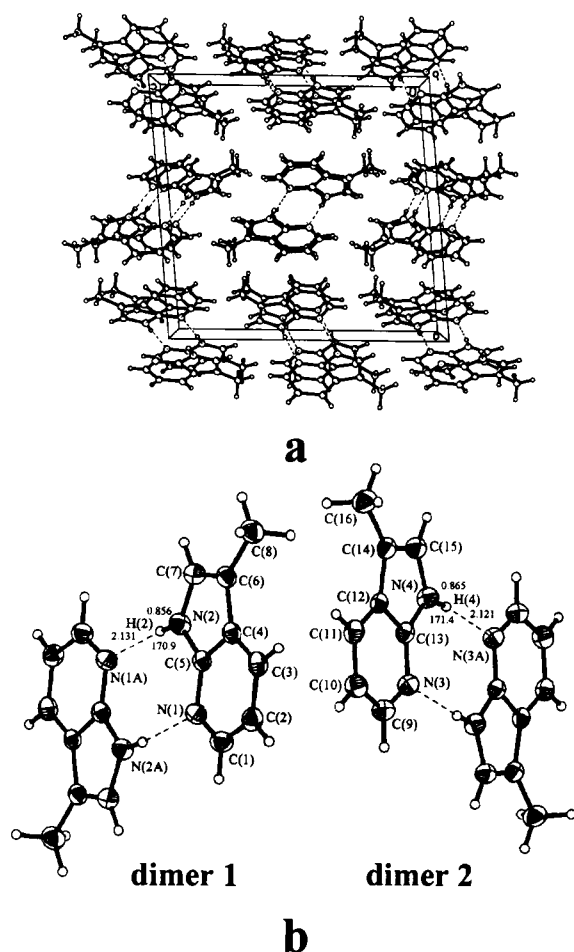**dimer 1**   **dimer 2**

b

Figure 3. a. The projection of 3MAI-*h* dimer in a unit cell of the single crystal. b. Two types of spatially arranged dimeric forms, specified as dimer 1 and 2. Bond distance and angle are in angstroms and degree (degrees), respectively.

coupled with a pulse picker (NEOS, model N17389) was used as an excitation source, giving a tunable wavelength in the range of 255–275 nm with a repetition rate of 8 MHz. An Edinburgh OB 900-L single-photon counter was used as a detecting system. The resolution of the time-correlated photon-counting system is limited by the detector response of ~30 ps. The fluorescence decays were analyzed by the sum of exponential functions with an iterative convolution method reported previously,[23] which allows partial removal of the instrument time broadening and consequently renders a temporal resolution of ~15 ps.

3. Results

3.1. Structure of 3MAI in a Single Crystal. As shown in Figure 3, the crystal structure of 3MAI-*h* is composed of a cyclic dimer via dual N—H⋯N hydrogen bonds. Parallel cyclic dimers are stacked via the interaction between their ring π-systems to form alternating slabs. The orientation of the parallel molecules in one slab is nearly perpendicular to those in adjacent slabs. The space group is *p2₁/C*, and *Z* = 8. Thus, there are two kinds of crystallographically independent molecules. Each of them forms a hydrogen-bonding dimer by the operation of the inversion center, while there is no symmetry relation between the two forms of dimers. To examine whether these two kinds

TABLE 1: Bond Lengths [Ångstroms] and Angle [Degrees] for 3MAI-h in a Single Crystal

Dimer 1			
N(1)—C(5)	1.332(2)	N(1)—C(1)	1.335(2)
N(2)—C(5)	1.365(2)	N(2)—C(7)	1.368(2)
C(1)—C(2)	1.387(2)	C(2)—C(3)	1.377(2)
C(3)—C(4)	1.394(2)	C(4)—C(5)	1.416(2)
C(4)—C(6)	1.425(2)	C(6)—C(7)	1.367(2)
C(6)—C(8)	1.502(2)	N(2)—H(2)	0.856(2)
N(1A)⋯H(2)	2.131(2)	N(1A)⋯N(2)	2.980(2)
C(5)—N(1)—C(1)	113.95(14)	C(5)—N(2)—C(7)	108.30(14)
N(1)—C(1)—C(2)	124.99(16)	C(3)—C(2)—C(1)	119.98(16)
C(2)—C(3)—C(4)	117.77(15)	C(3)—C(4)—C(5)	116.74(14)
C(3)—C(4)—C(6)	135.71(15)	C(5)—C(4)—C(6)	107.54(14)
N(1)—C(5)—N(2)	125.88(14)	N(1)—C(5)—C(4)	126.57(14)
N(2)—C(5)—C(4)	107.54(14)	C(7)—C(6)—C(4)	105.41(14)
C(7)—C(6)—C(8)	128.49(16)	C(4)—C(6)—C(8)	126.10(15)
C(6)—C(7)—N(2)	111.22(15)	N(1A)⋯H(2)—N(2)	170.90

Dimer 2			
N(3)—C(13)	1.335(2)	N(3)—C(9)	1.335(2)
N(4)—C(13)	1.366(2)	N(4)—N(15)	1.368(2)
C(9)—C(10)	1.390(2)	C(10)—C(11)	1.376(2)
C(11)—C(12)	1.386(2)	C(12)—C(13)	1.415(2)
C(12)—C(14)	1.434(2)	C(14)—C(15)	1.365(2)
C(14)—C(16)	1.500(2)	N(4)—H(4)	0.865(2)
N(3A)⋯H(4)	2.121(2)	N(3A)⋯N(4)	2.979(2)
C(13)—N(3)—C(9)	113.75(14)	C(13)—N(4)—C(15)	108.42(14)
N(3)—C(9)—C(10)	125.03(16)	C(11)—C(10)—C(9)	119.82(15)
C(10)—C(11)—C(12)	117.89(15)	C(11)—C(12)—C(13)	117.01(14)
C(11)—C(12)—C(14)	135.84(14)	C(13)—C(12)—C(14)	107.15(13)
N(3)—C(13)—N(4)	125.77(14)	N(3)—C(13)—C(12)	126.50(14)
N(4)—C(13)—C(12)	107.71(14)	C(15)—C(14)—C(12)	105.55(14)
C(15)—C(14)—C(16)	128.67(17)	C(12)—C(14)—C(16)	125.77(15)
C(14)—C(15)—N(4)	111.16(15)	N(3A)⋯H(4)—N(4)	171.4

of hydrogen-bonding dimers (specified as dimer 1 and dimer 2) are in the same circumstances in the single crystal, we have closely examined these two components in the X-ray data. The results of X-ray structural analyses are shown in Figure 3 and Table 1. The sameness in configuration of these two hydrogen-bonded dimers under different spatial arrangements can be supported by several critical bond lengths and angles shown in Table 1. For example, N(1A)⋯N(2) and N(1A)⋯H(2)N(2) were calculated to be 2.980 and 2.131 Å, respectively, for dimer 1. In addition, the angle of N(1A)⋯H(2)N(2) was calculated to be 170.9°. In comparison, similar results of 2.979 Å (N(3A)⋯N(4)) and 2.121 Å (N(3A)⋯H(4)N(4)) with an N(3A)⋯H(4)N(4) angle of 171.4° were obtained for dimer 2. These, in combination with similar bond angles and bond distances among the rest of the atoms between dimer 1 and 2 (see Table 1) indicate that within the standard deviation these two hydrogen-bonding dimers are in the same configuration and hence should behave in practically the same way.

To ensure the same crystal structure in both fluorescence and X-ray measurements, we first determined the structure by X-ray spectroscopy, followed by performing temperature-dependent fluorescence spectroscopy and dynamics of the same single crystal. During the fluorescence measurement an ultrahigh vacuum was maintained in the cryostat so that the D/H isotope exchange was negligible. In the case of 3MAI-*d*, great care was taken to perform the X-ray measurement in dry air conditions, and the results are attached in the Supporting Information. Comparing X-ray data shown in Table 1 and Supporting Information, it is obvious that single crystals of 3MAI-*h* and 3MAI-*d* used in the fluorescence studies are isomorphous. The X-ray crystallography was also performed at −80 °C. The results showed negligible differences in structure from that obtained at 295 K, indicating no temperature-dependent structural transformation for 3MAI in a single crystal.
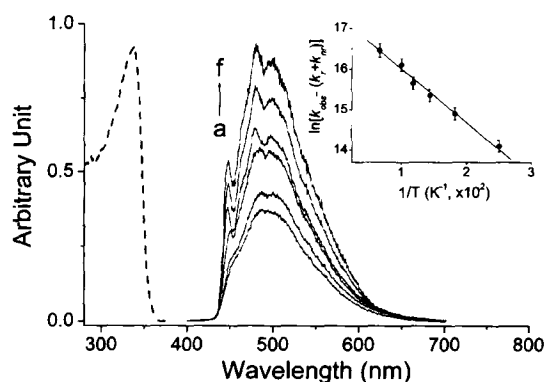
Figure 4. (—) The fluorescence of the 3MAI-*h* crystal as a function of temperature at **a.** 298, **b.** 240, **c.** 195, **d.** 90, **e.** 50, and **f.** 8 K. (- -) The absorption spectra of 3MAI-*h* in a solid form at room temperature. Inset: The plot of $\ln[k_{obs} - (k_r + k_{nr})]$ versus the reciprocal of the temperature.
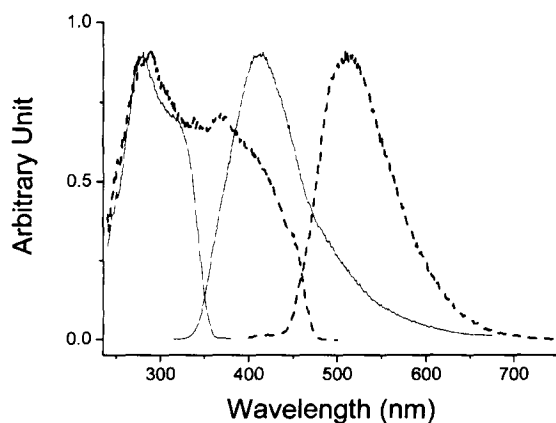

Figure 5. The fluorescence and fluorescence excitation spectra of 3MM(1)AI (—) and 3MM(7)AI (- -) in the crystal form at ambient temperature.

3.2. Spectroscopy and Dynamics in the Single Crystal. In contrast to a normal fluorescence ($\lambda_{max} \sim 370$ nm) observed in 7AI,[19] 3MAI-*h* in a single crystal exhibited a unique, large Stokes-shifted fluorescence ($\lambda_{max} \sim 500$ nm) throughout 298—8.0 K (Figure 4). In comparison, 3MM(1)AI (see Figure 2), which serves as a nonproton-transfer model for 3MAI, revealed a fluorescence with a peak maximum at 410 nm ($\tau_f \sim 0.9$ ns) in the solid state. Conversely, 3MM(7)AI, a model compound of the proton-transfer tautomer, exhibited room-temperature fluorescence maximized at 510 nm (Figure 5, $\tau_f \sim 2.1$ ns), of which the spectral and dynamical features resemble those observed in the 3MAI-*h* single crystal. These steady-state approaches unambiguously lead to two concluding remarks: 1. ESDPT is apparently operative in the 3MAI-*h* single crystal, resulting in a 500-nm proton-transfer tautomer emission. 2. Due to the lack of any observable normal emission, the rate of ESDPT must be fast even at a temperature of as low as 8.0 K. The latter viewpoint was supported by the subsequent time-resolved measurement. When monitored at the 500-nm emission band, the rise component of the tautomer fluorescence was too fast to be resolved ($\ll 15$ ps) throughout 298—8.0 K. Conversely, the decay of the tautomer emission can be well fitted by single exponential kinetics. The lifetime-revealed slight temperature dependence, varying from 2.7 (298 K) to 7.4 ns (8.0 K). From the standpoint of a temperature-independent
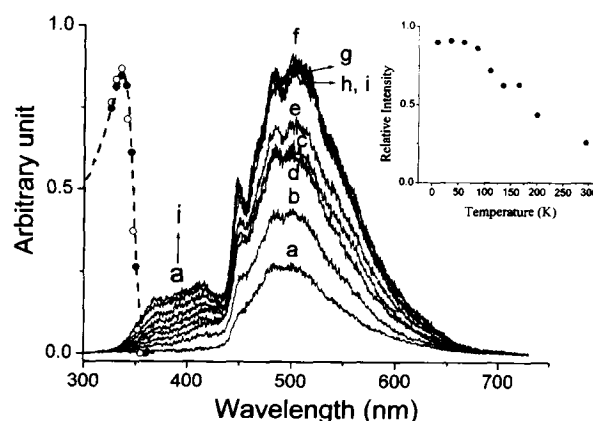
Figure 6. (—) The fluorescence of 3MAI-*d* crystal as a function of temperature at **a.** 298, **b.** 200, **c.** 165, **d.** 135, **e.** 110, **f.** 85, **g.** 35, **h.** 12, and **i.** 8 K. The excitation spectrum of the 3MAI-*d* crystal monitored at the F$_2$ (• •) and F$_1$ bands (o o). The excitation wavelength was tuned from 360 to 325 nm. (- -) The absorption spectra of 3MAI-*d* in a solid form at room temperature. Inset: The plot of tautomer emission intensity at 500 nm versus the temperature (in Kelvin).

fluorescence radiative decay rate, the result simply indicates the decrease in nonradiative deactivation rates (vide infra), which is consistent with the steady-state measurement, showing that the intensity of the tautomer emission increased as the temperature decreased (see Figure 4a—f).

Remarkable temperature-dependent fluorescence spectra were observed for the 3MAI-*d* single crystal. Dual emission became obvious at <200 K, in which a normal emission band (specified as the F$_1$ band) maximized at 395 nm gradually appeared (Figure 6). Conversely, the 500-nm tautomer emission (specified as the F$_2$ band) intensity versus temperature was slightly irregular (see insert of Figure 6); it increased upon decreasing the temperature from 298 to 190 K, followed by a decrease in the intensity at 150—120 K. At < 12 K the intensity as well as the ratio of dual emission was nearly temperature independent. By tuning the excitation wavelength, the resulting excitation spectrum, within experimental error, was independent of the emission wavelength monitored at either the F$_1$ or F$_2$ band, which is also effectively identical with the absorption profile (see Figure 6).

In accordance with the steady-state approach, a remarkable deuterium isotope effect on the ESDPT dynamics was also observed in the 3MAI-*d* single crystal. While the rise component of the F$_1$ band was beyond the instrument response of ~ 15 ps at 298—8.0 K, at <150 K the decay was resolvable and revealed drastic temperature dependence. As shown in Figure 7A and Table 2, the results clearly showed a decrease of the single-exponential decay rate constant, k_{obs}^N, upon decreasing the temperature. For instance, k_{obs}^N measured to be 3.8×10^9 s^{-1} at 8 K is smaller than that of 2.6×10^{10} s^{-1} measured at 100 K by ~ 7-fold. Conversely, the fluorescence dynamics of the F$_2$ band resolved at <150 K could only be fitted by dual exponential kinetics, which consist of a rise and a decay component as indicated by the fitted negative and positive preexponential factors, respectively. When monitored at >520 nm region free from the interference of the normal emission, the absolute values for both rise and decay preexponential factors, within experimental error, are similar (see Table 2). Slight differences are possibly attributed to the existence of ~5% of nondeuterated 3MAI-*h* in which fast ESDPT takes place. Therefore, the fitted preexponential value for the decay component is greater than that for the rise component. Table 2 also
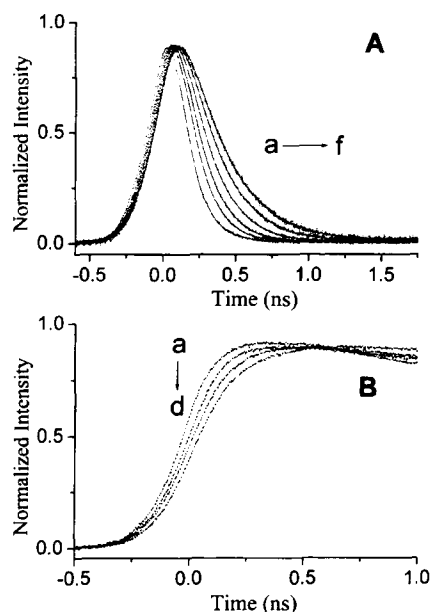
Figure 7. A. The time-dependent fluorescence decay dynamics of the 3MAI-*d* crystal monitored at the F$_1$ band (380 nm) at various temperatures of a. 150, b. 100, c. 70, d. 40, e. 20, and f. 10K. B. The rise dynamics of the F$_2$ band (520 nm) monitored at a. 190, b. 150, c. 70, and d. 10 K.

TABLE 2: Temperature-Dependent Fluorescence Relaxation Dynamics for 3MAI-*d* in a Single Crystal

temperature (K)	fluorescence lifetime				
	F$_1$ (λ_{max}=395 nm) τ (ns)	F$_2$ (λ_{max} = 500 nm)[a]			
		τ_1 (ns)	a_1	τ_2 (ns)	a_2
150	NA			6.66	1.000
100	0.038	0.040	−0.208	6.80	0.239
70	0.061	0.060	−0.205	7.15	0.235
40	0.127	0.130	−0.010	7.28	0.014
20	0.210	0.226	−0.011	7.33	0.017
10	0.260	0.260	−0.011	7.36	0.013
8	0.263	0.265	−0.011	7.38	0.015

[a] The F$_2$ band was fitted by dual exponential kinetics expressed as $F(t) = a_1e^{-\tau_1^{-1}t} + a_2e^{-\tau_2^{-1}t}$.

shows an interesting correlation between decay and rise components for the F$_1$ and F$_2$ bands, respectively, at various temperatures, in which the rise time of the F$_2$ band, within experimental error, was the same as the decay time of the F$_1$ band. In summary, the time-resolved measurement in combination with steady-state approaches led us to conclude that both F$_1$ (normal emission) and F$_2$ (tautomer emission) bands originate from the same ground-state species, i.e., the normal dimeric form, and the F$_1$ band is apparently the precursor of the F$_2$ band. Thus, the existence of a nonnegligible ESDPT barrier for the 3MAI-*d* dimer is apparent, and the deuterium isotope effect becomes significant on the rate of ESDPT at sufficiently low temperatures. The irregular temperature-dependent tautomer emission intensity for 3-MAI-*d* can thus be rationalized by two competing relaxation processes: 1. As the temperature decreases, the decrease of the ESDPT rate results in a smaller yield of population to the tautomer state, 2. The tautomer fluorescence quantum yield tends to increase at lower temperature due to the decrease of the rate of radiationless deactivations. Details on the relaxation dynamics will be discussed in the following section.
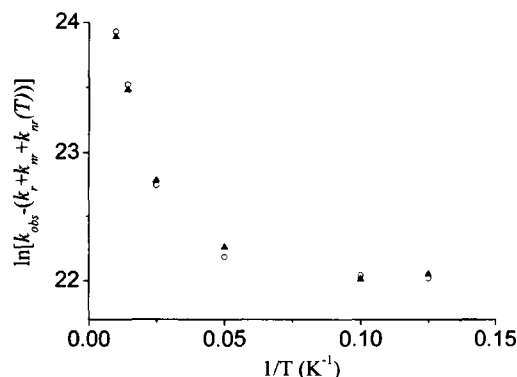

Figure 8. The plot of $\ln[k_{obs} - (k_r + k_{nr} + k_{nr}(T))]$ versus the reciprocal of the temperature for a. the decay of the F$_1$ band (▲) and b. rise kinetics of the F$_2$ band (○) in a 3MAI-*d* single crystal at ≤150 K. See text for the definition of $k_r + k_{nr} + k_{nr}(T)$.

4. Discussion

For the F$_2$ band, the observed temperature-dependent decay rate can be expressed as

$$k_{obs} = k_r + k_{nr} + k_{nr}(T) \qquad (1)$$

where k_{nr} denotes the temperature independent radiationless decay rate constant, possibly involving internal conversion, intersystem crossing, etc. The temperature-dependent radiationless decay rate constant $k_{nr}(T)$ can be further expressed as an Arrhenius type of thermally deactivated pathway, namely, $k_{nr}(T) = Ae^{-E_a/RT}$ where E_a is the barrier for the thermally deactivated process. As indicated by the time-resolved measurement, the lifetime of the tautomer emission (the F$_2$ band) was invariable at <12 K. Thus, it is reasonable to assume that $k_{nr}(T)$ is negligible, and the decay rate of 1.36×10^8 s^{-1} measured at, e.g., 8 K is equivalent to $k_r + k_{nr}$. The plot of $\ln[k_{obs} - (k_r + k_{nr})]$ versus the reciprocal of the temperature reveals straight-line behavior (see insert of Figure 4), supporting the validity of the thermal deactivation pathway for the tautomer emission. A best linear least-squares fit for the insert of Figure 4 gives E_a and the frequency factor to be 0.35 kcal/mol and 5.2×10^8 s^{-1}, respectively.

For the F$_1$ band, the observed temperature-dependent decay rate can be expressed as

$$k_{obs} = k_r + k_{nr} + k_{nr}(T) + k_{pt}(T) \qquad (2)$$

where $k_{nr}(T)$ denotes the thermally deactivated pathways except for the rate of proton transfer $k_{pt}(T)$. It is not feasible to obtain $k_r + k_{nr} + k_{nr}(T)$ for the normal emission (i.e., the F$_1$ band) of 3MAI in a single crystal because the dynamics of relaxation of the excited normal species are still dominated by the rate of double proton-transfer reaction even at low temperatures. Alternatively, we have attempted to obtain $k_r + k_{nr} + k_{nr}(T)$ values by performing the temperature-dependent relaxation dynamics of the 3MM(1)AI crystal in which the excited-state proton-transfer reaction is prohibited due to the lack of pyrrolic hydrogen. The results showed a slightly temperature-dependent decay rate from 4×10^8 s^{-1} (150 K) to 1.1×10^8 s^{-1} (8 K). Taking the k_{obs} value of the 3MM(1)AI crystal to be $k_r + k_{nr} + k_{nr}(T)$ for the 3MAI-*d* dimer, a plot of $\ln[k_{obs} - (k_r + k_{nr} + k_{nr}(T))]$ versus $1/T$ is shown in Figure 8. Apparently, the contribution of $k_r + k_{nr} + k_{nr}(T)$ is rather small in this plot simply due to its much smaller value in comparison to the rate of double proton-transfer reaction. If the ESDPT dynamics, $k_{pt}(T)$, mainly

3-Methyl-7-azaindole in a Single Crystal

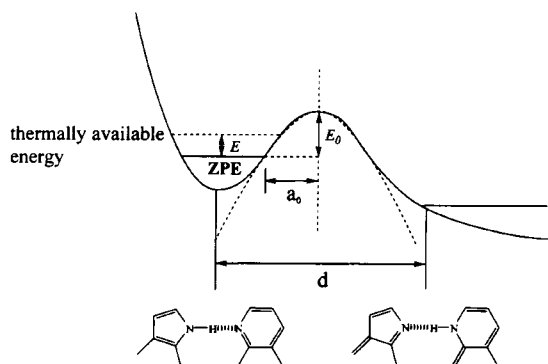*J. Phys. Chem. A, Vol. 106, No. 35, 2002* **8011**

Figure 9. A simplified one-dimensional PES regarding the ESDPT based on a bound-free potential curve. See text for the detailed description of notations.

incorporate a barrier crossing, i.e., a classical thermally activated process, straight-line behavior is expected upon plotting $\ln[k_{obs} - (k_r + k_{nr} + k_{nr}(T))]$ as a function of the reciprocal of the temperature. In contrast, the plot depicted in Figure 8a revealed an asymptote-like curve, which approached a constant value at <12 K. A similar pattern was also obtained when the rise dynamics of the F_2 band (i.e., the tautomer emission) are plotted against the reciprocal of the temperature (see Figure 8b).

The concave asymptote for the $k_{pt}(T)$-versus-$1/T$ plot in combination with a nearly constant ESDPT rate at 8−12 K led us to conclude that the dynamics of ESDPT for the 3MAI-*d* crystal are not governed by a thermally activated process, but more plausibly proceed through a proton-tunneling mechanism. To apply such theories, simplified approximation about the ESDPT potential energy surface (PES) is necessary. Both steady-state and dynamic approaches indicate that the ESDPT reaction in the 3MAI dimer is exergonic and irreversible. Accordingly, a simplified one-dimensional PES regarding the ESDPT can be represented by a bound-free potential curve shown in Figure 9, in which the proton-tunneling rate is given by

$$k_{\text{tunnel}} = \nu \exp\left[-\frac{\sqrt{2m}}{\hbar} \int_{-a_0}^{a_0} V(x)^{1/2}\, dx \right] \qquad (3)$$

where $V(x)$ is the energy barrier along the reaction coordinate, ν is the bound vibrational frequency, i.e., the reaction-coordinate frequency of the N−H (or N−D) mode in the case of 3MAI, m is the effective mass of the proton or deuterium, and a_0 is the distance from the center of the barrier to the classical vibrational turning points. Equation 3 can easily be evaluated if the potential barrier is further represented by a semiempirical, one-dimensional approach based on a parabolic shape-like activation energy, i.e., $V(x) = E_0(1 - x^2/a_0^2)$ where E_0 denotes the maximum barrier height above the zero point energy (ZPE). The resolvable ESDPT time scales for 3MAI-*d* are in the range of few tens to hundreds picoseconds. Thus, it is reasonable to assume a fast thermal equilibrium prior to the ESDPT reaction. Further support of this viewpoint can be given by varying the excitation wavelength from 255 to 275 nm, giving the same results on the ESDPT dynamics (not shown here). Accordingly, the tunneling rate for a molecule possessing thermal energy E above ZPE can thus be expressed as

$$k_{\text{tunnel}} = \nu \exp\left[-\frac{\pi a_0}{\hbar}\sqrt{2m(E_0 - E)} \right] \qquad (4)$$

A rough estimate of a_0 can be obtained from the average N−H⋯N hydrogen bond distances,[24] the estimated displacement of the proton transfer (denoted d in Figure 9) and classical turning points for the zero-point motion of the N−H (or N−D) harmonic vibration from the equilibrium position. For the case of 7AI, a_0, has been estimated to be 0.27 and 0.36 Å for N(1)−H and N(1)−D substituents, respectively.[3,11,25] The same a_0 values were used for 3MAI in the following calculation, assuming that methyl substitution at the C(3) position has negligible perturbation on the dimeric structure. Since the tunneling rate was measured to be independent of the temperature in the range of 8−12 K, the thermally available energy E can be neglected. Accordingly, the barrier height E_0 could be deduced by applying known reaction-coordinate frequency ν, effective mass m and the estimated a_0 value to eq 4. For the case of 3MAI-*d*, taking ν to be $\sim6.0 \times 10^{13}$ s^{-1} (~2000 cm^{-1}), an E_0 value of 605 cm^{-1} (1.73 kcal/mol) was thus deduced. At a relatively high temperature such as >20 K (see Figure 8) the available thermal energy is nonnegligible. The actual tunneling rate has to be calculated by the sum of all possible thermally populated states and is thus complicated. Given the difference in ZPE of ~400 cm^{-1} between N−H and N−D stretching, a barrier height of ESDPT was further deduced to be ~205 cm^{-1} (~0.58 kcal/mol) for the 3MAI-*h* dimer. Plugging E_0 of 205 cm^{-1}, $a_0^H = 0.27$ Å, $m = 1$, and $\nu = 2800$ cm^{-1} (8.4×10^{13} s^{-1}) to eq 4, the proton tunneling rate, k_{tunnel}, was calculated to be 4.3×10^{12} s^{-1} for 3MAI-*h* at <12 K. This time scale of $k_{\text{tunnel}}^{-1} = 233$ fs is too fast to be resolved by our picosecond time-correlated single photon counting system. On the basis of the energy barrier of 0.58 and 1.73 kcal/mol, respectively, rates of ESDPT for 3MAI-*h* and 3MAI-*d* were calculated to be negligibly small via a thermally activated process at <12 K.

Certainly, it should be noted that the proton tunneling could rarely be satisfactorily described as a one-dimensional process. The motion of atoms between which the proton is being exchanged may have a major effect on the tunneling rate.[26−32] Although the above results conclude a finite barrier to ESDPT, it is rather small, and subtle changes in the proton-transfer distance or energetics could have large effects on the proton-transfer rates. This recognition has led to the introduction of two-dimensional approaches in which the second dimension represents the effective motion of the other atoms during the proton-transfer reaction. Theoretical approaches[33−35] have revealed that the KIE (kinetic isotope effect) temperature dependence may be caused by thermally excited reactants and/or products that modulate the barrier width and shape. Although two-dimensional models may produce a more qualitative insight into the kinetic isotope effect and the temperature dependence of the transfer process, they still require the introduction of empirical parameters and thus cannot render quantitative predictions. For more precise quantitative work it is necessary to consider all degrees of freedom of the global system for an overall proton-transfer reaction.

At this stage, we are unable to differentiate the one-step versus two-step, nonconcerted ESDPT mechanism. Although the experimental results indicate a single decay and rise component for normal and tautomer emissions, respectively, it is also possible that ESDPT takes place via a two-step mechanism, and the rate in one of the steps is too fast to be resolved by the picosecond resolution. Alternatively, fluorescence upconversion with femtosecond resolution may provide valuable information. Unfortunately, the temperature-dependent study in the 3MAI single crystal is intrinsically difficult due to the photolysis and

or thermal reaction upon high repetition rate and high power laser excitation. Focus on this subject is currently in progress.

5. Conclusion

In conclusion, both steady-state and time-resolved measurements down to 8.0 K have revealed a remarkable deuterium isotope effect on the rate of ESDPT in the 3MAI-*d* single crystal. A barrier height of ESDPT of 1.73 and 0.58 kcal/mol was estimated for the 3MAI-*d* and 3MAI-*h* dimers, respectively, in a single crystal, and the ESDPT rates are mainly governed by a proton/deuterium tunneling mechanism. The results provide a prototype to mimic the intrinsic ESDPT dynamics of the 7AI-like dual hydrogen-bonded dimer with complete structural information, which are believed to bring up a broad spectrum of interest in the field of proton-transfer studies.

Supporting Information Available: X-ray data for 3MAI-*h* and 3MAI-*d*. This material is available free of charge via the Internet at http://pubs.acs.org.

References and Notes

(1) Taylor, C. A.; El-Bayoumi, M. A.; Kasha, M. *Proc. Nat. Acad. Sci. U.S.A.* **1969**, *63*, 253.

(2) Ingham, K. C.; Abu-Elgheit, M.; El-Bayoumi, M. A. *J. Am. Chem. Soc.* **1971**, *93*, 5023

(3) Ingham, K. C.; El-Bayoumi, M. A. *J. Am. Chem. Soc.* **1974**, *96*, 1674.

(4) Watson, J. D.; Crick, F. H. C. *Nature (London)* **1953**, *171*, 964.

(5) (a) Lowdin, P.-O. *Adv. Quantum Chem.* **1965**, *2*, 213. (b) Lowdin, P.-O. *Rev. Mod. Phys.* **1963**, *35*, 724.

(6) Hetherington, W. M., III; Micheels, R. H.; Eisenthal, K. B. *Chem. Phys. Lett.* **1979**, *66*, 230.

(7) Share, P.; Sarisky, M.; Pereira, M.; Repinec, S.; Hochstrasser, R. M. *J. Lumin.* **1991**, *48/49*, 204.

(8) Takeuchi, S.; Tahara, T. *Chem. Phys. Lett.* **1997**, *277*, 340.

(9) Chachisvilis, M.; Fiebig, T.; Douhal, A.; Zewail, A. H. *J. Phys. Chem. A* **1998**, *102*, 669.

(10) Takeuchi, S.; Tahara, T. *J. Phys. Chem. A* **1998**, *102*, 7740.

(11) Fiebig, T.; Chachisvilis, M.; Manger, M.; Zewail, A. H.; Douhal, A.; Garcia-Ochoa, I.; de La Hoz Ayuso, A. *J. Phys. Chem. A* **1999**, *103*, 7419.

(12) Bulska, H.; Chodkowska, A. *J. Am. Chem. Soc.* **1980**, *102*, 3259.

(13) Bulska, H.; Grabowska, A.; Pakula, B.; Sepiol, J.; Waluk, J.; Wild, U. P. *J. Lumin.* **1984**, *29*, 65.

(14) Catalán, J.; Kasha, M. *J. Phys. Chem. A* **2000**, *104*, 10812.

(15) Steiner, T. *Angew. Chem., Int. Ed.* **2002**, *41*, 48.

(16) Sekikawa, T.; Kobayashi, T.; Inabe, T. *Phys. Chem. A* **1997**, *101*, 644.

(17) Sekikawa, T.; Kobayashi, T.; Inabe, T. *J. Phys. Chem. B* **1997**, *101*, 10645.

(18) Dufour, P.; Dartiguenave, Y.; Dartiguenave, M.; Dufour, N.; Lebuis, A. M.; Belanger-Gariepy, F.; Beauchamp, A. L. *Can. J. Chem.* **1990**, *68*, 193.

(19) Chou, P. T.; Liao, J. H.; Wei, C. Y.; Yang, C. Y.; Yu, W. S.; Chou, Y. H. *J. Am. Chem. Soc.* **2000**, *122*, 986.

(20) After prolong photolysis of 3IAI the crystal turned yellow, accompanied by a decrease of the proton-transfer tautomer emission. Under the same experimental conditions similar photolysis reaction did not occur in 3MAI. It is thus believed that iodine substituents play a role for the observed photochemistry in 3IAI.

(21) Robison, M. M.; Robison, B. L. *J. Am. Chem. Soc.* **1956**, *78*, 1247.

(22) Chou, P. T.; Chen, Y. C.; Yu, W. S.; Chou, Y. H.; Wei, C. Y.; Cheng, Y. M. *J. Phys. Chem. A* **2001**, *105*, 1731.

(23) Demas, J. N.; Crosby, G. A. *J. Phys. Chem.* **1971**, *75*, 991–1024.

(24) Vinogradov, S. N.; Linnell, R. H. *Hydrogen Bonding*; Van Nostrand-Reinhold: New York, 1971: Chapter 7.

(25) Kim, S. K.; Breen, J. J.; Willberg, D. M.; Peng, L. W.; Heikal, A.; Syage, J. A.; Zewail, A. H. *J. Phys. Chem.* **1995**, *99*, 7421.

(26) Fernandez-Ramos, A.; Smedarchina, Z.; Siebrand, W.; Zgierski, M. Z.; Rios, M. A. *J. Am. Chem. Soc.* **1999**, *121*, 6280.

(27) Bicerano, J.; Schaefer, H. F., III; Miller, W. H. *J. Am. Chem. Soc.* **1983**, *105*, 2550.

(28) Siebrand, W.; Wildman, T. A.; Zgierski, M. Z. *J. Am. Chem. Soc.* **1984**, *106*, 4083, 4089.

(29) Smedarchina, Z.; Siebrand, W. *Chem. Phys.* **1993**, *170*, 347.

(30) Benderskii, V. A.; Goldanskii, V. I.; Makarov, D. E. *Phys. Rep.* **1993**, *233*, 195.

(31) Benderskii, V. A.; Makarov, D. E.; Wight, C. A. *Chemical Dynamics at Low Temperatures*: J. Wiley & Sons: New York, 1994: p 385.

(32) Liu, Y.-P.; Lu, D.-h.; Gonzalez-Lafont, D. G.; Truhlar, D. G.; Garrett, B. C. *J. Am. Chem. Soc.* **1993**, *115*, 7806

(33) Bruno, W. J.; Bialek, W. *Biophys. J.* **1992**, *63*, 689.

(34) Antoniou, D.; Schwartz, S. D. *Proc. Nat. Acad. Sci. U.S.A.* **1997**, *94*, 12360.

(35) Borgis, D.; Hynes, J. T. *J. Chem. Phys.* **1991**, *94*, 3619.

ARTICLES

Proton-Transfer Tautomerism in 10-Hydroxybenzo[*h*]quinolines: Heavy Atom Effects and Non-Hydrogen-Bonded Photorotamer Formation in 77 K Glassy Matrixes

Pi-Tai Chou,*,† Guo-Ray Wu,‡ Yun-I Liu,‡ Wei-Shan Yu,‡ and Chau-Shuen Chiou‡

Department of Chemistry, National Taiwan University, Taipei, Taiwan ROC, and Department of Chemistry, The National Chung-Cheng University, Chia Yi, Taiwan ROC

Received: January 30, 2002; In Final Form: April 18, 2002

The low-lying triplet states of 10-hydroxybenzo[*h*]quinoline (HBQ) and its halogenated derivatives 7,9-diiodo-10-hydroxybenzo[*h*]- quinoline (DIHBQ) in an excited-state intramolecular proton-transfer (ESIPT) process have been investigated. For DIHBQ, which is enhanced by the intramolecular heavy atom effect, the proton-transfer tautomer (i.e., the keto form) phosphorescence that is maximized at 735 nm ($\tau_p = 1.75 \mu s$) was resolved in a 77 K methylcyclohexane (MCH) glass. Further transient absorption and $^1O_2$ sensitization experiments allow us to deduce the population yield and radiative decay rate of the keto triplet state to be 0.85 and 8.8 s^{-1}, respectively. Upon increasing the excitation intensity, photolysis reactions were observed for both HBQ and DIHBQ in the MCH glass. The reversibility of the photolysis reaction throughout a thawing and freezing cycle led us to conclude that the rupture of an intramolecular hydrogen bond through the excessive energy dissipated does occur. The product exhibits a non-hydrogen-bonding type of enol emission that would otherwise be inaccessible in the hydrogen-bonded enol form because of the ultrafast ESIPT. Accordingly, relative energy levels in different spin manifolds are established during a proton-transfer cycle. The keto—enol reverse proton transfer in the lowest triplet manifold was estimated to be endergonic by ~7.42 kcal/mol.

1. Introduction

Insights into the dynamic features of a proton-transfer process have relied extensively on studies of the excited-state intramolecular proton-transfer (ESIPT) reaction.[1-11] The ESIPT process generally involves transfer of a hydroxyl (or amino) proton to an acceptor such as nitrogen or a carbonyl oxygen from a preexisting hydrogen-bonding configuration, forming a proton-transfer tautomer. This unusual photophysical property (i.e., a large amount of Stokes-shifted keto $S_1'\rightarrow S_0'$ fluorescence (hereafter, the prime sign denotes the proton-transfer tautomer)), with a possible change of the dipole moment in either magnitude or direction during the reaction, has been found to have many important applications. Prototypical examples include dye lasers, energy/data storage devices, optical switches,[12] biological probes,[13,14] metal-cation chelates,[15] and proton-transfer materials with future perspectives in electroluminescence.[16]

Among ESIPT molecules, 10-hydroxybenzo[*h*]quinoline (HBQ) (see Figure 1) has very unique spectral properties. The fused 7,8-benzoquinoline structure constrains the O—H- - - N geometry of the dominant enol form to a nearly perfect six-membered ring hydrogen-bonding configuration. Thus, HBQ possesses a very strong hydrogen bond in the ground state, as indicated by a 14.9-ppm downfield-shifted hydroxyl proton (in CDCl₃) in the ^{1}H NMR study.[17] For many ESIPT systems with relatively weak intramolecular hydrogen bonds, perturbation from polar, protic environments may modify the ESIPT dynamics, which

* Corresponding author. E-mail: chop@ccms.ntu.edu.tw.
† National Taiwan University.
‡ The National Chung-Cheng University.

HBQ(enol)　R: H, 　R₁: H
MBQ　　　　R: CH₃, R₁: H
DIHBQ　　　R: H, 　R₁: I
DIMBQ(enol)R: CH₃, R₁: I

Keto forms of HBQ and DIHBQ

a **b**

Proposed non-hydrogen-bonded enol forms of HBQ and DIHBQ

c
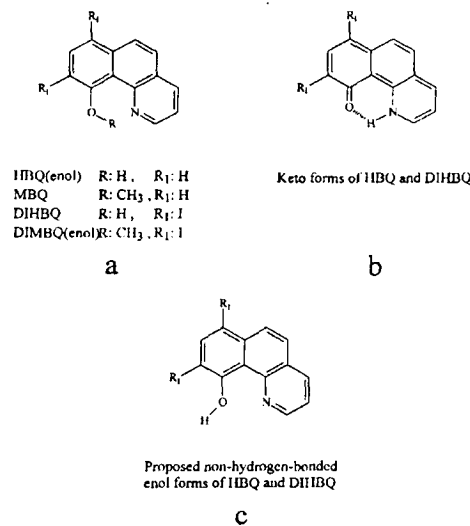
Figure 1. Structures of HBQ, DIHBQ, and their corresponding methoxyl derivatives.

may either be prohibited within the excited-state life span or proceed with a prerequisite of (protic) solvent reorganization.[18] In contrast, the occurrence of fast ESIPT in HBQ is essentially free from solvent perturbation. For example, studies in aqueous solution have shown the occurrence of ultrafast ESIPT in HBQ throughout a wide pH range of 0–14.[19] This data, in combination with HBQ's extraordinarily high photostability,[17] leads to

5968 *J. Phys. Chem. A, Vol. 106, No. 25, 2002*

Chou et al.

a variety of applications. In one approach, HBQ has been suggested to be a suitable radiation-hard scintillate because of its enormously large Stokes-shifted emission and high photostability.[20] Sytnik et al. used HBQ to probe enzyme kinetics and concluded that HBQ could distinguish static solvent-cage polarity from dynamical solvent dielectric relaxation.[13,14] Robert et al. used HBQ as a fluorescence probe to examine the influence of organized media such as cyclodextrins in aqueous solution.[21] Studies on comprehensive solvatochromism effects for HBQ in a variety of solvents have been performed by del Valle and Catalán[22] in an attempt to shed light on the use of HBQ in probing the solvent dynamics as well as in elucidating the biological environment. Recently, the femtosecond time-resolved approach has shown that the rate of ESIPT for enol HBQ is >150 fs^{-1}. The results, in combination with the lack of a deuterium isotope effect on the ESIPT dynamics, suggest a barrierless ESIPT reaction along the potential energy surface.[23]

Despite extensive information regarding ESIPT properties in the singlet-state manifold, to our knowledge, all attempts to resolve the spectroscopy and dynamics of triplet states for HBQ are still obscured. The peak maximum of the keto-tautomer fluorescence, depending on the solvent polarity, was reported to be >580 nm.[17,19,21-23] One thus expects the $T_1'-S_0'$ energy gap for HBQ to be in the far-visible or near-infrared (NIR) regions. On one hand, correlation of the forbidden triplet–singlet radiative decay rate constant k_P generally obeys the relationship $k_P \propto |D|^2 \bar{\nu}^3$, where D is the transition moment length and $\bar{\nu}$ is the average wavenumber of the transition.[24] k_P is then proportional to E_T^3, where E_T denotes the energy gap between the T_1' and S_0' states and becomes smaller when E_T decreases to the NIR region. On the other hand, a theory pertaining to the radiationless decay derived by Siebrand concludes that the intramolecular radiationless deactivation should increase with the decreasing energy gap of the transition.[25] For many ESIPT molecules in particular, vibrational modes associated with intramolecular hydrogen bonds usually act as good quenchers for the tautomer emission.[26] Thus, detecting phosphorescence in the NIR region, especially for the ESIPT molecules, may be hampered by the dominant $T_1' \rightsquigarrow S_1'$ radiationless deactivation process.

In this study, the spectroscopy and dynamics of triplet states for HBQ and its halogenated derivatives were investigated. On the basis of intramolecular heavy atom effects,[27] in combination with an ultrasensitive detecting system, keto-tautomer phosphoresce in the NIR region was resolved in 7,9-diiodo-10-hydroxybenzo[h]quinoline (DIHBQ, Figure 1). Intriguing photolysis reactions were also observed for both HBQ and DIHBQ in a 77 K MCH glass, giving rise to the enol-like emission that would otherwise be unobtainable. As a result, relative energy levels in different spin manifolds during a proton-transfer cycle were thus established.

2. Experimental Section

2.1. Materials. 10-Hydroxybenzo[h]quinoline (HBQ) (TCI Inc) was twice recrystallized from cyclohexane followed by purification using column chromatography (2:1 ethyl acetate/hexanes). The purity was checked by using the fluorescence excitation spectrum. Methylcyclohexane (Aldrich) was of spectrograde quality and was used without further purification. No fluorescence or phosphorescence impurities were detected in the blank solvent at either room temperature or 77 K.

DIHBQ was synthesized by adding a solution containing HBQ (0.01 mol) and glacial acetic acid (4 mL) in chloroform

(10 mL) to a solution of iodine (0.02 mol in 20 mL methanol) for a period of 1 h. The precipitate was collected and neutralized with sodium carbonate to obtain DIHBQ. ^{1}H NMR (CDCl$_3$, 400 MHz): δ 7.659 (t, $J = 12.72$ Hz, 1H), 7.762 (d, $J = 9.32$ Hz, 1H), 8.084 (d, $J = 8.8$ Hz, 1H), 8.338 (d, $J = 8.4$ Hz, 1H), 8.572 (s, 1H), 8.853 (d, $J = 4.6$ Hz, 1H), 16.705 (s, 1H). A general methylation procedure incorporating methyliodide into the basic DIHBQ solution to obtain 7,9-diiodo-10-methoxybenzo[h]quinoline (DIMBQ) failed because of the detachment of iodine from DIHBQ at the reflux temperature. Alternatively, 10-methoxybenzo[h]quinoline (MBQ) was first synthesized through the methylation of HBQ (0.5 g).[19] DIMBQ was then obtained by a similar iodination procedure. Crude DIMBQ was further purified by column chromatography (eluent: ethyl acetate). ^{1}H NMR (CDCl$_3$, 400 MHz): δ 4.512 (s, 3H), 7.489 (d, $J = 8.0$ Hz, 1H), 7.767 (d, $J = 8.5$ Hz, 1H), 7.952 (t, 1H), 8.097 (s, 1H), 8.868 (d, $J = 7.6$ Hz, 1H), 9.630 (d, $J = 5.2$ Hz, 1H).

2.2. Method. Steady-state absorption and fluorescence spectra were recorded by a Varian (Cary 3E) spectrophotometer and a Hitachi (F4500) fluorimeter, respectively. Detailed fluorescence lifetime measurements have been described in the previous report.[23] Briefly, the second harmonic of the Ti–sapphire oscillator (100 fs, 82 MHz, Spectra Physics) coupled with a pulse picker (NEOS, model N17389) was used as an excitation source, giving a tunable wavelength in the range of 380–410 nm with a repetition rate of 8 MHz. An Edinburgh OB 900-L single photon counter was the detector, giving a temporal resolution of ~15 ps. For time-resolved phosphorescence measurements, an Nd:YAG (355 nm, 8 ns, Continuum Surlite III) pumped optical parametric oscillator was tuned between 620 and 800 nm and was then frequency-doubled by BBO crystals to obtain a 310–400-nm excitation frequency. The resulting luminescence was then detected by a red-sensitive intensified charge coupled detector (ICCD, Princeton Instrument, model 576G/1) coupled with a polychromator in which the grating is blazed with a maximum at 700 nm.

The transient absorption experiment was performed by using a modified flash lamp (EG&G model LS-1130) as a white-light probe pulse. A cylindrical lens was used to shape the pumped Nd:YAG 355-nm pulse to a rectangular size of 10×2 mm^2. The white-light probe pulse was collected by an optical fiber, collimated by a 5-cm focal-length lens, and skimmed to a 2×2-mm^2 rectangle before entering the sample cell. The pump and probe pulses were crossed at a 90° angle, with an overlapping distance of 10 mm. The probe pulse, after passing through the sample solution, was focused on the entrance slit (~700 μm) of the ICCD system.

Steady-state O$_2$ ($^1\Delta_g \rightarrow {}^3\Sigma_g^-$ (0, 0)) emission spectra in the region of 1274 nm were obtained by exciting the sample solution under a front-face excitation configuration using an Ar ion laser (362 nm, Coherent Innova 90). The emission was then sent through an NIR Fourier transform interferometer (Bruker Equinox 55) and detected by a liquid nitrogen-cooled Ge detector (403X, Applied Detector Corporation). For the time-resolved study, the third harmonic (355 nm) of the Nd:YAG laser (Continuum Surlite I) was used as an excitation light source. An NIR fast-response photomultiplier (Hamamatsu model R5509–72) operated at -80 °C was used as a detecting system. The response time of the overall detecting system was determined to be ~20 ns, as measured by the response of the system to a 1064-nm Nd:YAG laser pulse of 8-ns duration. To select the emission of interest, a combination of interference and band-pass filters was used.
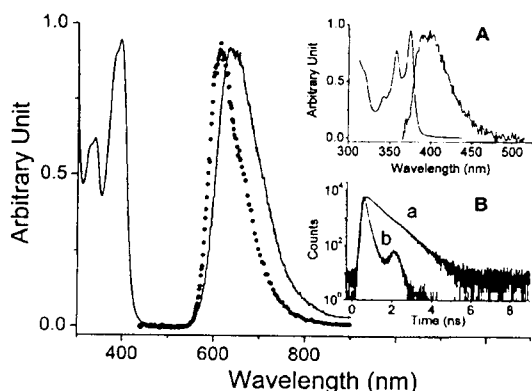
Proton-Transfer Tautomerism in Quinolines

J. Phys. Chem. A, Vol. 106, No. 25, 2002 **5969**

Figure 2. Absorption and emission spectra of DIHBQ (—) in MCH at 298 K. Emission spectrum of DIHBQ (•••) in a 77 K MCH glass. (A) Absorption and emission spectra of DIMBQ in MCH at 298 K. (B) Fluorescence decay at 610 nm for DIHBQ at 77 K (a) and the system response function (b) (λ_{ex} = 395 nm).

In the oxygen-dependent study, the molar ratio of oxygen in solution was determined by Henry's law from known O_2 concentrations for various solvents at 760 Torr.[28]

3. Results and Discussion

3.1. Photophysics of HBQ and 7,9-DIHBQ.

Figure 2 shows the room-temperature absorption and emission spectra of DIHBQ in MCH. The $S_0 \rightarrow S_1$ ($\pi\pi^*$) absorption exhibits an onset at ~440 nm with a peak maximum at 395 nm ($\epsilon_{395} \approx 8100$ M^{-1} cm^{-1}). The luminescence is mainly characterized by a largely Stokes-shifted emission band maximized at 640 nm. The excitation spectrum is independent of the monitored emission wavelength and is effectively identical to the absorption profile (not shown here). Conversely, DIMBQ, which is considered to be a non-proton-transfer model with an electronic configuration similar to that of DIHBQ, exhibits a very weak, normal Stokes-shifted fluorescence maximum at ~400 nm (see inset A of Figure 2). Thus, similar to what was concluded in HBQ,[17,19,23] ESIPT is operative in DIHBQ, resulting in keto-tautomer emission (see Scheme 1).

Not detecting any enol emission for DIHBQ is consistent with the occurrence of rapid proton-transfer tautomerism in the lowest singlet excited state. This viewpoint is further supported by the fluorescence lifetime measurement where the keto-tautomer emission is well-fitted by a single-exponential decay rate of 220 ps^{-1}, whereas the rise time is beyond the system response of 15 ps. On the basis of approximately unity ESIPT efficiency for DIHBQ, the quantum yield of the keto-tautomer emission was determined to be 1.8 × 10^{-3} by comparing its emission intensity to that of HBQ ($\tau_f \approx 300$ ps, $\Phi_{obs} \approx 2.1 \times 10^{-3}$ in cyclohexane[23]). In comparison to the spectra of HBQ, both absorption and fluorescence spectra of DIHBQ exhibit significant red shifts of ~1000 and 400 cm^{-1}, respectively, in cyclohexane. The bathochromic shift could be qualitatively rationalized by the electron-donating properties of iodine substituents through the resonance effect, reducing the $\pi \rightarrow \pi^*$ energy gap in both the enol and keto species.

In a 77 K MCH glass, an ESIPT reaction with an ultrafast rate still takes place in DIHBQ, as was supported by two observations: (1) a unique keto-tautomer fluorescence peak that was maximized at 610 nm ($\Phi_f \approx 6.8 \times 10^{-3}$) was resolved in a steady-state approach (Figure 2) and (2) the fluorescence lifetime was deduced to be ~600 ps, whereas the rise time is still beyond our system response of 15 ps (see inset B of Figure
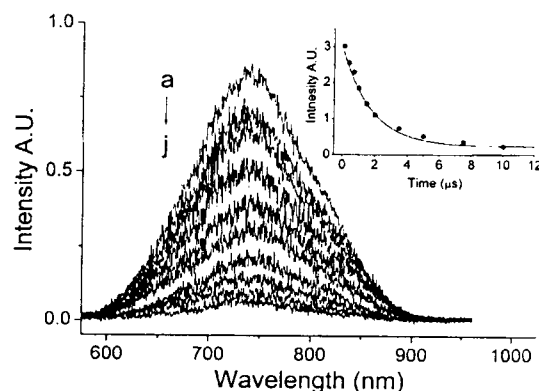

Figure 3. Time-dependent $T_1' \rightarrow S_0'$ phosphorescence spectra of DIHBQ in a 77 K MCH glass acquired at various delay times of (a) 100 ns, (b) 400 ns, (c) 700 ns, (d) 1.0 μs, (e) 1.5 μs, (f) 2.0 μs, (g) 3.5 μs, (h) 5.0 μs, (i) 7.5 μs, and (j) 10 μs with respect to the pump pulse. Inset: Decay profile of 735-nm emission intensity. Note that the spectral feature at >800 nm may not be authentic because of the nonlinear spectral response of the ICCD.

SCHEME 1: Relative Energy Levels (in cm^{-1}) for the Enol and Keto Tautomers of DIHBQ Estimated from Either Experimental or Theoretical Approaches[a]

DIHBQ(enol form)   DIHBQ(keto form)
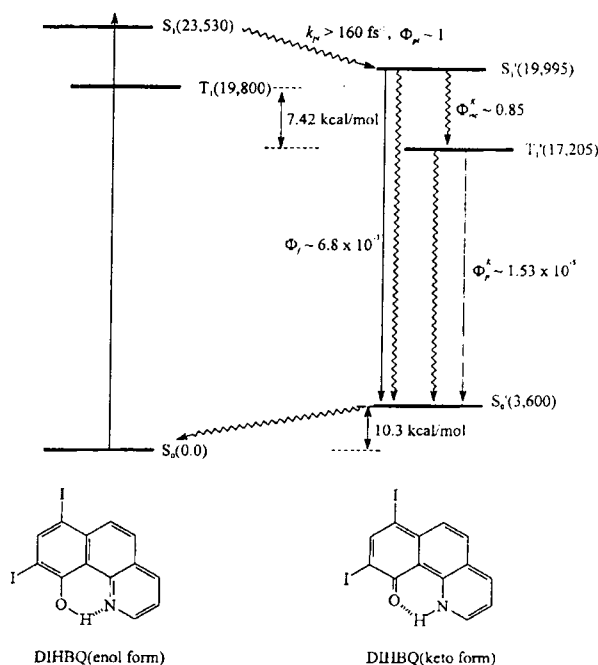
[a] See text for a detailed description.

2). The fluorescence peak maximum of 610 nm is blue-shifted by ~800 cm^{-1} with respect to that observed at 298 K. A similar hypsochromic shift has been reported for HBQ in a 77 K MCH glass[17] and was tentatively attributed to the solvent cage effect. To obtain the presumably ultraweak $T_1' \rightarrow S_0'$ phosphorescence, the high-voltage gate of the ICCD was operated at a delay time of >50 ns to eliminate the fast decay component attributed to the keto-tautomer fluorescence. Upon low-power excitation (<1 mJ/cm², vide infra), phosphorescence at >600 nm was resolved, and its spectral evolution as a function of the delay time is shown in Figure 3a—j. The long-lived emission that is maximized at 735 nm undergoes single-exponential decay kinetics, of which the lifetime was fitted to be 1.75 μs ($k_{obs} \approx 5.7 \times 10^5$ s^{-1}, see

inset of Figure 3). The excitation spectrum that is tuned in the 380–405 nm region revealed the same spectral profile as that monitored at the keto-tautomer fluorescence (not shown here), indicating that both emissions originate from a common ground state. In comparison, DIMBQ exhibited a phosphorescence band that was maximized at 495 nm ($\tau_p \approx 1.2$ ms) in a 77 K MCH glass. The results unambiguously show that the 735-nm emission originates from the keto-tautomer $T_1'{\to}S_0'$ phosphorescence. By opening the ICCD gate width as wide as 10 μs to cover >99.9% of the phosphorescence decay, the observed yield of keto-tautomer phosphorescence, Φ_{obs}^K, was measured to be 1.3 × 10^{-5}. Under identical experimental conditions, our attempts to resolve the keto-tautomer phosphorescence for HBQ failed. It is thus reasonable to conclude that the phosphorescence yield of HBQ, if it exists, should be ≪1.3 × 10^{-5}.

Theoretically, the observed yield for the keto-tautomer phosphorescence can be expressed as $\Phi_{obs}^K = \Phi_{pt}\,\Phi_{isc}^K\,\Phi_p^K$ where Φ_{pt} denotes the yield of the ESIPT and is assumed to be ~100% efficient because of the ultrafast rate of ESIPT, Φ_{isc}^K is the population yield of the keto-tautomer triplet state, and Φ_p^K represents the keto phosphorescence yield and is equivalent to k_r^p/k_{obs}^p where k_r^p and k_{obs}^p, respectively, denote the radiative and measured decay rate constants of the keto phosphorescence. The quantitative measurement of Φ_{isc}^K by using triplet–triplet energy transfer to an organic molecule is not feasible for DIHBQ mainly because of the lack of sensitizers with known low-lying triplet-state energies and absorption cross sections that could allow energy evaluation from quenching (i.e., energy transfer) experiments. Alternatively, we performed an oxygen photosensitization experiment to circumvent this obstacle. This method is feasible in determining the yield of the triplet state of organic molecules if the following assumptions hold: (i) The T_1-S_0 energy gap is greater than the energy required to sensitize singlet oxygen (O_2 $^1\Delta_g{\to}^3\Sigma_g^-$ (0,0) of ~7850 cm^{-1}). (ii) Sensitization of oxygen by the S_1 state is negligible because of its relatively much shorter life span. (iii) The decay of the triplet state should be dominated by the $T_1-^3O_2$ energy transfer. Assumptions (i) and (ii) hold for DIHBQ because of the keto $T_1'-S_0'$ energy gap of ~13 605 cm^{-1} and fast decay of the keto-tautomer emission at room temperature (e.g., ~220 ps in MCH at 298 K).

Conventionally, the O_2 quenching dynamics for the triplet state can be obtained through the triplet–triplet absorption measurements as a function of the added O_2 concentration. Figure 4 depicts the transient absorption spectra of DIHBQ in degassed methylcyclohexane. The transient absorption maximum at 475 nm undergoes a fast single-exponential decay with a rate of 8.5 × 10^5 s^{-1} (see inset A of Figure 4). The drastic quenching dynamics of the transient absorbance upon adding O_2 helped us to assign the 475-nm transient to the triplet–triplet absorption unambiguously. Inset B of Figure 4 shows a plot of decay rate as a function of O_2 concentration. From the best linear least-squares fit, we deduced an O_2 quenching rate constant of 3.2 × 10^9 s^{-1}, which within experimental error is equal to $^1/_9$ of the diffusion-controlled rate (~3.0 × 10^9 M^{-1} s^{-1} calculated from the Stokes–Einstein equation[29] that was derived theoretically from the T–O_2 sensitization. Thus, under oxygen saturation (1.15 × 10^{-2} M in cyclohexane at 1 atm O_2, 298 K [28]), the decay of the triplet state should be dominated (>97%) by the $T_1'-^3O_2$ energy transfer, thereby fulfilling requirement (iii).

Figure 5 shows the emission spectrum of the O_2 $^1\Delta_g{\to}^3\Sigma_g^-$ (0, 0) transition at 1274 nm that is sensitized by DIHBQ, of which the lifetime was determined to be ~21 μs in methylcyclohexane. Within experimental error, the decay dynamics
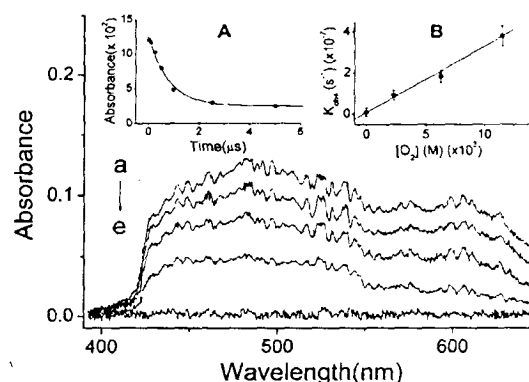

Figure 4. Transient absorption spectra of DIHBQ in degassed MCH (298 K) at pump–probe delay times of (a) 0 ns, (b) 250 ns, (c) 500 ns, (d) 1.0 μs, and (e) 10 μs. (A) Decay kinetics of the transient absorbance monitored at 475 nm. (B) Plot of the decay rate of transient absorbance at 475 nm vs oxygen concentration and the best linear least-squares fit.
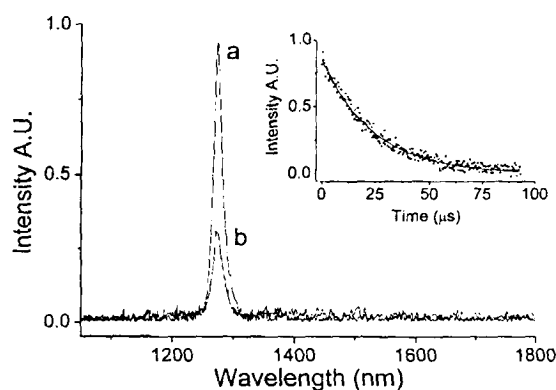

Figure 5. O_2 $^1\Delta_g{\to}^3\Sigma_g^-$ (0, 0) emission spectrum in MCH sensitized by (a) 1-H-phenalen-1-one and (b) DIHBQ under the same optical density of 0.2 at 362 nm (Ar$^+$ laser). Inset: Decay dynamics of the O_2 $^1\Delta_g{\to}^3\Sigma_g^-$ (0, 0) 1274 nm emission (λ_{ex}: 355 nm, Nd/YAG laser) sensitized by DIHBQ in MCH (298 K).

are identical to those of the O_2 ($^1\Delta_g$) emission in cyclohexane that was generated by a known sensitizer, 1-H-phenalen-1-one (PH).[30] We have further determined the triplet-state population in DIHBQ by comparing its sensitized O_2 ($^1\Delta_g$) emission intensity with respect to that produced with the sensitizer PH. The ratio of the sensitized O_2 ($^1\Delta_g$) emission intensity for DIHBQ versus PH was deduced to be 0.33 in O_2-saturated methylcyclohexane. Counting the PH-sensitized O_2 ($^1\Delta_g$) yield of 0.92 ± 0.1 [31] and ~98% of the triplet-state quenching dynamics for DIHBQ in O_2 saturated cyclohexane (vide supra), the yield of intersystem crossing Φ_{isc}^K was then estimated to be 0.31. In this derivation, we have assumed that the production of O_2 ($^1\Delta_g$) that is sensitized by the triplet state is of unit efficiency. This assumption is based on a spin statistical argument in which the only deactivation pathway of the triplet state resulting from the $T_1'-O_2$ ($^3\Sigma_g^-$) encounter is the energy transfer to form O_2 ($^1\Delta_g$). Because the assumption of unit efficiency of O_2 ($^1\Delta_g$) generation in each $T_1'-^3O_2$ encounter may be invalid for DIHBQ, we used the value of $\Phi_{isc}^K = 0.31$ as the lower limit. Φ_{isc}^K is equivalent to k_{isc}^K/k_f^K where k_{isc}^K and k_f^K are rate constants of intersystem crossing and fluorescence decay, respectively, for the keto form. Knowing k_f^K to be 4.55 × 10^9 s^{-1} ($\tau_f = 220$ ps^{-1}), k_{isc}^K was thus deduced to be 1.41 × 10^9 s^{-1} at 298 K. k_{isc}^K is further assumed to be independent of
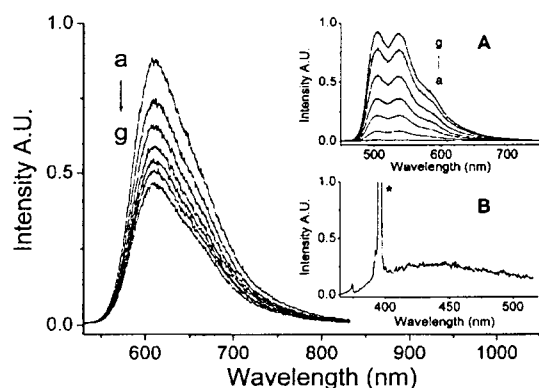
Figure 6. Disappearance of $S_1' \rightarrow S_0'$ fluorescence and growth of 505-nm phosphorescence spectra (A) of DIHBQ as a function of photolysis (355 nm, 35 mJ/cm², 10 Hz) periods of (a) 0, (b) 0.5, (c) 1.0, (d) 1.5, (e) 2.0, (f) 2.5, and (g) 3.0 min in a 77 K MCH glass. (B) Fluorescence spectrum of DIHBQ after 30 min of photolysis in a 77 K MCH glass where >90% of DIHBQ was converted to the non-hydrogen-bonded enol form (λ_{ex}: 355 nm (35 mJ/cm²), * denotes Raman scattering).

temperature if the triplet-state population proceeds only through the $S_1' \rightarrow T_1'$ intersystem crossing and if the $S_1'-T_1'$ energy gap is $\gg kT$. Support for the latter assumption is given by the >2700 cm⁻¹ gap measured from the difference in peak maxima between keto fluorescence (~16 400 cm⁻¹) and phosphorescence (~13 605 cm⁻¹). Knowing the observed decay rate of ~1.67 × 10⁹ s⁻¹ ($\tau_f \approx 600$ ps) for the keto fluorescence, Φ_{isc}^K and Φ_p^K were thus calculated to be 0.85 and 1.53 × 10⁻⁵, respectively, for DIHBQ in a 77 K MCH glass. According to the relationship of $\Phi_p^K = k_r^P/k_{obs}^P$, where k_{obs}^P was measured to be 5.71 × 10⁵ s⁻¹, the radiative decay rate of keto phosphorescence, k_r^P, was further deduced to 8.8 s⁻¹.

3.2. Photolysis of DIHBQ and HBQ. Upon increasing the excitation laser intensity (355 nm) of >30 mJ/cm², significant photolysis time-dependent spectral evolutions for DIHBQ were observed in which both fluorescence ($\lambda_{max} \approx 610$ nm) and phosphorescence ($\lambda_{max} \approx 735$ nm) of the keto tautomer gradually decreased, accompanied by the appearance of an emission band that was maximized at 505 nm (Figure 6). By scanning the delay time of the gating ICCD, the lifetime of the 505-nm emission was measured to be 1.52 ms. It should be noted that after each photolysis period emission spectra and their associated lifetime of products were obtained under sufficiently low excitation intensity (<1.0 mJ/cm²) to avoid further photolysis reactions. The long life span unambiguously allows us to assign the 505-nm emission band to the phosphorescence. When the sample was thawed to the liquid phase and then was quickly frozen back to the glassy form at 77 K, both the fluorescence and phosphorescence of the keto form were completely recovered, accompanied by the disappearance of the 505-nm phosphorescence. In a comparative study, DIMBQ in a 77 K MCH glass exhibited phosphorescence with spectral features and relaxation dynamics ($\lambda_{max} \approx 495$ nm, $\tau_p \approx 1.2$ ms and $\Phi_p \sim 0.3$) that were similar to those of the photolysis product in DIHBQ. The results, in combination with the reversibility of the photolysis reaction during a thawing-and-freezing cycle, led us to conclude that upon the photolysis of DIHBQ the rupture of an intramolecular hydrogen bond takes place, forming a non-hydrogen-bonded enol conformer (vide infra).

A similar photolysis reaction was observed for HBQ in the glass matrixes where the decrease of the 607-nm keto fluorescence was obvious (Figure 7). However, instead of a dominant 505-nm enol phosphorescence observed upon photolyzing
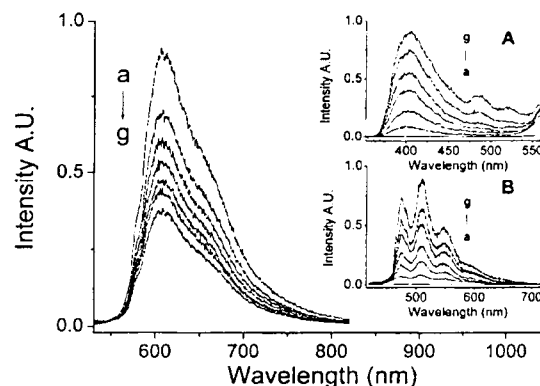

Figure 7. Disappearance of the $S_1' \rightarrow S_0'$ fluorescence and the growth of product emission (A) for HBQ in a 77 K MCH glass under the same photolysis condition as those used in Figure 6. (B) Growth of product phosphorescence as a function of photolysis period. To acquire B, the high-voltage gate width of ICCD was opened as wide as 10 ns with a delay time of 100 ns to eliminate fluorescence interference.

DIHBQ, the photolysis time-dependent spectral growth consists of dual emission maxima at 403 and 475 nm (see inset A of Figure 7). Note for inset A of Figure 7 that the ICCD was operated in a free-run mode so that the spectra were obtained via a steady-state manner. When the gate was opened at, for example, 10 ms followed by scanning the delay time of acquisition, long-lived 475-nm phosphorescence was resolved, the lifetime of which was determined to be ~1.2 s (see inset B of Figure 7). Conversely, the lifetime of the 403-nm emission band was measured to be ~3.0 ns so that its assignment to a fluorescence band is unambiguous. We have made a further attempt to estimate the yield of the photolysis reaction. In a 77 K transparent MCH glassy matrix, DIHBQ (optical density ~0.5 at 355 nm) was irradiated by a 355-nm laser beam (10 Hz), the intensity and beam diameter of which were measured to be 2.5 mJ and 3.0 mm (~35 mJ/cm²), respectively. After a photolysis period of 30 s, the intensity of the keto-tautomer fluorescence was reduced by 16.4%. By neglecting the inner filter effect, the photolysis efficiency Φ_{rxn} can thus be deduced from $(F_0 - F)\% = (E\%)[1 - (1 - \Phi_{rxn})^n]$ where $(F_0 - F)\%$ is the percentage decrease of the keto-tautomer emission intensity and $(E\%)$ and n denote the percentage of DIHBQ being excited (~45%) and the number of laser shots during the photolysis period (300), respectively. Φ_{rxn} was thus calculated to be 0.13% for DIHBQ. A similar procedure gave Φ_{rxn} to be ~0.15% for HBQ.

Under the weak excitation intensity that was used to obtain the enol-like phosphorescence that is shown in inset A of Figure 6, the fluorescence associated with the non-hydrogen-bonded enol product of DIHBQ was negligibly small. The result can be rationalized by the dominant rate of intersystem crossing that is enhanced by the iodine heavy-atom effect in the enol form. This viewpoint can be further supported by the ultraweak enol fluorescence ($\Phi_f \approx 10^{-4}$, $\tau_f \approx 120$ ps, see Table 1) measured in DIMBQ, whereas the corresponding phosphorescence is apparently strong ($\Phi_p \approx 0.3$). After a long period of photolysis, when >90% of the hydrogen-bonded enol species disappeared while monitoring the keto-tautomer fluorescence, very weak fluorescence at a peak maximum of 425 nm was indeed resolved for DIHBQ (inset B of Figure 6) under a high laser-excitation intensity (i.e., ~35 mJ/cm²). The lifetime was measured to be as short as ~50 ps (see Table 1). Similar heavy-atom-enhanced decay dynamics of phosphorescence ($\tau_p \approx 1.5$ × 10⁻³ s) were observed in the photolysis product (i.e., the

TABLE 1: Photophysical Properties of HBQ and DIHBQ and Their Corresponding Methylated Derivatives in 298 K and 77 K Methylcyclohexane

	absorption	fluorescence			phosphorescence		
	λ_{max}(nm)[a]	λ_{max}(nm)	Φ_{obs}	τ_f (ns)	λ_{max}(nm)	Φ_{obs}[b]	τ_p (s)[b]
HBQ	380	403[c]		3.00[b]	475[c]		1.20
		625[a]	2.1×10^{-3a}	0.30[a]			
		607[b]	6.3×10^{-3b}	0.54[b]			
MBQ	360	368[a]	0.05[a]	0.90[a]	466[b]		
		367[b]		3.33[b]			
DIHBQ	395	425[c]		0.05[b]	505[c]		1.52×10^{-3}
		640[a]	1.8×10^{-3a}	0.22[a]	735[b]	1.3×10^{-5}	1.75×10^{-6}
		610[b]	6.8×10^{-3b}	0.60[b]			
DIMBQ	375	400[a]	1.0×10^{-4a}	0.12[a]	495[b]	0.3	1.20×10^{-3}

[a] 298 K. [b] 77 K. [c] Photolysis products at 77 K.

non-hydrogen-bonded enol form) of DIHBQ. In comparison, the phosphorescence lifetime of the non-hydrogen-bonded enol form was measured to be as long as 1.2 s in HBQ.

The photoinduced rupture of the intramolecular hydrogen bond may not be uncommon among ESIPT molecules. A similar mechanism has been proposed to explain the photolysis of salicylaldehyde (SA) in low-temperature solid matrixes.[32] Nagaoka et al.[33] have reported that except for the major channels of radiationless deactivation (i.e., proton-transfer reaction, intersystem crossing, and internal conversion) SA undergoes a minor photoisomerization channel, thus forming an open enol-conformer. On the basis of FTIR analyses of vibrational modes for various deuterium isotope substitutions, Morgan et al.[34] further resolved the open conformer to be a structure in which both the hydroxyl and aldehyde functional groups rotate by 180°.

When a CW Ar$^+$ laser (362.5 nm) was used as an excitation source, similar photolysis reactions were observed for both HBQ and DIHBQ in a 77 K MCH glass. The results eliminate the photolysis mechanism that mainly results from the multiphoton event. In another approach, if the rupture of the intramolecular hydrogen bond occurred in the enol excited state, one would expect a similar reaction pattern in the keto $^1\pi\pi^*$ state for which the lifetime ($\sim$600 ps) is much longer even than that ($\ll$15 ps) of the enol form. However, detailed excitation spectral analyses showed no existence of photolysis products with the absorption chromophore of >420 nm, indicating that photoisomerization did not take place in the keto form. Accordingly, the possibility that for HBQ and DIHBQ the electronically excited enol form undergoes an O−H rotation in competition with the ultrafast ESIPT dynamics is discounted as well.

As shown in Scheme 1 (vide infra), both ESIPT and ground-state reverse proton-transfer reactions are highly exergonic. These results, in combination with the dominant $S_1'{\rightarrow}S_0'$ radiationless transition (see Table 1), led us to propose a more plausible mechanism that incorporates the formation of a vibrationally hot, hydrogen-bonded enol after a proton-transfer cycle. Subsequently, the highly exothermic energy dissipated from the radiationless transition generates the local heat, which thermally activates the −OH rotation in the glassy matrixes. The plausible product (i.e., a non-hydrogen-bonded enol form with the hydroxyl proton rotating out of the hydrogen-bonding configuration) is dynamically stable and is trapped in the glass matrix by the constraint of the solid environment. Upon fusion of the solvent, the product relaxes back to the thermodynamically more stable enol form possessing an intact hydrogen-bonding configuration. Unlike SA, where both the O−H and carbonyl functional groups can rotate simultaneously,[34] pyridinic nitrogen in HBQ and DIHBQ is fixed in a planar geometry. Thus, the photolysis product (i.e., the enol conformer) seems to be incorporated only with the rotation of hydroxyl proton,

though the actual degree of rotation is not accessible at this stage.

3.3. Energy Diagram. With the above experimental results, we herein attempt to construct an energy diagram regarding an overall proton-transfer cycle in DIHBQ. As shown in Scheme 1, the energy of the S_0 state of the enol tautomer has been arbitrarily set to 0 kcal/mol. In addition, because of more informative data and less thermal perturbation, the construction of relative energy levels is done under the environment of a 77 K MCH glass. Scheme 1 also shows population and quantum yields of various photophysical pathways. The relative energy levels for S_1' and T_1' were taken directly from the peak maxima of keto fluorescence (610 nm) and phosphorescence (735 nm), respectively. Fluorescence (425 nm) and phosphorescence (505 nm) of the non-hydrogen-bonded enol form were applied for the S_1 and T_1 states. One must be cautious here to make sure that the hydrogen-bonded enol form normally exhibits a bathochromic spectral shift in the singlet manifold with respect to the non-hydrogen-bonded conformer. The relative energy gap between the enol (S_0) and keto (S_0') forms in the ground state is experimentally unobtainable because of the ultrafast ground-state reverse proton transfer and thus has to be accessed through theoretical approaches. However, the large spin−orbit coupling factor limits ab initio calculations at higher-level basis sets. Alternatively, semiempirical approaches based on AM1 and PM3 methods were performed, resulting in S_0' being higher in energy than S_0 by 8.7 and 11.8 kcal/mol, respectively. By taking an average of 10.3 kcal/mol for the $S_0 - S_0'$ energy gap, we depict the relative energy levels for the overall proton-transfer cycle in DIHBQ in Scheme 1. The T_1 state of the enol form is estimated to be $\sim$7.42 kcal/mol higher in energy than the T_1' state of the keto tautomer, indicating that the $T_1'{\rightarrow}T_1$ reverse proton transfer is highly endergonic, which is consistent with the experimental results.

4. Conclusions

On the basis of the heavy-atom effect, the lowest-lying triplet state of the proton-transfer keto tautomer has been studied by its corresponding ultraweak phosphorescence at 735 nm. The results, in combination with the photolysis experiment and theoretical approaches, lead to the establishment of relative energy levels during a proton-transfer cycle in different spin manifolds. The relaxation dynamics of T_1' were dominated by radiationless deactivation. The result is qualitatively consistent with the energy gap law, leading to the conclusion that the intramolecular radiationless deactivation constant should increase with the decreasing energy gap of the transition.[25] The application of the iodine heavy-atom effect enhances both $S_1'{\rightarrow}T_1'$ intersystem crossing and $T_1'{\rightarrow}S_0'$ radiative decay rates,

which, coupled with an ultrasensitive NIR detecting system, turns out to be crucial to the resolution of the spectroscopy and dynamics of the triplet states of ESIPT molecules.

Despite the strong intramolecular hydrogen bond formation in both HBQ and DHHBQ, O–H rotational enol conformers were produced during the photolysis. The similarity in the photolysis patterns between HBQ and SA derivatives leads us to propose the possibility of generalizing a mechanism incorporating photoinduced hydrogen bond breakage among ESIPT molecules in glassy matrixes, particularly for those possessing weak hydrogen bonds such as 3-hyroxyflavone.[18a] Our preliminary results have shown that in addition to the protic-solvent perturbation photoinduced breakage of the intramolecular hydrogen bond in 3-hydroxyflavones played a role in the prohibition of ESIPT reaction in 77 K MCH glassy matrixes.[35] Accordingly, one may have to exercise great caution when considering the application of ESIPT molecules to solid-state devices in which the operation is, in principle, based on the ESIPT mechanism.

References and Notes

(1) For reviews on related subjects, see refs 2–11

(2) Kasha, M. *J. Chem. Soc., Faraday Trans. 2* **1986**, *82*, 2379.

(3) Kosower, E. M.; Huppert, D. *Annu. Rev. Phys. Chem.* **1986**, *37*, 127.

(4) Barbara, P. F.; Walsh, P. K.; Brus, L. E. *J. Phys. Chem.* **1989**, *93*, 29.

(5) Nagaoka, S.; Nagashima, U. *Chem. Phys.* **1989**, *136*, 153.

(6) Chou, P. T.; Martinez, M. L.; Studer, S. L. *J. Phys. Chem.* **1991**, *95*, 10306.

(7) Formosinho, S. F.; Arnaut, L. G. *J. Photochem. Photobiol., A* **1993**, *75*, 21.

(8) Douhal, A.; Lahmani, F.; Zewail, A. H. *Chem. Phys.* **1996**, *207*, 477.

(9) Pfeiffer, M.; Lau, A.; Lenz, K.; Elsaesser, T. *Chem. Phys. Lett.* **1997**, *268*, 258

(10) Moriyama, M.; Kosuge, M.; Tobita, S.; Shizuka, H. *Chem. Phys.* **2000**, *253*, 91.

(11) Scheiner, S. *J. Phys. Chem. A* **2000**, *104*, 5898.

(12) For example, see (a) Chou, P. T.; McMorrow, D.; Aartsma, T. J.; Kasha, M. *J. Phys. Chem.* **1984**, *88*, 4596. (b) Ernsting, N. P.; Nikolaus, B.

Appl. Phys. B **1986**, *39*, 155. (c) Acuña, A. V.; Amat-Guerri, F.; Catalán, J.; Costella, A.; Figuera, J.; Munoz, J. *Chem. Phys. Lett.* **1986**, *132*, 576. (d) Kasha, M. In *Molecular Electronic Devices*; Carter, F. L., Siatkowski, R. E., Wohltjen, H., Eds.; Elsevier Science Publishers: New York, 1988; pp 107–121. (e) Catalán, J.; del Valle, J. C. *J. Am. Chem. Soc.* **1993**, *115*, 4321. (f) Ferrer, M. L.; Acuña, A. U.; Amat-Guerri, F.; Costela, A.; Figuera, J. M.; Florido, F.; Sastre, R. *Appl. Opt.* **1994**, *33*, 2266. (g) Jones, G.; Rahman, M. A. *J. Phys. Chem.* **1994**, *98*, 13028. (h) Liphardt, M.; Gooneskera, A.; Jones, B. E.; Ducharme, S.; Takacs, J. M.; Zhang, L. *Science (Washington, D.C.)* **1994**, *263*, 367. (i) Kuldová, K.; Corval, A.; Trommsdorff, H. P.; Lehn, J. M. *J. Phys. Chem. A* **1997**, *101*, 6850.

(13) Sytnik, A.; Gormin, D.; Kasha, M. *Proc. Natl. Acad. Sci. U.S.A.* **1994**, *91*, 8267, 11968.

(14) Sytnik, A.; del Valle, J. C. *J. Phys. Chem.* **1995**, *99*, 13028.

(15) Roshal, A. D.; Grigorovich, A. V.; Doroshenko, A. O.; Pivovarenko, V. G.; Demchenko, A. P. *J. Phys. Chem. A* **1998**, *102*, 5907.

(16) Tarkka, R. M.; Zhang, X.; Jenekhe, S. A. *J. Am. Chem. Soc.* **1996**, *118*, 9438.

(17) Martinez, M. L.; Cooper, W. C.; Chou, P. T. *Chem. Phys. Lett.* **1992**, *193*, 151.

(18) For example, see (a) Kasha, M.; McMorrow, D. *J. Phys. Chem.* **1984**, *88*, 2235. (b) Grellman, K. H.; Mordzinski, A.; Heinrich, A. *Chem. Phys.* **1989**, *136*, 201. (c) Schwartz, B. J.; Peteanu, L. A.; Harris, C. B. *J. Phys. Chem.* **1992**, *96*, 3591. (d) Tobita, S.; Yamamoto, M.; Kurahayashi, N.; Tsukagoshi, R.; Nakamura, Y.; Shizuka, H. *J. Phys. Chem. A* **1998**, *102*, 5206.

(19) Chou, P. T.; Wei, C. Y. *J. Phys. Chem.* **1996**, *100*, 17059.

(20) Chou, P. T.; Martinez, M. L. *Radiat. Phys. Chem.* **1993**, *41*, 373.

(21) Roberts, E. L.; Chou, P. T.; Alexander, T. A.; Agbaria, R. A.; Warner, I. M. *J. Phys. Chem.* **1995**, *99*, 5431.

(22) del Valle, J. C.; Catalán, J. *Chem. Phys.* **2001**, *270*, 1.

(23) Chou, P. T.; Chen, Y. C.; Yu, W. S.; Chou, Y. H.; Wei, C. Y.; Cheng, Y. M. *J. Phys. Chem. A* **2001**, *105*, 1731.

(24) McGlynn, S. P.; Azumi, T.; Kinoshita, M. *Molecular Spectroscopy of the Triplet State*; Prentice Hall: Englewood Cliffs, NJ, 1969; p 18.

(25) Sieband, W. *J. Chem. Phys.* **1967**, *47*, 2411.

(26) Klöpffer, W. *Adv. Photochem.* **1977**, *10*, 311.

(27) For recent studies of heavy atom effects on the ESIPT reaction, see Catalán, J.; Diaz, C. *J. Phys. Chem. A* **1998**, *102*, 323.

(28) Battino, R.; Rettich, T. R.; Tominaga, T. *J. Phys. Chem. Ref. Data.* **1983**, *12*, 163.

(29) Birks, J. B. *Photophysics of Aromatic Molecules*; Wiley: New York, 1970; p 313.

(30) (a) Schmidt, R.; Bodesheim, M. *Chem. Phys. Lett.* **1993**, *213*, 111. (b) Schmidt, R.; Bodesheim, M. *J. Phys. Chem.* **1994**, *98*, 2874. (c) Schmidt, R.; Bodesheim, M. *J. Phys. Chem.* **1995**, *99*, 15919.

(31) Schmidt, R.; Tanielian, C.; Dunsbach, R.; Wolff, C. *J. Photochem. Photobiol., A* **1994**, *79*, 11.

(32) Lamola, A. A.; Sharp, L. J. *J. Phys. Chem.* **1966**, *70*, 2634.

(33) Nagaoka, S.; Hirota, N.; Sumitani, M.; Yoshihara, K. *J. Am. Chem. Soc.* **1983**, *105*, 4220.

(34) Morgan, M. A.; Orton, E.; Pimental, G. C. *J. Phys. Chem.* **1990**, *94*, 7927.

(35) Chou, P. T.; Wei, C. Y. Unpublished work.

Self-Complementarity of Oligo-2-aminopyridines: A New Class of Hydrogen-Bonded Ladders

Man-kit Leung, Ashis B. Mandal, Chih-Chieh Wang,
Gene-Hsiang Lee, Shie-Ming Peng, Hsing-Ling Cheng,
Guor-Rong Her, Ito Chao, Hsiu-Feng Lu, Ying-Chieh Sun,
Mei-Ying Shiao, and Pi-Tai Chou

Contribution from the Department of Chemistry, National Taiwan
University, Taipei 106, Taiwan, Department of Chemistry, Soochow
University, Taipei, Taiwan, Institute of Chemistry, Academia Sinica,
Taipei, Taiwan, Department of Chemistry, National Taiwan Normal
University, Taipei, Taiwan, and Department of Chemistry, National
Chung Cheng University, Chia Yi, Taiwan

JOURNAL
OF THE
AMERICAN
CHEMICAL
SOCIETY®

Self-Complementarity of Oligo-2-aminopyridines: A New Class of Hydrogen-Bonded Ladders

Man-kit Leung,*,† Ashis B. Mandal,† Chih-Chieh Wang,‡ Gene-Hsiang Lee,†
Shie-Ming Peng,*,† Hsing-Ling Cheng,† Guor-Rong Her,† Ito Chao,*,§ Hsiu-Feng Lu,‖
Ying-Chieh Sun,‖ Mei-Ying Shiao,⊥ and Pi-Tai Chou*,†

*Contribution from the Department of Chemistry, National Taiwan University,
Taipei 106, Taiwan, Department of Chemistry, Soochow University, Taipei, Taiwan,
Institute of Chemistry, Academia Sinica, Taipei, Taiwan, Department of Chemistry,
National Taiwan Normal University, Taipei, Taiwan, and Department of Chemistry,
National Chung Cheng University, Chia Yi, Taiwan*

Received July 10, 2001. Revised Manuscript Received November 15, 2001

Abstract: A new class of hydrogen-bonded ladders based on hydrogen-bonded dimerization of oligo-α-aminopryidines has been demonstrated. Jorgensen's model can be successfully applied to this hydrogen-bonding system in nonpolar solvents. The results show the competitive enthalpy/entropy compensation relationship upon dimerization. Although increasing the number of hydrogen-bonding interactions would enhance the hydrogen-bonding stabilization enthalpy, this stabilization enthalpy per unit would be partially sacrificed to compensate for the entropy loss due to dimerization. These results clearly support the importance of preorganization in designing hydrogen-bonding guest–host molecules.

1. Introduction

The construction of molecules that associate in a strong, directional, and selective mode is a challenging topic in supramolecular chemistry. Because hydrogen bonds are relatively flexible in geometry as compared to rigid covalent bonds, the principle of using hydrogen bonds to confer binding strength and selectivity has become an important topic for research.[1,2] Many examples of using hydrogen-bonding interactions to control the self-assembling of molecules into well-defined aggregates, ranging from container molecules,[3] supramolecular tubes,[4] to

artificial ion channels,[5] have been reported during the past decade. In addition, the principle of hydrogen-bonding interactions has also been applied to crystal engineering.[6] This requires self-recognition between identical molecules, a much less common phenomenon usually restricted to molecules containing "complementary donor and acceptor units". Recently, using the hydrogen-bond array, instead of covalent bonds, to construct zipperic ladder molecules has been explored.[7,8] Polymeric structure **1** intrigues us because **1** may dimerize to form a belt-shape zipperic dimer through hydrogen-bonding interactions. Because **1** contains an alternating proton donor/acceptor sequence, according to Jorgensen's theory,[9] a relatively strong secondary repulsive interaction is expected. This would lead to a relatively small hydrogen-bonding stabilization arising from each of the repeating units. The prediction is particularly attractive to us

* To whom correspondence should be addressed. E-mail: P.-T.C., chop@ccms.ntu.edu.tw; M.-k.L., mkleung@ms.cc.ntu.edu.tw; S.-M.P., smpeng@mail.ch.ntu.edu.tw.
  † National Taiwan University.
 ‡ Soochow University.
  § Academia Sinica.
 ‖ National Taiwan Normal University.
  ⊥ National Chung Cheng University.
(1) For recent reviews, see: (a) Prins, L. J.; Reinhoudt, D. N.; Timmerman, P. *Angew. Chem., Int. Ed.* **2001**, *40*, 2382. (b) Zimmerman, S. C.; Corbin, P. S. *Struct. Bonding* **2000**, *96*, 63. (c) Niemz, A.; Rotello, V. M. *Acc. Chem. Res.* **1999**, *32*, 44. (d) Ward, M. D. *Chem. Soc. Rev.* **1997**, *26*, 365. (e) Doronina, S. O.; Behr, J. P. *Chem. Soc. Rev.* **1997**, *26*, 63. (f) Fyfe, M. C. T.; Stoddart, J. F. *Acc. Chem. Res.* **1997**, *30*, 393.
(2) For examples, see: (a) Corbin, P. S.; Zimmerman, S. C. *J. Am. Chem. Soc.* **2000**, *122*, 3779. (b) Zeng, H.; Miller, R. S.; Flowers, R. A., II; Gong, B. *J. Am. Chem. Soc.* **2000**, *122*, 2635. (c) Appella, D. H.; Barchi, J. J., Jr.; Durell, S. R.; Gellman, S. H. *J. Am. Chem. Soc.* **1999**, *121*, 2309. (d) Ranganathan, A.; Pedireddi, V. R.; Rao, C. N. R. *J. Am. Chem. Soc.* **1999**, *121*, 1752. (e) Kuduva, S. S.; Craig, D. C.; Nangia, A.; Desiraju, G. R. *J. Am. Chem. Soc.* **1999**, *121*, 1936. (f) Marfurt, J.; Leumann C. *Angew. Chem., Int. Ed.* **1998**, *37*, 175. (g) Coe, S.; Kane, J. J.; Nguyen, T. L.; Toledo, L. M.; Wininger, E.; Fowler, F. W.; Lauher, J. W. *J. Am. Soc. Chem.* **1997**, *119*, 86.
(3) (a) Castellano, R. K.; Nuckolls, C.; Rebek, J., Jr. *J. Am. Chem. Soc.* **1999**, *121*, 11156. (b) Schalley, C. A.; Martín, T.; Obst, U.; Rebek, J., Jr. *J. Am. Chem. Soc.* **1999**, *121*, 2133. (c) Vysotsky, M. O.; Pop, A.; Broda, F.; Thondorf, I.; Bohmer, V. *Chem.-Eur. J.* **2001**, *7*, 4403.
(4) Baumeister, B.; Matile, S. *Chem.-Eur. J.* **2000**, *6*, 1739.

(5) (a) Sakai, N.; Brennan, K. C.; Weiss, L. A.; Matile, S. *J. Am. Chem. Soc.* **1997**, *119*, 8726. (b) Sakai, N.; Matile, S. *Chem.-Eur. J.* **2000**, *6*, 1731.
(6) MacDonald, J. C.; Whitesides, G. M. *Chem. Rev.* **1994**, *94*, 2383.
(7) For recent reviews, see: (a) Piguet, C.; Bernardinelli, G.; Hopfgartner, G. *Chem. Rev.* **1997**, *97*, 2005. (b) Rebek, J., Jr. *Chem. Soc. Rev.* **1996**, 255. (c) Whitesides, G. M.; Simanek, E. E.; Mathias, J. P.; Seto, C. T.; Chin, D. N.; Mammen, M.; Gordon, D. M. *Acc. Chem. Res.* **1995**, *28*, 37.
(8) For recent examples, see: (a) Corbin, P. S.; Zimmerman, S. C.; Thiessen, P. A.; Hawryluk, N. A.; Murray, T. J. *J. Am. Chem. Soc.* **2001**, *123*, 10475. (b) Archer, E. A.; Sochia, A. E.; Krische, M. J. *Chem.-Eur. J.* **2001**, *7*, 2049. (c) Söntjens, S. H. M.; Sijbesma, R. P.; van Genderen, M. H. P.; Meijer, E. W. *J. Am. Chem. Soc.* **2000**, *122*, 7487. (d) Archer, E. A.; Goldberg, N. T.; Lynch, V.; Krische, M. J. *J. Am. Chem. Soc.* **2000**, *122*, 5006. (e) Bisson, A. P.; Carver, F. J.; Eggleston, D. S.; Haltiwanger, R. C.; Hunter, C. A.; Livingstone, D. L.; McCabe, J. F.; Rotger, C.; Rowan, A. E. *J. Am. Chem. Soc.* **2000**, *122*, 8856. (f) Folmer, B. J. B.; Sijbesma, R. P.; Kooijman, H.; Spek, A. L.; Meijer, E. W. *J. Am. Chem. Soc.* **1999**, *121*, 9001. (g) Sakai, N.; Majumdar, N.; Matile, S. *J. Am. Chem. Soc.* **1999**, *121*, 4294. (h) Sessler, J. L.; Wang, R. *Angew. Chem., Int. Ed.* **1998**, *37*, 1726. (i) Bisson, A. P.; Carver, F. J.; Hunter, C. A.; Waltho, J. P. *J. Am. Chem. Soc.* **1994**, *116*, 10292. (j) Ghadiri, M. R.; Granja, J. R.; Milligan, R. A.; McRee, D. E.; Khazanovich, N. *Nature* **1993**, *366*, 324.

Scheme 1
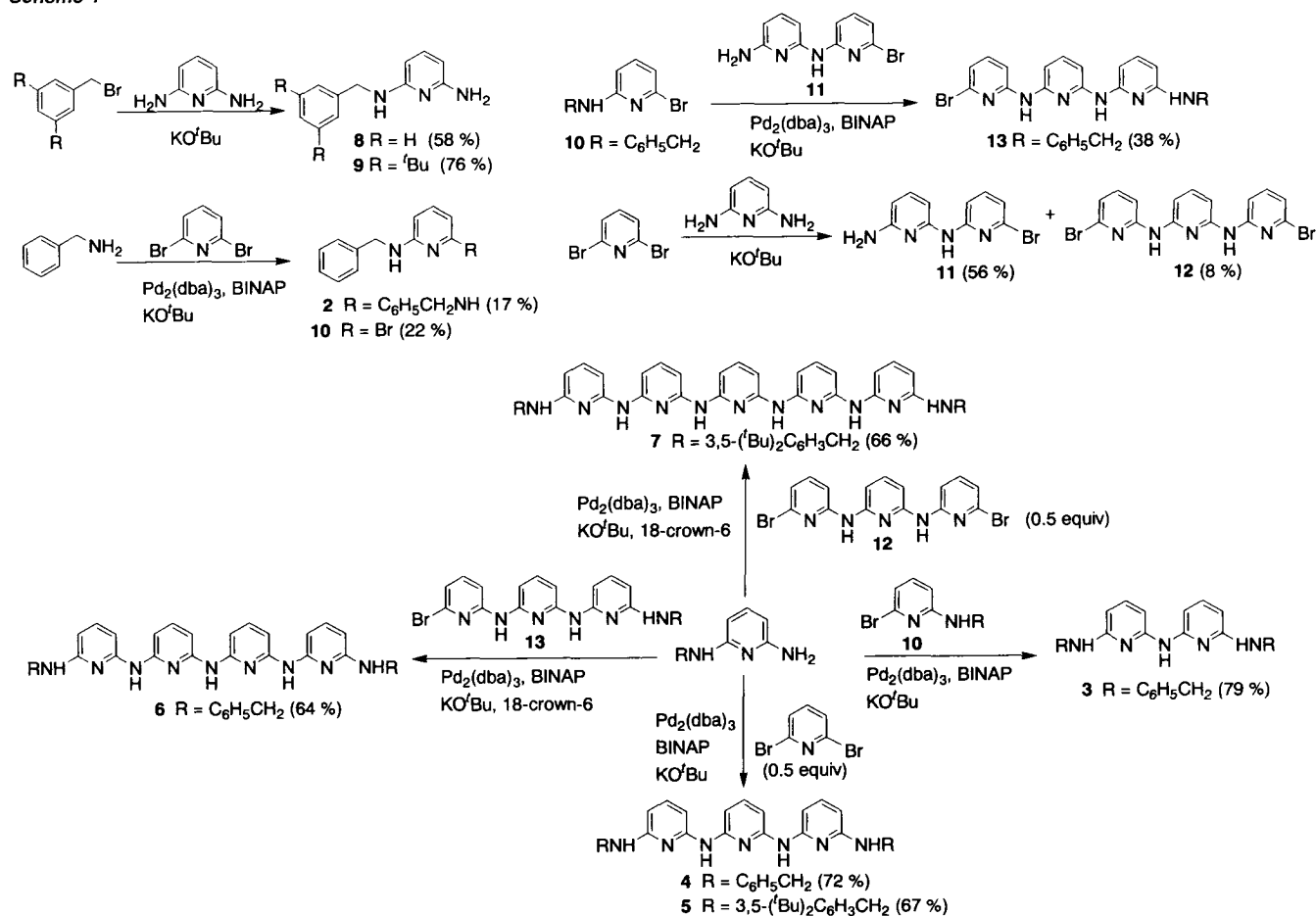
because a relatively low dissociation energy barrier for the zipperic dimer would be expected. This implies a fast association—dissociation process that may be beneficial for **1** to search for the optimal matching, resulting in the most stable dimeric pair.
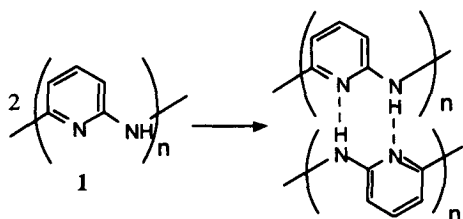
To evaluate the dimerization behavior of **1**, the dimerization behavior of its oligomers **2**−**7** is investigated. Through a systematic study of the structure of their zipperic hydrogen-bonded dimers in solid state as well as their thermodynamics upon hydrogen-bonded dimerization in the solution phase, valuable information can be provided about the self-dimerization process. In addition, this study provides a systematic way to evaluate the Jorgensen's theory, an important model for the quantitative prediction of hydrogen-bonding interactions.

2 R = H, n = 1   3 R = H, n = 2
4 R = H, n = 3   5 R = t-Bu, n = 3
6 R = H, n = 4   7 R = t-Bu, n = 5
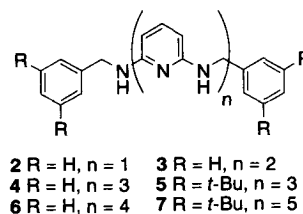
2. Results and Discussion

2.1. Tactic for the Synthesis of 2−7. Syntheses of **2** and **8** have been reported in the literature.[10] Oligomers **3**−**7**, and their precursors, were prepared on the basis of the Buchwald's palladium-catalyzed amination procedures (Scheme 1).[11] To construct the target molecules, terminal building blocks **8** and the di-*tert*-butyl substituted **9** were prepared from benzylation of 2,6-diaminopyridine. Terminal di-*tert*-butyl substituted **9** was used as the precursor for **5** and **7** because it could enhance the solubility[12] of **5** and **7**. The solubility criterion is particularly important in the measurements of the dimerization constant. Compound **10** was obtained from palladium-catalyzed monoam-

(9) (a) Zimmerman, S. C.; Murray, T. J. *Tetrahedron Lett.* **1994**, *35*, 4077; **1995**, *36*, 7627. (b) Murray, T. J.; Zimmerman, S. C. *J. Am. Chem. Soc.* **1992**, *114*, 4010. (c) Pranata, J.; Wierschke, S. G.; Jorgensen, W. L. *J. Am. Chem. Soc.* **1991**, *113*, 2810. (d) Jorgensen, W. L.; Pranata, J. *J. Am. Chem. Soc.* **1990**, *112*, 2008.

(10) (a) Sprinzak, Y. *J. Am. Chem. Soc.* **1956**, *78*, 3207. (b) Czuba, W.; Kowalski, P. *Pol. J. Chem.* **1980**, *54*, 853.

(11) (a) Wagaw, S.; Buchwald, S. L. *J. Org. Chem.* **1996**, *61*, 7240. (b) Lai, S.-Y.; Lin, T.-W.; Chen, Y.-H.; Wang, C.-C.; Lee, G.-H.; Yang, M.-h.; Leung, M.-k; Peng, S.-M. *J. Am. Chem. Soc.* **1999**, *121*, 250. (c) Yang, M.-H.; Lin, T.-W.; Chou, C.-C.; Lee, H.-C.; Chang, H. C.; Lee, G.-H.; Leung, M-.k.; Peng, S.-M. *Chem. Commun.* **1997**, 2279.

(12) Schenk, R.; Gregorius, H.; Meerholz, K.; Heinze, J.; Müllen, K. *J. Am. Chem. Soc.* **1991**, *113*, 2634.

Table 1. Crystallographic Data for **2a**, **2b**, **3**, and **4**

	2a	2b	3	4
chemical formula	$C_{19}H_{19}N_3$	$C_{19}H_{19}N_3$	$C_{24}H_{23}N_5$	$C_{29}H_{27}N_7$
formula weight	289.37	289.37	381.47	473.58
space group	$P2/c$	$P2_1$	$P2_1/c$	$C2/c$
a (Å)	17.0899(3)	12.9834(5)	14.5143(3)	18.7696(4)
b (Å)	9.0332(1)	5.6602(2)	19.6482(4)	12.1599(20
c (Å)	15.8559(1)	21.9238(7)	14.7183(3)	21.8358(5)
β (°)	102.860(1)	100.692(1)	99.308(2)	98.384(1)
V (Å³)	2386.38(5)	1583.2(1)	4142.1(2)	4930.5(2)
Z	6	4	8	8
$F(000)$	924	616	1616	2000
T (K)	295(2)	295(2)	295(2)	295(2)
λ (Mo Kα) (Å)	0.71073	0.71073	0.71073	0.71073
D_{calc} (kg m^{-3})	1.208	1.214	1.223	1.276
μ (mm^{-1})	0.073	0.073	0.075	0.079
reflection collected	17 892	6396	25 990	25 402
unique reflections	4217	4529	7296	4346
absorption correction	semiempirical from equivalents	semiempirical from equivalents	semiempirical from equivalents	semiempirical from equivalents
refinement on	F^2	F^2	F^2	F^2
parameters refined	312	414	548	342
$R(F_o)^a$ ($I > 2\sigma(I)$)	0.0763	0.0583	0.0611	0.0796
$R_w(F_o^2)^b$ ($I > 2\sigma(I)$)	0.1785	0.1067	0.1188	0.1410
$R(F_o)^a$ (all data)	0.1479	0.0912	0.1349	0.1338
$R_w(F_o^2)^b$ (all data)	0.2195	0.1236	0.1500	0.1858
GOF on F^2	1.002	1.106	1.055	1.222

$^a R(F_o) = \Sigma ||F_o| - |F_c||/\Sigma|F_o|$. $^b R_w(F_o^2) = [\Sigma\{w(F_o^2 - F_c^2)^2\}/\Sigma\{w(F_o^2)^2\}]^{1/2}$.

ination of 2,6-dibromopyridine. The internal building blocks **11** and **12** were obtained from a base-catalyzed coupling reaction of a 1:1 ratio of 2,6-dibromopyridine and 2,6-diaminopyridine. Although **12** is expected to be a minor product in our reaction conditions, it could be easily isolated by precipitation in CH_2Cl_2 due to the relatively low solubility of **12**. The residue was then concentrated and subjected to liquid chromatography on silica gel to give **11** as a pure product. Palladium-catalyzed Buchwald's coupling of **10** with **11** would afford another building block **13** in a 38% yield. On the other hand, **12** was used as an important block for the synthesis of **7**. Once the terminal and the internal building blocks were in hand, oligomers **3**–**7** were synthesized from the corresponding building blocks using normal Buchwald's coupling conditions. However, addition of 18-crown-6 was required in the synthesis of **6** and **7** to facilitate the coupling reaction.[13] Details of syntheses and spectral characterization are described in the following sections and in the Experimental Section.

2.2. Single-Crystal X-ray Crystallographic Analyses of 2–4. Single crystals of **2**–**4** were easily prepared by slow evaporation of the solvent, and their crystallographic data are summarized in Table 1. Unfortunately, attempts at preparation of the single crystals of **5**–**7** were unsuccessful. Intermolecular hydrogen-bonding interactions were observed in the crystal forms of compounds **2**–**4**, of which the hydrogen-bond parameters are summarized in Table 2.

Two crystallization patterns by the molecular aggregation of **2** are observed; one is a trimeric form **2a** (Figure 1), and the other is a zigzag polymeric chain **2b** (Figure 2). The **2a** form is $P2/c$ with $Z = 6$ in which an interesting trimer sharing four hydrogen bonds with a 2-fold axis through the N(5), C(22) atoms is found (Figure 1a). The nitrogen atom N(5) of the central pyridine is symmetrically hydrogen bonded to two amino groups N(3) and N(3A) of two other diaminopyridine molecules

Table 2. Geometrical Parameters for N–H···N Hydrogen Bonds Observed in the Crystal Lattices of **2a**, **2b**, **3**, and **4**

crystal	H-bond (Å)	D···A (Å)	H···A (Å)	∠D–H···A (°)
2a	N(3)–H(3)···N(5)	3.137(5)	2.21(3)	160(1)
	N(4)–H(4)···N(2)	3.008(5)	2.20(3)	158(1)
	mean	3.07	2.21	159
2b	N(1)–H(1)···N(2)	3.207(5)	2.54(4)	146(1)
	N(4)–H(4)···N(5)	3.170(5)	2.32(4)	147(1)
	mean	3.19	2.43	147
3	N(3)–H(3)···N(7)	3.022(5)	2.08(3)	178(1)
	N(5)–H(5)···N(9)	3.118(5)	2.16(4)	167(1)
	N(6)–H(6)···N(2)	3.071(5)	2.16(3)	169(1)
	N(8)–H(8)···N(4)	3.019(5)	2.09(3)	177(1)
	mean	3.06	2.12	173
4	N(1)–H(1)···N(6)	3.014(6)	2.15(4)	170(1)
	N(3)–H(3)···N(4)	3.025(6)	2.21(4)	166(1)
	N(5)–H(5)···N(2)	3.089(6)	2.15(4)	166(1)
	mean	3.04	2.17	167

(dashed line). On the other hand, the amino groups of the central molecule N(4) and N(4A) are bonded to the nitrogen atom of pyridine of the other two diaminopyridine molecules N(2) and N(2A) (dashed line). The N···N distances are found to be 3.173(5) and 3.008(5) Å for N(3)···N(5) and N(4)···N(2) hydrogen bonds, respectively. The hydrogen-bond H···N distances of 2.21(3) Å for N(3)–H(3)···N(5) and N(3A)–H(3A)···N(5) are slightly longer than those of 2.20(3) Å for N(4)–H(4)···N(2) and N(4A)–H(4A)···N(2A). Another 3-D picture of **2a** depicted in Figure 1b clearly displays the spatial arrangement among these trimers.

The second form **2b** is $P2_1$ with $Z = 4$ (Figure 2). Two crystallographic independent, one-dimensional zigzag hydrogen-bonding networks are found in this structure. Two chains are parallel to the b axis with different orientations. In one chain, one amino group N(1)–H(1) is hydrogen bonded to the pyridine N(2A) of the next layer. A similar bonding pattern also occurs in the other chain, in which N(4)–H(4) is hydrogen bonded to the pyridine N(5A) of the next layer. The presence of the hydrogen bonds aligns the benzene ring and

(13) Wolfe, J. P.; Buchwald, S. L. *J. Org. Chem.* **1997**, *62*, 6066.

(a)

(b)

Figure 1. (a) The molecular structure of **2** in a trimeric form. Ellipsoids are drawn at the 30% probability level. (b) Perspective view of **2a** along the crystallographic *b* axis.

pyridine ring of **2** packed in an orderly arrangement (Figure 2b), where the interlayer distance is equal to the length of the *b* axis (5.660 Å). The N(1)···N(2A) and N(4)···N(5A) distances are found to be 3.207(5) and 3.170(5) Å, respectively. The relatively long hydrogen-bond H···N distances of 2.54(4) and 2.32(4) Å for N(1)−H(1)···N(2A) and N(4)−H(4)···N(5A) with small bond angles of 146(1)° and 147(1)° in **2b** indicate weaker hydrogen-bonding interactions between molecules in comparison to those in **2a**.[14] We tentatively attributed this observation to the lower hydrogen-bonding density in **2b**, in which only one pair of hydrogen bond per molecule was formed. However, the existence of two forms of diaminopyridine in the solid state indicates that the two kinds of hydrogen-bonding network may only slightly differ in their free energy.

Compounds **3** and **4** crystallize in a spiral conformation of the dimeric form possessing four and six pairs of N−H···N hydrogen bonds, respectively, which are shown in Figures 3 and 4. Triaminodipyridine **3** crystallizes in *P*2₁/*c* with *Z* = 8. There is one helical dimer in an asymmetric unit (Figure 3). Four pairs of hydrogen bonds form between the amino groups and the nitrogen atoms of the pyridine groups. Similarly, tetraaminotripyridine **4** crystallizes in *C*2/*c* with *Z* = 8. The helical dimer is located at the crystallographic 2-fold axis in which only one molecule is found in an asymmetric unit (Figure 4). Six pairs of hydrogen bonds form in the dimeric configuration of **4**.

The distances between NH···N and N···N, as well as the NH···N angle, are useful parameters for evaluating the hydrogen-

bond interactions. In general, a strong hydrogen-bonding interaction would lead to short NH···N and N···N distances, and a large NH···N angle.[14] The N···N distances vary in a range of 3.019(5)−3.118(5) Å for **3** with an average of 3.06 Å, and 3.014(6)−3.089(6) Å with an average of 3.04 Å for **4**. The H···N distances vary in a range of 2.08(3)−2.16(4) Å for **3** with an average of 2.12 Å, and 2.15(4)−2.21(4) Å with an average of 2.17 Å for **4**. These values are slightly larger than the reported statistical mean distances of 2.939 Å (σ = 0.092) for N···N and 2.04 Å (σ = 0.14) for R_2NH···N (sp²), but still fall within the boundary of standard deviations.[15] The average NH···N angles of 173° and 167° for **3** and **4**, respectively, in comparison to the statistical mean of 166° (σ = 8.7) also suggest reasonably strong intermolecular hydrogen-bond interactions.

The distances between the donor nitrogen atoms and between the acceptor nitrogen atoms of the proximal hydrogen-bond donor−acceptor pairs are of particular importance because the secondary interactions arising from those atoms strongly affect the stability of the dimers. Data listed in Table 3 show an average N−N separation of 3.72 Å for the dimer of **3** and 3.69 Å for the dimer of **4**. Because these distances are still short, substantial electrostatic interactions are expected.[9c]

2.3. Thermodynamics of Dimerization. The possibility of the formation of hydrogen-bonded dimers in solution was first evaluated by electrospray ionization mass spectroscopy (ESI-MS).[16] Although mass spectrometry only reflects the properties of a gas-phase species, it has been known that the correlation between the gas phase and solution is often good for ESI-MS. In comparison to **4**, the relatively soluble *tert*-butyl substituted **5** is more appropriate for the latter ¹H NMR and UV−vis studies. Thus, among the list of compounds, we chose **2**, **3**, **5**, **6**, and **7** for the ESI-MS analysis. The signals of *m*/*z* = 2M + H in the ESI-MS analysis (Table 4) support the formation of dimers of **2**, **3**, **5**, **6**, and **7** in CHCl₃. However, the signal intensities in the ESI-MS measurement may be affected by many experimental factors, and the relative intensities do not simply reflect the relative amounts of the species in solution. Therefore, further ¹H NMR (in CDCl₃) and UV−vis spectroscopic experiments (in cyclohexane) were carried out to substantiate the MS results. These experiments should provide quantitative information about the hydrogen-bond directed zipperic self-dimerization.

¹H NMR Approaches. ¹H and ¹³C NMR spectra taken in CDCl₃ are in agreement with the structural assignments for compounds **2**−**7**. Figure 5 shows the plot of NH's chemical shifts versus concentrations for **2**, **3**, **5**, **6**, and **7** at 30 °C. Note that the NH peak was chosen to be well separated from the rest of the peaks to gain accuracy. Details for the choice of the specific NH's chemical shifts are provided in the Supporting Information. As shown in Figure 5, the concentration-dependence of the δ values for the amino protons of **2**, **3**, **5**, **6**, and **7** suggests hydrogen-bonded dimer formation.[17] The dimerization constants K_d, δ_i, and δ_f were obtained from nonlinear

(14) Jeffrey, G. A. *An Introduction to Hydrogen Bonding*; Oxford: New York, 1997; p 12.

(15) Llamas Saiz, A. L.; Foces-Foces, C. *J. Mol. Struct.* **1990**, *238*, 367.

(16) For example, see: Schalley, C. A.; Castellano, R. K.; Brody, M. S.; Rudkevich, D. M.; Siuzdak, G.; Rebek, J., Jr. *J. Am. Chem. Soc.* **1999**, *121*, 4568.

(17) Connors, K. A. *Binding Constants, The Measurement of Molecular Complex Stability*; Wiley: New York, 1987; p 202. To simplify the curve fitting process, δ_i of **2**, **3**, and **5**, and δ_f of **7** could be directly evaluated from the plot in Figure 5.
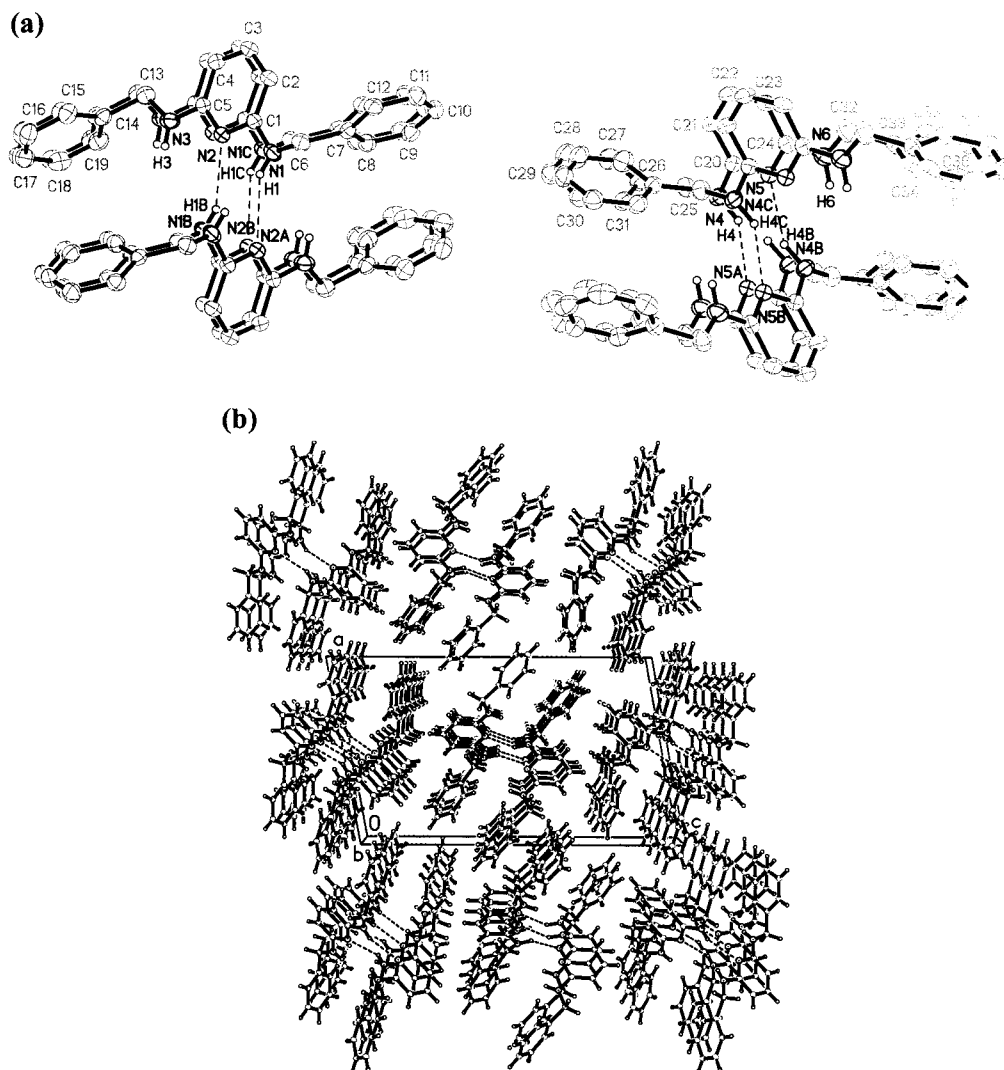
Figure 2. (a) The molecular structure of **2** in a polymeric zigzag form. Ellipsoids are drawn at the 30% probability level. (b) Perspective view of **2b** along the crystallographic *b* axis.
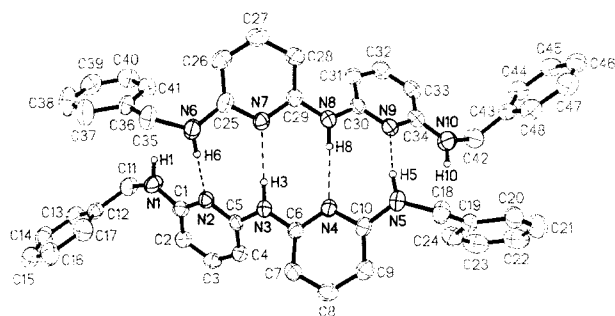

**Figure 3.** The dimeric structure of **3**. Ellipsoids are drawn at the 30% probability level.

Figure 4. The dimeric structure of **4**. Ellipsoids are drawn at the 30% probability level.

least-squares fitting of the data with eq 1 expressed as[17]

$$\delta = \delta_i + \frac{1 + 4K_d[\text{OAP}] - \sqrt{1 + 8K_d[\text{OAP}]}}{4K_d[\text{OAP}]}(\delta_f - \delta_i) \quad (1)$$

where [OAP] is the concentration of oligo-2-aminopyridines used in the measurement. δ_i and δ_f are the NH chemical shifts of oligo-2-aminopyridines in the monomeric and dimeric forms, respectively. The resulting dimerization constants along with

values for the dimerization free energy are listed in Table 5. The dimerization constant K_d of **2** is too low to be determined accurately. The low K_d value may qualitatively rationalize the unfavorable dimeric formation in the crystal packing. Instead, trimer **2a** and zigzag polymeric chain **2b** are dominant forms (vide supra). In $CDCl_3$, a fair estimation of the K_d value for **2** can be made. The magnitude of K_d (0.034 M^{-1}) for **2** in our estimation is reasonably close to the reported value of K_d (0.2 M^{-1}) for 2,6-$(C_5H_{11}(CO)NH)_2C_5H_3N$.[18] In addition, the correlation plot (Figure 6a) shows that the dimerization free energy

Table 3. Distances between the Donor Nitrogen Atoms and the Acceptor Nitrogen Atoms of the Proximal Hydrogen-Bond Donor–Acceptor Pairs (in Å)

	dimer of 3		dimer of 4
N1···N6	3.798	N1···N7	3.788
N2···N7	3.677	N1···N5	3.628
N3···N6	3.674	N2···N6	3.763
N3···N8	3.747	N2···N4	3.665
N4···N7	3.647	N3···N5	3.628
N4···N9	3.704	N3···N3	3.547
N5···N8	3.669	N4···N4	3.804
N5···N10	3.897		
mean	3.72	mean	3.69

Table 4. Electrospray Ionization Mass Spectral Data of **2**, **3**, **5**, **6**, and **7**

compound[a]	$m/z = M + H$ (base peak)	$m/z = 2M + H$ (rel intensity %)
2	290.2	577.3(4)
3	382.3	762.7(1)
5	689.6	1396.2(19)
6	566.4	1130.9(5)
7	882.9	1764.0(3)

[a] The concentrations of the samples were ranged from 1×10^{-3} to 3×10^{-3} M.
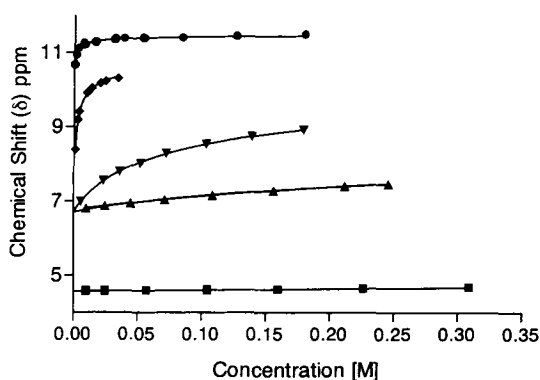
Figure 5. The plot of NH's chemical shifts versus concentrations for **2** (■), **3** (▲), **5** (▼), **6** (◆), and **7** (●) at 30 °C. (−) The best fitted curves for each plot using eq 1 (see text).

Table 5. Dimerization Constants and Thermodynamic Parameters (kJ mol⁻¹) for **2**, **3**, **5**, **6**, and **7** in CDCl₃ at 303 K

compound	n	$K_d\,[M^{-1}]$	ΔG^0_{dim}	ΔH^0_{dim} [c]	$T\Delta S^0_{dim}$ [c]
2	1	3.4×10^{-2} [a]	8.5 ± 2.0		
3	2	5.5×10^{-1} [b]	1.5 ± 0.1	-31 ± 3	$-33 \pm 3(32)$[d]
5	3	6.8[b]	-4.8 ± 0.2	-47 ± 2	$-42 \pm 2(41)$[d]
6	4	3.4×10^2 [b]	-14.7 ± 0.6	-75 ± 14	$-60 \pm 13(59)$[d]
7	5	1.0×10^4 [b]	-23.2 ± 0.4		

[a] Standard deviation is $\pm 2.3 \times 10^{-2}$ on the basis of nonlinear least-squares fitting. [b] Estimated relative error <20%. [c] The values were obtained from a linear plot of $1/T$ versus $R \ln(K_d)$, giving the slope equal to ΔH^0_{dim} and the intercept equal to ΔS^0_{dim}. [d] Values of $T\Delta S^0_{dim}$ at 298 K.

ΔG^0_{dim} is linearly correlated to the number of the repeating units with $r = 0.99$ in CDCl₃. On the basis of Jorgensen's analysis,[9c,d] a linear correlation equation of $\Delta G^0_{dim} = n(2P + 4S) = n(\Delta\Delta G^0_{dim})$ for our zipperic dimers is expected,[19] where n is the number of repeating units, $\Delta\Delta G^0_{dim}$ denotes the

(18) Beijer, F. H.; Sijbesma, R. P.; Vekemans, J. A. J. M.; Meijer, E. W.; Kooijman, H.; Spek, A. L. *J. Org. Chem.* **1996**, *61*, 6371.

(19) The equation was expressed in the convention proposed by Schneider. For references, see: (a) Lüning, U.; Kühl, C. *Tetrahedron Lett.* **1998**, *39*, 5735. (b) Sartorius, J.; Schneider, H.-J. *Chem.-Eur. J.* **1996**, *2*, 1446.
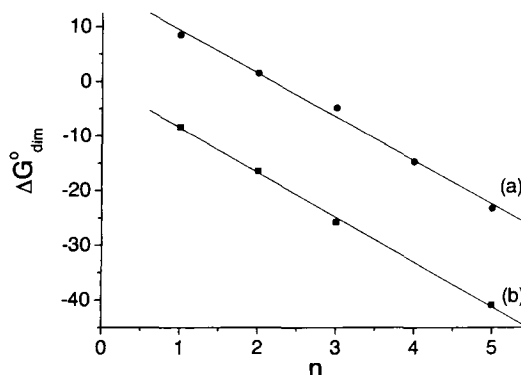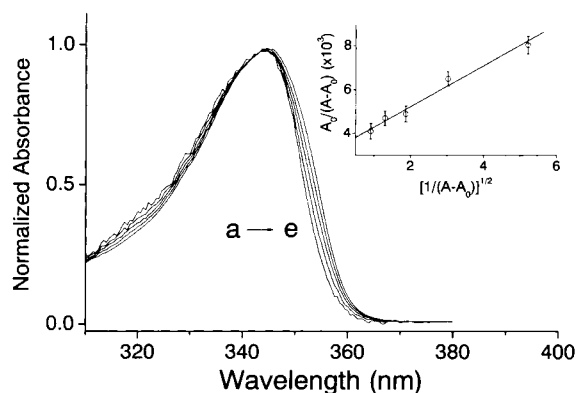
Figure 6. Plot of ΔG^0_{dim} (kJ mol⁻¹) versus n, the number of repeating 2-aminopyridine units: (a) in CDCl₃ (303 K), (b) in cyclohexane (298 K).

stabilization free energy arising from the hydrogen-bonding interactions per repeating unit, and P and S are the primary and secondary interactions defined by Jorgensen, respectively. However, our correlation plot in Figure 6a shows an empirical correlation of $\Delta G^0_{dim} = n(\Delta\Delta G^0_{dim}) + \Delta G^0_{int}$ which is slightly different from the predicted equation. Linear least-squares fitting of the data gives $\Delta\Delta G^0_{dim} = -8.0$ kJ/mol (the slope) and $\Delta G^0_{int} = 17.3$ kJ/mol (the intercept). Although as foreseen by Jorgensen's model where the dimerization free energy is linearly proportional to the number of the repeating units, the presence of a positive intercept, ΔG^0_{int},[20] in the correlation plot should not be ignored. Incorporating Schneider's empirical values of -7.9 and 2.9 kJ mol⁻¹ for the primary attractive and the secondary repulsive interactions,[19b] respectively, an increment of $\Delta\Delta G^0_{dim} = -4.2$ kJ/mol for each of the additional repeating units is anticipated from Jorgensen's equation. In comparison with this prediction, an increment of $\Delta\Delta G^0_{dim} = -8.0$ kJ/mol from our experiments is larger than the predicted one. These results indicate that the hydrogen-bonding interactions between our helical dimeric pairs are stronger than Schneider's statistical average. These results also suggest that mismatched pairing in the dimer formation is less favored. Mismatched pairing would lead to an increase of the ΔG^0_{dim}, leading to a less stable dimeric form. The presence of a positive intrinsic free energy, ΔG^0_{int}, indicates the existence of intrinsic factors that prevent the monomers from dimerization. These factors are independent of the hydrogen-bonding interactions in dimers, regardless of the units' number. Several possible factors including steric repulsion between terminal substituents, solvation effects, and entropy loss in dimerization may contribute to the nonnegligible ΔG^0_{int}.[21]

Temperature variation NMR experiments for **3**, **5**, and **6** were carried out to resolve ΔG^0_{dim} into ΔH^0_{dim} and $T\Delta S^0_{dim}$ (see Table 5). Linear least-squares fitting of the data gives $\Delta\Delta H^0_{dim}$ and $T(\Delta\Delta S^0_{dim})$ to be -22 and -14 kJ/mol, respectively, at 303 K. Here the negative $\Delta\Delta H^0_{dim}$ represents the hydrogen-bonding dimerization enthalpy per repeating unit, while the negative $T(\Delta\Delta S^0_{dim})$ represents the entropic free-energy loss per repeating unit due to dimerization. Several different factors such as

(20) Our definition of the intrinsic free energy ΔG^0_{int} in this article is different from the definition of intrinsic binding energy used by Jencks. For reference, see: Jencks, W. P. *Proc. Natl. Acad. Sci. U.S.A.* **1981**, *78*, 4046.

(21) (a) Williams, D. H.; Searle, M. S.; Mackay, J. P.; Gerhard, U.; Maplestone, R. A. *Proc. Natl. Acad. Sci. U.S.A.* **1993**, *90*, 1172. (b) Williams, D. H.; Searle, M. S.; Groves, P.; Mackay, J. P.; Westwell, M. S.; Beauregard, D. A.; Cristofaro, M. F. *Pure Appl. Chem.* **1994**, *66*, 1975.

Figure 7. The concentration-dependent absorption spectra of **5** in cyclohexane, in which C_0 was prepared to be (a) 4.2×10^{-6}, (b) 8.4×10^{-6}, (c) 1.68×10^{-5}, (d) 3.36×10^{-5}, (e) 6.72×10^{-5} M. The spectra are normalized at 345 nm. Insert: The plot of $A_0/(A - A_0)$ at, e.g., 355 nm as a function of $\sqrt{1/(A-A_0)}$.

internal rotational restrictions of monomers due to dimer formation or desolvation of the solvent molecules may have contributed to $T(\Delta\Delta S^0_{dim})$. Even though in principle the slope and intercept of the plots to $n = 0$ would give ΔH^0_{int} and $T\Delta S^0_{int}$, respectively, uncertainty due to curve fitting would limit the reliability of these parameters, leading to a less conclusive prediction.

UV–Vis Absorption Measurements. It is of key importance to mimic the intrinsic hydrogen-bonding effect in the nonpolar solvent that provides an environment free from the solvent perturbation such as polar(solute)–polar(solvent) and/or solvent hydrogen-bond interactions. Alternatively, the concentration-dependent absorption spectroscopy offers a reliable method because the dual hydrogen-bond formation of the 2-aminopyridine unit might alter the $S_0 \rightarrow S_1$ (π, π^*) chromophore due to the associated charge-transfer effect.[22] Here, compound **5** was used as a prototype to demonstrate such feasibility. When the concentration was prepared to be as low as 1.2×10^{-6} M, **5** exhibits the lowest singlet $\pi \rightarrow \pi^*$ absorption band maximum at 345 nm ($\epsilon_{345} \approx 4.3 \times 10^4$ M^{-1} cm^{-1}). Upon increasing the concentration, changes in the spectral features were observed in which the spectra after normalization reveal significant red shift (see Figure 7a–e). The results unambiguously conclude the formation of dimer and/or higher-order aggregates through the hydrogen-bonding effect. On the basis of the dimeric structure resolved from X-ray, we first assume a dominant dimeric formation, which possesses a spiral, cyclic type of six hydrogen-bond configurations. The dimerization constant K_d can thus be extracted from eq 2

$$\frac{A_0}{A - A_0} = \sqrt{\frac{l\epsilon_M^2}{\epsilon_D - 2\epsilon_M}} \cdot \sqrt{\frac{1}{K_d}} \cdot \sqrt{\frac{1}{A - A_0}} + \frac{2\epsilon_M}{\epsilon_D - 2\epsilon_M} \quad (2)$$

where A and l denote the initially prepared absorbance at a selected wavelength and cell path length, respectively. ϵ_M and ϵ_D are the molar extinction coefficients of monomer and dimer at the selected wavelength. A_0 is the absorbance of the monomer assuming that no dimer is formed. Experimentally, ϵ_M can be resolved by performing the absorption titration study at a sufficiently low concentration where the monomer exists

Table 6. Values of ΔG^0_{dim}, ΔH^0_{dim}, and $T\Delta S^0_{dim}$ upon Dimerization as a Function of the Repeating Unit of 2-Aminopyridine at 298 K (in kJ mol^{-1})

compound	n	ΔG^0_{dim}	ΔH^0_{dim}	$T\Delta S^0_{dim}$
2	1	$-(7.2 \pm 0.7)$	$-(52 \pm 3)$	$-(45 \pm 3)$
3	2	$-(15.0 \pm 1.5)$	$-(68 \pm 5)$	$-(53 \pm 5)$
5	3	$-(23.3 \pm 2.1)$	$-(86 \pm 5)$	$-(63 \pm 7)$
7	5	$-(39.6 \pm 3.2)$	$-(124 \pm 8)$	$-(84 \pm 10)$

prevalently. A detailed derivation of eq 2 is described in the Appendix. The plot of $A_0/(A - A_0)$ at, for example, 355 nm as a function of $1/(\sqrt{A-A_0})$ shown in the insert of Figure 7 reveals sufficiently linear behavior, supporting the assumption of dimeric formation in **5**. The best linear least-squares fit to the insert of Figure 7 gives a K_d value of $(1.2 \pm 0.5) \times 10^4$ M^{-1} ($\epsilon_D^{355} \approx 8.02 \times 10^4$ M^{-1} cm^{-1}). The hydrogen-bonded association in **5** can be further supported by the concentration-dependent fluorescence spectra of which the fluorescence maximum is gradually red shifted from $\sim$368 nm (4.2×10^{-6} M) to $\sim$378 nm (8.4×10^{-5} M, not shown here).[23] Dual fluorescence lifetime of 3.1 and 1.8 ns originating from monomer and dimer, respectively, was resolved.[23] Temperature-dependent absorption titration spectra were also performed to resolve ΔG^0_{dim} into ΔH^0_{dim} and $T\Delta S^0_{dim}$. The logarithm plot of dimerization constants as a function of the reciprocal of the temperature renders linear behavior, and ΔH^0_{dim} was deduced to be $\sim$−86 kJ/mol for **5**. Similar spectroscopic methods were applied to **2**, **3**, and **7** in cyclohexane where prevalent hydrogen-bonded dimerization upon association was also observed. Accordingly, the best fit of data based on eq 1 gives rise to K_d values of $(1.8 \pm 0.5) \times 10^1$, $(4.2 \pm 1.5) \times 10^2$, and $(8.7 \pm 1.5) \times 10^6$ M^{-1} for **2**, **3**, and **7**,[24] respectively. The sparse solubility of **6** in cyclohexane due to the lack of *tert*-butyl substituents makes the extraction of thermodynamic data upon dimerization infeasible. Figure 6b reveals a plot of the dimerization free energy ΔG^0_{dim} as a function of the number of the repeating 2-aminopyridine units n. Again, as foreseen by the Jorgensen model, the dimerization free energy is linearly proportional to the number of the repeating hydrogen-bond units. A linear least-squares fit of the data based on an empirical correlation of $\Delta G^0_{dim} = n(\Delta\Delta G^0_{dim}) + \Delta G^0_{int}$ results in $\Delta\Delta G^0_{dim}$ and ΔG^0_{int} of −8.3 and 1.5 kJ/mol, respectively. The fact that the value of ΔG^0_{int} in cyclohexane is much smaller than that in $CDCl_3$, indicating the applicability of the Jorgensen model in a nonpolar solvent, is worth mentioning here. Table 6 lists the values of ΔG^0_{dim}, ΔH^0_{dim}, and $T\Delta S^0_{dim}$ (298 K) upon dimerization as a function of the repeating unit of 2-aminopyridine in cyclohexane. The correlation plots of the data obtained from temperature variation experiments versus the number of the repeating units result in $\Delta\Delta H^0_{dim} = -18$ kJ/mol and $T(\Delta\Delta S^0_{dim}) = -9.8$ kJ/mol at 298 K (not shown here).

The enthalpy/entropy compensation effect[21-25] is observed in our system. Figure 8 shows a plot of ΔH^0_{dim} versus $T\Delta S^0_{dim}$ at $T = 298$ K that integrates the data for **2**, **3**, **5**, **6**, and **7** in both solvents. The plot is a sufficiently straight line with a slope of

(22) Chou, P. T.; Wu, G. R.; Wei, C. Y.; Cheng, C. C.; Chang, C. P.; Hung, F. T. *J. Phys. Chem. B* **2000**, *104*, 7818.

(23) To avoid the inner filter effect, a configuration of front-face excitation was applied throughout the fluorescence study.

(24) Because of the large K_d value, a very low concentration of **7** is required to perform the concentration-dependent study. Accordingly, 4 cm and 10 cm path length cells were incorporated in the absorption titration study.

(25) Williams, D. H.; O'Brien, D. P.; Bardsley, B. *J. Am. Chem. Soc.* **2001**, *123*, 737.
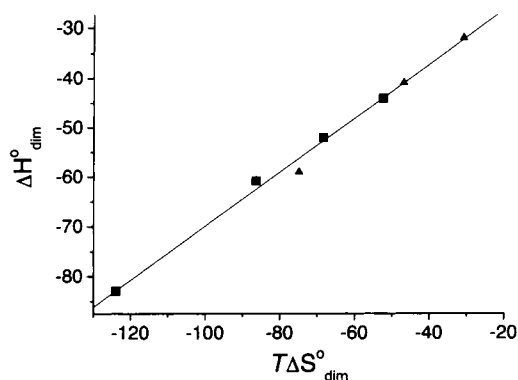
Figure 8. The correlation plot of ΔH_{dim}^0 (kJ mol^{-1}) versus $T\Delta S_{dim}^0$ (kJ mol^{-1}) at 298 K: (▲) data in CDCl$_3$; (■) data in cyclohexane.

0.54, suggesting that around 54% of the enthalpy gain from dimerization interactions would be sacrificed to compensate for the entropic free-energy loss. On the basis of the plot, one could perceive that large decreases in enthalpies are linearly correlated to the decreases in entropies upon dimerization. Data obtained either in cyclohexane or in CDCl$_3$ follow the same correlation. These results could be rationalized by the hydrogen-bond effect. Although the hydrogen-bonding formation between the monomers would gain significant amounts of the enthalpic stabilization energy, the increased hydrogen-bond interactions would reduce internal motions of the monomers, resulting in a loss of entropy. These results also imply the formation of a relatively tighter dimeric pair in cyclohexane than that in CDCl$_3$.

The intrinsic CDCl$_3$—solute interaction may be qualitatively rationalized through an ab initio approach. To simplify the calculations, the terminal N-benzylic groups were replaced with N-methyl groups for **2**—**4**, forming **2-Me**, **3-Me**, and **4-Me**. The initial geometry of monomers and dimers was adopted from X-ray structures for **3** and **4**. As C—H···N interactions have been documented in the literature,[26-28] we first attempted to explore whether chloroform desolvation plays a role in the process of dimerization. Although the C—H bond of chloroform has been shown to be a potential proton donor,[29-32] the proton acceptor ability of a chlorine atom is less obvious. Meanwhile, the interactions between chloroform molecules are quite weak. The complexation energy of the best geometrically optimized chloroform dimer that was located is −1.55 kJ/mol and can thus be neglected. Accordingly, as a crude approximation, it was assumed that prior to the dimerization formation at least one C—H···N interaction has to be broken for each pyridine ring. In other words, one and two chloroform molecules have to be decomplexed from monomeric **2-Me** and **3-Me**, respectively, in advance of dimerization. Note that more solvent molecules in the solvation shell have to be relocated in real solution upon proceeding to dimerization. Nevertheless, our

preliminary approach should provide certain clues about the relative importance of solute—solute and solute—solvent interactions.

Several interesting observations were made from the calculation results. First, all calculated (C—)H···N distances are within the sum of van der Waals radii of H and N (2.6 Å), while all (N—)H···Cl and (C—)H···Cl distances are larger than the sum of van der Waals radii of H and Cl (2.9 Å). In almost all cases, the C—H···N angle is more linear than the N—H···Cl and C—H···Cl angles. The results implied that C—H···N interaction is of primary importance, while the N—H···Cl and C—H···Cl interactions are minor parts. Second, at the B3LYP/6-31+G**// HF/6-31G* level, the gas-phase complexation energies of **2-Me·CHCl$_3$** (−17.45 kJ/mol) and **3-Me·2CHCl$_3$** (−23.47 kJ/mol) are a few kJ/mol smaller than those of (**2-Me**)$_2$ (−28.87 kJ/mol) and (**3-Me**)$_2$ (−42.63 kJ/mol). Thus, the magnitude of the solute—solvent interaction in chloroform is far from negligible. In comparison, much less solvation outcomes can be expected with less polar or acidic solvents such as cyclohexane, consistent with the experimental results. Finally, the dimerization energies of **2-Me**, **3-Me**, and **4-Me** were calculated to be −28.87, −42.63, and −61.63 kJ/mol, respectively, at the B3LYP/6-31+G**//HF/6-31G* level. The plot of ΔE_{dimer} (see Experimental Section) versus the number of the repeating 2-aminopyridine groups shows linear behavior ($R^2 \approx 0.991$, not shown here). However, the increase of complexation energy is not a simple multiple of the number of hydrogen bonds. For example, the complexation energy of (**3-Me**)$_2$ is less than twice that of (**2-Me**)$_2$, possibly due to secondary interactions. In (**2-Me**)$_2$, the unbound N—H group twists out of the molecular plane to avoid secondary interactions. However, for the formation of two additional hydrogen bonds in (**3-Me**)$_2$, the middle N—H group, which corresponds to the unbound N—H bond in (**2-Me**)$_2$, has to be brought back to the vicinity of a neighboring N—H group of the binding partner (see Figures 2 and 3 for reference). For **3-Me·2CHCl$_3$**, the unfavorable dipole—dipole interaction between the two chloroform molecules cancels out some of the favorable solute—solvent interactions. Therefore, decomplexation of the second chloroform molecule becomes relatively easy. A similar trend was applied to oligo-2-aminopyridines with higher repeating n (>3) units. The results qualitatively rationalize the difference in ΔG_{int}, while $\Delta\Delta G_{dim}$ is similar between CDCl$_3$ and cyclohexane. Further detailed studies focusing on the molecular dynamics simulation are in progress.

3. Conclusion

In summary, we have demonstrated a systematic approach to evaluate the strength of hydrogen-bonding interactions. Jorgensen's model can be successfully applied to our systems in cyclohexane. However, the intrinsic free energy ΔG_{int}^0 has to be considered if the dimerization studies are carried out in CDCl$_3$ in which ΔG_{int}^0 is an important parameter that works against the monomers from dimerization. Our results show the enthalpy/ entropy compensation relationship as a competition between bonding and dynamics. Although increasing the number of hydrogen-bonding interactions would definitely enhance the hydrogen-bonding stabilization enthalpy, this stabilization enthalpy per unit would be partially sacrificed to compensate for the entropic free-energy loss due to dimerization in our cases.

(26) (a) Desiraju, G. R. *Angew. Chem., Int. Ed. Engl.* **1995**, *34*, 2311−2327 and references therein. (b) Marjo, C. E.; Bishop, R.; Craig, D. C.; Scudder, M. L. *Eur. J. Org. Chem.* **2001**, 863.

(27) Hilfiker, M. A.; Mysak, E. R.; Samet, C.; Maynard, A. *J. Phys. Chem. A* **2001**, *105*, 3087.

(28) Gu, Y.; Kar, T.; Scheiner, S. *J. Mol. Struct.* **2000**, *552*, 17−31.

(29) (a) Desiraju, G. R. *J. Chem. Soc., Chem. Commun.* **1989**, 179. (b) Desiraju, G. R. *Acc. Chem. Res.* **1991**, *24*, 290−296.

(30) Jemmis, E. D.; Giju, K. T.; Sundararajan, K.; Sankaran, K.; Vidya, V.; Viswanathan, K. S.; Leszczynski, J. *J. Mol. Struct.* **1999**, *510*, 59.

(31) Our calculation at the MP2/6-31G** level estimated the BSSE corrected binding energy of CHCl$_3$···NH$_3$ complex to be −23.26 kJ/mol.

(32) Pawelka, Z.; Koll, A.; Zeegers-Huyskens, Th. *J. Mol. Struct.* **2001**, *597*, 57.

These results clearly support the importance of "the concept of preorganization"[33–35] in the design of hydrogen-bonding guest—host molecules.

4. Experimental Section

4.1. Materials. Tris(dibenzylideneacetone)dipalladium(0) (Pd$_2$(dba)$_3$, 2,2'-bis(diphenylphosphino)-1,1'-binaphthyl (BINAP), potassium-*tert*-butoxide (KO-*t*Bu), and 18-crown-6 were obtained commercially (Aldrich, Janssan, Tokyo Kasei) and used as received. Benzene was refluxed over calcium hydride for 8 h before use.

4.2. General Procedures for Synthesizing 2—7. A mixture of the corresponding bromide and amine, Pd$_2$(dba)$_3$, BINAP, KO-*t*Bu, and 18-crown-6 in dry benzene (10 mL) was refluxed at 80 °C under argon with constant stirring. After reacting for a specified time period, the reaction mixture was cooled and quenched with NH$_4$Cl solution (2 mL). The product was extracted twice with CH$_2$Cl$_2$. The extracts were combined and washed with H$_2$O (2 mL), dried over anhydrous MgSO$_4$, and concentrated under reduced pressure to provide a crude oil, which was further purified by column chromatography over silica gel. In most cases, a mixture of ethyl acetate and hexane is a suitable eluent for column chromatography. Although the products isolated by this approach are reasonably good in their NMR spectra and elemental analysis, the products usually contained trace amounts of brown impurity that would significantly affect the experiments in the UV—vis analysis. Therefore, compounds **2, 3, 5,** and **7** were further purified through column chromatography (diethyl ether) to remove the brown impurity before analysis.

Bis[6-(benzylamino)pyrid-2-yl]amine (3). The reaction of (*N*-benzyl)pyridine-2,6-diamine (**8**) (0.199 g, 1 mmol) and 2-(*N*-benzyl-amino)-6-bromopyridine (**10**) (0.262 g, 1 mmol) in the presence of Pd$_2$-(dba)$_3$ (0.010 g, 1 mol %), BINAP (0.012 g, 2 mol %), and KO-*t*Bu (0.448 g, 4 mmol) in benzene (10 mL) for 8 h gave a crude product **3**. Purification by column chromatography over silica gel, using hexane/EtOAc (4:1) as eluent, gave the pure bis[6-(benzylamino)pyrid-2-yl]-amine (**3**) (0.304 g, 79% yield) as colorless crystals. R_f 0.50 (hexane/EtOAc, 7:3). mp 131 °C. IR (KBr): 3421, 3265, 1610 cm^{-1}. ^{1}H NMR (200 MHz, DMSO-d_6): δ 8.47 (s, 1H, NH), 7.36—7.09 (m, 12H), 6.77 (d, *J* = 8.0 Hz, 2H), 6.73 (t, *J* = 6 Hz, 2H, NH), 5.93 (d, *J* = 8.0 Hz, 2H), 4.46 (d, *J* = 6 Hz, 4H). ^{13}C NMR (100 MHz, DMSO-d_6): δ 158.89, 139.63, 139.43, 139.37, 128.19, 127.27, 126.65, 114.05, 106.53, 44.18. EI-MS: 381 [M$^+$]. Anal. Calcd for C$_{24}$H$_{23}$N$_5$: C, 75.55; H, 6.08; N, 18.37. Found: C, 75.19; H, 6.15; N, 18.86.

N^2,*N*^{6}-**Bis[6'-(benzylamino)pyrid-2'-yl]pyridine-2,6-diamine (4).** The reaction of (*N*-benzyl)pyridine-2,6-diamine (**8**) (0.398 g, 2 mmol) and 2,6-dibromopyridine (0.237 g, 1 mmol) in the presence of Pd$_2$-(dba)$_3$ (0.021 g, 2 mol %), BINAP (0.025 g, 4 mol %), KO-*t*Bu (0.56 g, 5 mmol), and 18-crown-6 (1.3 gm, 5 mmol) in benzene (20 mL) for 16 h gave a crude **4**. Purification by column chromatography over silica gel, using hexane/EtOAc (7:3) as eluent, gave **4** (0.34 g, 72% yield) as yellow crystals. R_f 0.45 (hexane/EtOAc, 7:3). mp 188 °C. IR (KBr): 3437, 3232, 1604 cm^{-1}. ^{1}H NMR (300 MHz, DMSO-d_6): δ 8.67 (s, 2H, NH), 7.37—7.20 (m, 13H), 7.12 (d, *J* = 7.8 Hz, 2H), 6.85—6.81 (m, 4H), 6.00 (d, *J* = 7.8 Hz, 2H), 4.49 (d, *J* = 6 Hz, 4H). ^{13}C NMR (100 MHz, DMSO-d_6): δ 157.45, 153.14, 152.68, 140.97, 138.14, 138.09, 128.14, 127.07, 126.40, 102.64, 98.90, 98.72, 44.32. FAB-MS: *m/z* 473 [M$^+$]. Anal. Calcd for C$_{29}$H$_{27}$N$_7$: C, 73.53; H, 5.74; N, 20.71. Found: C, 73.20; H, 5.73; N, 20.73.

N^2,*N*^{6}-**Bis[6'-(3'',5''-di-*tert*-butylbenzylamino)pyrid-2'-yl]pyridine-2,6-diamine (5).** The reaction of *N*-(3',5'-di-*tert*-butylbenzyl)pyridine-

2,6-amine (**9**) (0.622 g, 2 mmol) and 2,6-dibromopyridine (0.237 g, 1 mmol) in the presence of Pd$_2$(dba)$_3$ (0.021 g, 2 mol %), BINAP (0.025 g, 4 mol %), and KO-*t*Bu (0.448 g, 4 mmol) in benzene (20 mL) for 8 h gave a crude **5**. Purification by column chromatography over silica gel, using hexane/EtOAc (7:3) as eluent, gave pure **5** (0.468 g, 67% yield) as yellow solid. R_f 0.50 (hexane/EtOAc, 4:1). mp 120 °C. IR (KBr): 3409, 3229, 1614 cm^{-1}. ^{1}H NMR (400 MHz, CDCl$_3$): δ 8.75 (s, 2H, NH), 7.44—7.21 (m, 9H), 7.11 (d, *J* = 7.6 Hz, 2H), 6.59 (d, *J* = 8.0 Hz, 2H), 5.96 (d, *J* = 8.0 Hz, 2H), 5.25 (bs, 2H, NH), 4.40 (d, *J* = 5.6 Hz, 4H), 1.31 (s, 36H). ^{13}C NMR (100 MHz, CDCl$_3$): δ 158.53, 153.67, 153.52, 150.95, 139.16, 139.05, 138.18, 121.54, 121.08, 103.24, 99.73, 97.72, 47.27, 34.77, 31.42. FAB-MS: 697 [M$^+$]. Anal. Calcd for C$_{45}$H$_{59}$N$_7$: C, 77.42; H, 8.53; N, 14.05. Found: C, 77.46; H, 8.60; N, 13.91.

Bis{6-[6'-(benzylamino)pyrid-2'-yl)amino]pyrid-2-yl}amine (6). The reaction of *N*^{6}-(6'-bromopyrid-2-yl)-*N*^{2}-(6''-(benzylamino)pyrid-2-yl)pyridine-2,6-diamine (**13**) (0.446 g, 1 mmol) and (*N*-benzyl)-pyridine-2,6-diamine (**8**) (0.199 g, 1 mmol) in the presence of Pd$_2$(dba)$_3$ (0.021 g, 2 mol %), BINAP (0.025 g, 4 mol %), KO-*t*Bu (0.448 g, 4 mmol), and 18-crown-6 (0.65 g, 2.5 mmol) in benzene (10 mL) for 8 h gave a crude **6**. Purification by column chromatography over silica gel (CH$_2$Cl$_2$/acetone, 24:1) gave pure **6** (0.362 g, 64% yield) as a brown solid. R_f 0.38 (hexane:EtOAc, 3:2). mp 181 °C. IR (KBr): 3421, 3195, 1602, 1580 cm^{-1}. ^{1}H NMR (400 MHz, CDCl$_3$): δ 10.17 (s, 1H, NH), 9.73 (s, 2H, NH), 7.41 (t, *J* = 8 Hz, 2H), 7.29—7.18 (m, 12H), 6.99 (d, *J* = 8 Hz, 2H), 6.82 (d, *J* = 8 Hz, 2H), 6.53 (d, *J* = 8 Hz, 2H), 5.86 (d, *J* = 8 Hz, 2H), 5.62 (bs, 2H, NH), 4.35 (d, *J* = 5.6 Hz, 4H). ^{13}C NMR (100 MHz, DMSO-d_6): δ 157.45, 153.12, 152.68, 152.58, 140.93, 138.37, 138.11, 128.14, 127.06, 126.40, 102.92, 102.86, 98.92, 98.72, 44.35. FAB-MS: 565 [M$^+$]. HRMS calcd for C$_{34}$H$_{31}$N$_9$, 565.2702; found, 565.2698.

N^2,*N*^{6}-{6'-[6''-(3''',5'''-Di-*tert*-benzylamino)pyrid-2''-yl)amino]pyrid-2'-yl}pyridine-2,6-diamine (7). The reaction of *N*-(3',5'-di-*tert*-butylbenzyl)pyridine-2,6-amine (**9**) (0.622 g, 2 mmol) and *N*^{2},*N*^{6}-bis(6'-bromopyrid-2'-yl)pyridine-2,6-diamine (**12**) (0.419 g, 1 mmol) in the presence of Pd$_2$(dba)$_3$ (0.032 g, 3 mol %), BINAP (0.038 g, 6 mol %), KO-*t*Bu (0.56 g, 5 mmol), and 18-crown-6 (0.528 g, 2 mmol) in benzene (10 mL) for 8 h gave a crude **7**. Purification by column chromatography over silica gel (hexane/EtOAc, 3:2) gave pure **7** (581 mg, 66%) as a yellow solid. R_f 0.58 (hexane:EtOAc, 7:3). mp 139 °C. IR (KBr): 3418, 3228, 3201, 1613 cm^{-1}. ^{1}H NMR (400 MHz, CDCl$_3$): δ 11.39 (s, 2H, NH), 10.70 (bs, 2H, NH), 7.44—7.40 (m, 3H), 7.20—7.36 (m, 6H), 7.19 (s, 4H), 7.07 (bs, 2H), 6.76 (m, 4H), 6.46 (d, *J* = 8.0 Hz, 2H), 5.90 (d, *J* = 8 Hz, 2H), 4.38 (bs, 4H), 1.23 (s, 36H). ^{13}C NMR (100 MHz, CDCl$_3$): δ 154.65, 154.61, 154.39, 153.92, 151.01, 150.98, 139.33, 139.25, 139.16, 138.16, 121.24, 121.01, 103.68, 103.14, 102.86, 99.75, 97.56, 47.33, 34.78, 31.43. FAB-MS: 881 [M$^-$]. Anal. Calcd for C$_{55}$H$_{67}$N$_{11}$: C, 74.87; H, 7.66; N, 17.47. Found: C, 74.06; H, 7.62; N, 16.96.

N-(3',5'-Di-*tert*-butylbenzyl)pyridine-2,6-diamine (9). To a mixture of 2,6-diaminopyridine (1.09 g, 0.01 mol) and KO-*t*Bu (2.24 g, 0.02 mol) in dry benzene (30 mL) was added a solution 3,5-di-*tert*-butylbenzylbromide (2.83 g, 0.01 mol) in benzene (5 mL) at room temperature with constant stirring. The mixture was refluxed at 80 °C for 6 h. After cooling, the crude mixture was quenched with saturated solution of NH$_4$Cl (4 mL), washed with water (4 mL), and dried over anhydrous MgSO$_4$. The solvent was removed, and the crude product was chromatographed over silica gel (hexane/EtOAc, 3:1) to give **9** (2.36 g, 76%) as a light brown thick liquid. R_f 0.32 (hexane/EtOAc, 4:1). IR (KBr): 3476, 3380, 3302, 1609 cm^{-1}. ^{1}H NMR (400 MHz, CDCl$_3$): 7.44 (t, *J* = 1.6 Hz, 1H), 7.23—7.30 (m, 3H), 5.85—5.88 (m, 2H), 4.96 (t, *J* = 5.6 Hz, 1H), 4.18—4.20 (m, 4H), 1.41 (2, 18H). ^{13}C NMR (100 MHz, CDCl$_3$): 31.29, 34.59, 47.03, 95.16, 96.79, 120.88, 121.65, 138.15, 139.12, 150.71, 157.57, 158.12. MS: *m/z* (EI 70 eV) 311 (M$^+$, 100). Anal. Calcd for C$_{20}$H$_{29}$N$_3$: C, 77.11; H, 9.39; N, 13.50. Found: C, 76.83; H, 9.29; N, 13.34.

(33) Cram, D. J. *Angew. Chem., Int. Ed. Engl.* **1986**, *25*, 1039.
(34) Martell, A. E.; Hancock, R. D.; Motekaitis, R. J. *Coord. Chem. Rev.* **1994**, *133*, 39.
(35) For recent examples based on the concept of preorganization, see: (a) Bell, T. W.; Khasanov, A. B.; Drew, M. G. B.; Filikov, A.; James, T. L. *Angew. Chem., Int. Ed.* **1999**, *38*, 2543. (b) Bell, T. W.; Hou, Z.; Zimmerman, S. C.; Thiessen, P. A. *Angew. Chem., Int. Ed. Engl.* **1995**, *34*, 2163.

Preparation of N^2,N^6-Dibenzylpyridine-2,6-diamine (2) and 2-N-Benzylamino-6-bromopyridine (10).

To a magnetically stirred solution of 2,6-dibromopyridine (2.37 g, 0.01 mol), KO-*t*Bu (1.40 g, 0.0125 mol), Pd₂(dba)₃ (0.025 mg, 0.25 mol %), and BINAP (30 mg, 0.5 mol %) in dry benzene (40 mL) was added benzylamine (1.09 mL, 0.01 mol) dropwise at room temperature under argon atmosphere. The reaction mixture was refluxed at 80 °C for 4 h. After cooling, the reaction mixture was quenched with saturated NH₄Cl solution (4 mL), washed with H₂O (4 mL), and dried over anhydrous MgSO₄. The solvent was removed under vacuum, and purification by column chromatography over silica gel (hexane/EtOAc, 19:1) gave 2-benzylamino-6-bromopyridine (10) (575 mg, 22%) as colorless crystals. R_f 0.47 (hexane/EtOAc, 9:1). mp 88 °C. IR (KBr): 3288, 3084, 1606, 1566 cm⁻¹. ¹H NMR (200 MHz, DMSO-d_6): 7.45 (t, $J = 6$ Hz, 1H, NH), 7.19−7.32 (m, 6H), 6.63 (d, $J = 8$ Hz, 1H), 6.46 (d, $J = 8$ Hz, 1H), 4.40 (d, $J = 6.0$ Hz, 2H). ¹³C NMR (100 MHz, DMSO-d_6): 44.24, 98.61, 126.32, 127.03, 128.06, 137.86, 140.96, 153.16, 157.38. MS: *m/z* (EI, 70 eV) 264 (M⁺ + 2), 262 (M⁺). HRMS (M⁺) calcd for $C_{12}H_{11}^{79}BrN_2$, 262.0105; found, 262.0099. Also gave N^2,N^6-dibenzylpyridine-2,6-diamine (2) (490 mg, 17%) as colorless crystals. R_f 0.7 (hexane/EtOAc, 4:1). ¹H NMR (400 MHz, CDCl₃): δ 7.41−7.23 (m, 11H), 5.78 (d, $J = 8$ Hz, 2H), 4.84 (t, $J = 5.6$ Hz, 2H, NH), 4.48 (d, $J = 5.6$ Hz, 4H). ¹³C NMR (100 MHz, CDCl₃): δ 157.91, 139.69, 138.93, 128.34, 127.25, 126.82, 95.00, 46.11.

Preparation of N-(6′-Bromopyrid-2′-yl)pyridine-2,6-diamine (11) and N^2,N^6-Bis(6′-bromopyrid-2′-yl)pyridine-2,6-diamine (12).

To a mixture of 2,6-diaminopyridine (1 g, 0.009 mol) and 2,6-dibromopyridine (2.17 g, 0.009 mol) in dry benzene (10 mL) was added KO-*t*Bu (2.06 g, 0.018 mol) at room temperature under N₂ atmosphere with constant stirring. The reaction mixture was refluxed at 80 °C for 16 h. After cooling, the crude mixture was quenched with saturated NH₄Cl solution (2 mL), washed with H₂O (2 mL), and dried over anhydrous MgSO₄. The solvent was removed under vacuum, and the product was recrystallized from CH₂Cl₂ to give N^2,N^6-bis(6′-bromopyrid-2′-yl)-pyridine-2,6-diamine (12) (310 mg, 8%) as a brown solid. R_f 0.68 (CH₂Cl₂). IR (KBr): 3262, 3256, 3089, 3067, 3031, 1556 cm⁻¹. ¹H NMR (200 MHz, DMSO-d_6): 7.03 (d, $J = 8.0$ Hz, 2H), 7.04 (d, $J = 8.0$ Hz, 2H), 7.57 (t, $J = 7.8$ Hz, 2H), 7.58 (t, $J = 7.9$ Hz, 2H), 7.84 (d, $J = 8.2$ Hz, 1H), 9.84 (s, 2H). ¹³C NMR (100 MHz, DMSO-d_6): 103.9, 110.4, 118.6, 138.4, 139.2, 140.4, 151.8, 154.2. FAB-MS: *m/z* 419 (M⁺). Anal. Calcd for $C_{15}H_{11}N_5Br_2$: C, 42.79; H, 2.63; N, 16.63. Found: C, 42.98; H, 2.67; N, 16.43. The remaining crude mixture was purified by column chromatography over silica gel (CH₂Cl₂) to give N-(6′-bromopyrid-2′-yl)pyridine-2,6-diamine (11) (1.36 g, 56%) as a light brown solid. R_f 0.24 (CH₂Cl₂). IR (KBr): 3443, 3305, 3198, 1633, 1570 cm⁻¹. ¹H NMR (200 MHz, DMSO-d_6): 5.76 (bs, 2H), 5.98 (d, *J* = 7.0 Hz, 1H), 6.55 (d, $J = 7.8$ Hz, 1H), 6.96 (d, $J = 7.6$ Hz, 1H), 7.25 (t, *J* = 7.8 Hz, 1H), 7.49 (t, *J* = 8.0 Hz, 2H), 8.03 (d, *J* = 8.3 Hz, 1H), 9.53 (s, 1H). ¹³C NMR (100 MHz, DMSO-d_6): 98.9, 99.8, 110.2, 117.9, 138.3, 138.5, 140.1, 152.4, 154.7, 158.2. FAB-MS: *m/z* 264 (M⁺). Anal. Calcd for $C_{10}H_9N_4Br$: C, 45.45; H, 3.44; N, 21.22. Found: C, 45.55; H, 3.47; N, 20.72.

N-(6′-Bromo-2′-pyridyl)-N′-(6″-N-benzylamino-2″-pyridyl)-2,6-diaminopyridine (13).

To a magnetically stirred solution of 2-N-benzylamino-6-bromopyridine (10) (524 mg, 2 mmol) and N-(6′-bromopyrid-2′-yl)pyridine-2,6-diamine (11) (264 mg, 1 mmol) in dry benzene (20 mL) were added KO-*t*Bu (280 mg, 2.5 mmol), Pd₂(dba)₃ (21 mg, 2 mol %), BINAP (25 mg, 4 mol %), and 18-crown-6 (528 mg, 2 mmol) at room temperature under argon atmosphere. The stirring was continued at 80 °C for 4 h. After cooling, the reaction mixture was quenched with saturated NH₄Cl solution (4 mL), washed with H₂O (4 mL), and dried over anhydrous MgSO₄. The crude mixture was purified over silica gel to yield 13 (170 mg, 38%) as colorless crystals. R_f 0.62 (hexane:EtOAc, 7:3). mp 168 °C. IR (KBr): 3288, 3192, 3020, 1603, 1582 cm⁻¹. ¹H NMR (300 MHz, DMSO-d_6): 9.72 (s, 1H, NH),

8.90 (s, 1H, NH), 8.17 (d, $J = 8.1$ Hz, 1H), 7.54 (t, $J = 7.8$ Hz, 1H), 7.17−7.41 (m, 8H), 7.01 (d, $J = 7.5$ Hz, 1H), 6.90 (t, $J = 6.0$ Hz, 1H, NH), 6.76 (dd, $J = 6.1$ and 2.2 Hz, 1H), 6.58 (d, $J = 7.8$ Hz, 1H), 6.00 (d, $J = 8.1$ Hz, 1H), 4.48 (d, $J = 6.0$ Hz, 2H). ¹³C NMR (100 MHz, DMSO-d_6): 44.40, 98.65, 98.96, 102.89, 103.55, 110.45, 118.46, 126.42, 127.03, 128.16, 138.11, 138.45, 138.68, 140.38, 140.91, 151.97, 152.60, 153.12, 154.49, 157.52. FAB-MS: *m/z* 448 (M⁺ + 2), 446 (M⁺). Anal. Calcd for $C_{22}H_{19}BrN_6$: C, 59.07; H, 4.28; N, 18.79. Found: C, 58.54; H, 4.24; N, 18.52.

4.3. Methods. ¹H and ¹³C NMR were recorded in CDCl₃ or DMSO-d_6, and chemical shifts were reported in ppm relative to CHCl₃ (δ 7.24 ppm for ¹H and 77.0 ppm for ¹³C) or DMSO-d_6 (δ 2.49 ppm for ¹H and 39.5 ppm for ¹³C). Melting points were uncorrected. The variable-concentration ¹H NMR measurements (400 MHz) for **2**, **3**, **5**, **6**, and **7** were run in CDCl₃, using the signal of CHCl₃ (δ = 7.25) as the internal standard. Before use, CDCl₃ was treated with K₂CO₃ to remove any acidic impurity, dried over molecular sieves 4 Å, and distilled. Experimental details for the concentration-dependent chemical shifts are provided in the Supporting Information.

For the electrospray ionization mass spectroscopy (ESI-MS), a Finnigan LCQ quadruple ion trap mass spectrometer equipped with a pneumatically assisted electrospray ionization source was used. The mass spectrometer was operated in the positive ion mode by applying a voltage of 4.5 kV to the ESI needle. The temperature of the heated capillary in the ESI source was set at 200 °C. To avoid a space charge effect, the number of ions present in the trap at one time was regulated by automatic gain control, which was set at 5 × 10⁷ ions for the full-mass target. The flow rate of the sheath gas of nitrogen was set at 30 units. Helium was used as the damping gas at a pressure of 10⁻³ Torr. Voltage across the capillary and the octapole lenses was tuned by an automated procedure to maximize signals from the ion of interest in the mass spectrum.

Steady-state absorption and emission spectra were recorded by a U-3310 (Hitachi) spectrophotometer and a F4500 (Hitachi) fluorimeter, respectively. The sample compartment of U-3310A was attached by a temperature-controlled unit so that temperature variation studies can be performed within −10 to 80 °C. Because the titration experiment is critical for interpretation of the hydrogen-bonding association, we have carefully performed our absorption and fluorescence titration studies where each piece of data was acquired from an average of three to five measurements. The sensitivity for the absorption measurement is approximately 1.5 × 10⁻⁴ in absorbance under constant temperature (±0.1 °C) throughout the measurement.

Ab initio calculation was carried out using Gaussian 98.[36] Geometry optimization and frequency analyses were carried out at the HF/6-31G* level. All stationary points were verified by performing vibrational analyses. Dimerization energies reported were results of single point calculations of $\Delta E_{dimer} = E_{dimer} - 2E_{monomer}$, with counterpoise corrections for basis set superposition errors (BSSE), at the B3LYP[37,38]/6-31+G** level.

For the crystal structure determinations, data collection was carried out on a Siemens SMART diffractometer with a CCD detector (Mo Kα radiation, $\lambda = 0.71073$ Å) at room temperature. A preliminary

(36) Frisch, M. J.; Trucks, G. W.; Schlegel, H. B.; Scuseria, G. E.; Robb, M. A.; Cheeseman, J. R.; Zakrzewski, V. G.; Montgomery, J. A., Jr.; Stratmann, R. E.; Burant, J. C.; Dapprich, S.; Millam, J. M.; Daniels, A. D.; Kudin, K. N.; Strain, M. C.; Farkas, O.; Tomasi, J.; Barone, V.; Cossi, M.; Cammi, R.; Mennucci, B.; Pomelli, C.; Adamo, C.; Clifford, S.; Ochterski, J.; Petersson, G. A.; Ayala, P. Y.; Cui, Q.; Morokuma, K.; Malick, D. K.; Rabuck, A. D.; Raghavachari, K.; Foresman, J. B.; Cioslowski, J.; Ortiz, J. V.; Stefanov, B. B.; Liu, G.; Liashenko, A.; Piskorz, P.; Komaromi, I.; Gomperts, R.; Martin, R. L.; Fox, D. J.; Keith, T.; Al-Laham, M. A.; Peng, C. Y.; Nanayakkara, A.; Gonzalez, C.; Challacombe, M.; Gill, P. M. W.; Johnson, B. G.; Chen, W.; Wong, M. W.; Andres, J. L.; Head-Gordon, M.; Replogle, E. S.; Pople, J. A. *Gaussian 98*, revision A.7; Gaussian, Inc.: Pittsburgh, PA, 1998.
(37) Becke, A. D. *J. Chem. Phys.* **1993**, *98*, 5648.
(38) (a) Lee, C., Yang, W.; Parr, R. G. *Phys. Rev. B* **1988**, *37*, 785. (b) Miehlich, B.; Savin, A.; Stoll, H.; Preuss, H. *Chem. Phys. Lett.* **1989**, *157*, 200.

orientation matrix and unit cell parameters were determined from three runs of 15 frames each. each frame corresponding to 0.3° scan in 20 s. followed by spot integration and least-squares refinement. For each structure, data were measured using ω scans of 0.3° per frame for 20 s until a complete hemisphere had been collected. Cell parameters were retrieved using SMART[39] software and refined with SAINT on all observed reflections. Data reduction was performed with the SAINT[40] software and corrected for Lorentz and polarization effects. Absorption corrections were applied with the program SADABS.[40] The structures of **2a**, **2b**, **3**, and **4** are solved by direct methods with the SHELX-93[41] program and refined by full-matrix least-squares methods on F^2 with SHEXLTL-PC V 5.03.[42] All non-hydrogen atomic positions were located in difference Fourier maps and refined anisotropically. Hydrogen atoms attached to nitrogen atoms were located and refined isotropically. The rest of the hydrogen atoms attached to carbon atoms were fixed at calculated positions and refined using a riding mode. Detailed crystal data of **2a**, **2b**, **3**, and **4** are listed in Table 1, and the bond lengths and angles are deposited in the Supporting Information (CIF files).

Crystal Data of 2a. Single crystals of **2** were obtained by recrystallization from hexanes/ethyl acetate. A light-yellow crystal of approximate dimensions $0.4 \times 0.4 \times 0.25$ mm^3 was mounted on a glass capillary. A total of 17 886 reflections was collected with a final resolution of 0.75 Å. Sadabs absorption correction (T_{min} 0.819 and T_{max} 0.928) and 4217 unique reflections ($2\theta < 50°$, $R_{int} = 0.0867$) were used in the refinement. Full-matrix least-squares refinement on F^2 converged to $R_F = 0.0763$ [$I > 2\sigma(I)$], 0.1479 (all data) and $R_w(F^2) = 0.1785$ [$I > 2\sigma(I)$], 0.2195 (all data).

Crystal Data of 2b. A light-yellow crystal of approximate dimensions $0.60 \times 0.12 \times 0.06$ mm^3 was mounted on a glass capillary. A total of 6396 reflections was collected with a final resolution of 0.75 Å. Sadabs absorption correction (T_{min} 0.783 and T_{max} 0.928) and 4529 unique reflections ($2\theta < 50°$, $R_{int} = 0.0412$) were used in the refinement. Full-matrix least-squares refinement on F^2 converged to $R_F = 0.0583$ [$I > 2\sigma(I)$], 0.0912 (all data) and $R_w(F^2) = 0.1067$ [$I > 2\sigma(I)$], 0.1236 (all data).

Crystal Data of 3. Single crystals of **3** were obtained by recrystallization from hexanes/ethyl acetate. A light-yellow crystal of approximate dimensions $0.40 \times 0.20 \times 0.05$ mm^3 was mounted on a glass capillary. A total of 25 990 reflections was collected with a final resolution of 0.75 Å. Sadabs absorption correction (T_{min} 0.675 and T_{max} 0.928) and 7296 unique reflections ($2\theta < 50°$, $R_{int} = 0.0590$) were used in the refinement. Full-matrix least-squares refinement on F^2 converged to $R_F = 0.0611$ [$I > 2\sigma(I)$], 0.1349 (all data) and $R_w(F^2) = 0.1188$ [$I > 2\sigma(I)$], 0.1500 (all data).

Crystal Data of 4. Single crystals of **4** were obtained by recrystallization from hexanes/ethyl acetate. A light-yellow crystal of approximate dimensions $0.20 \times 0.15 \times 0.10$ mm^3 was mounted on a glass capillary. A total of 25 402 reflections was collected with a final resolution of 0.75 Å. Sadabs absorption correction (T_{min} 0.796 and T_{max} 0.928) and 4346 unique reflections ($2\theta < 50°$, $R_{int} = 0.0917$) were used in the refinement. Full-matrix least-squares refinement on F^2 converged to $R_F = 0.0796$ [$I > 2\sigma(I)$], 0.1338 (all data) and $R_w(F^2) = 0.1410$ [$I > 2\sigma(I)$], 0.1658 (all data).

(39) *SMART V 4.043 Software for the CCD Detector System*; Siemens Analytical Instruments Division: Madison, WI, 1995.

(40) *SAINT V 4.045 Software for the CCD Detector System*; Siemens Analytical Instruments Division: Madison, WI, 1995.

(41) Sheldrick, G. M. *SHELXL-93, Program for the Refinement of Crystal Structure*; University of Göttingen: Göttingen, Germany, 1993.

(42) *SHELXTL 5.03 (PC-Version), Program Library for Structure Solution and Molecular Graphics*; Siemens Analytical Instruments Division: Madison, WI, 1995.

Appendix

Derivation of Eq 2. A competitive equilibrium between monomer and dimer of oligo-α-aminopyridines (OAP) can be depicted as 2(OAP) $\rightleftharpoons$ (OAP)$_2$, and the dimerization constant K_d for the formation of the OAP dimer can be expressed as

$$K_d = \frac{C_p}{(C_0 - 2C_p)^2} \tag{a}$$

where C_0 is the initial concentration of OAP, and C_p denotes the concentration of the OAP dimeric form. The rearrangement of eq a leads to

$$\frac{C_0}{C_p} = \sqrt{\frac{1}{K_d C_p}} + 2 \tag{b}$$

Under equilibrium the absorbance A at any selected wavelength can be expressed as

$$A = \epsilon_D C_p l + \epsilon_M (C_0 - 2C_p)l = (\epsilon_D - 2\epsilon_M)C_p l + C_0 \epsilon_M l$$

$$\therefore C_p = \frac{A - C_0 \epsilon_M l}{(\epsilon_D - 2\epsilon_M)l} \tag{c}$$

where l is the cell length, and ϵ_M and ϵ_D denote the molar extinction coefficient of monomer and dimer, respectively. Combining eqs b and c, one obtains

$$\frac{C_0 l(\epsilon_D - 2\epsilon_M)}{A - C_0 \epsilon_M l} = \sqrt{\frac{(\epsilon_D - 2\epsilon_M)l}{K_d(A - C_0 \epsilon_M l)}} + 2 \tag{d}$$

Dividing ($\epsilon_D - 2\epsilon_M$) on each side leads to eq e.

$$\frac{C_0 l}{A - C_0 \epsilon_M l} = \sqrt{\frac{l}{K_d(\epsilon_D - 2\epsilon_M)}} \sqrt{\frac{1}{(A - C_0 \epsilon_M l)}} + \frac{2}{\epsilon_D - 2\epsilon_M} \tag{e}$$

By multiplying ϵ_M on each side and applying the Beer–Lambert law, eq e can be rewritten to obtain eq 2

$$\frac{A_0}{A - A_0} = \sqrt{\frac{l\epsilon_M^2}{K_d(\epsilon_D - 2\epsilon_M)}} \sqrt{\frac{1}{(A - C_0 \epsilon_M l)}} + \frac{2\epsilon_M}{\epsilon_D - 2\epsilon_M} \tag{2}$$

where A_0 in eq 2 simply denotes the absorbance of the monomer assuming that no dimer is formed at the prepared concentration. ϵ_M can be derived by performing the concentration-dependent study at a sufficiently low concentration so that only monomer mainly exists. By knowing the proportionality of the dilution, A_0 values can thus be obtained in each prepared concentration. Knowing ϵ_M at the analyzed wavelength, K_d can be deduced by intercept/(slope)^2 = $2K_d/l\epsilon_M$.

Supporting Information Available: CIF files containing detailed crystal data of **2a**, **2b**, **3**, and **4**. Original ^{1}H and ^{13}C NMR spectra of **2**–**9** and **10**–**13**. Experimental details for the NH's chemical shifts collected from the concentration-dependent experiments (PDF). These materials are available free of charge via the Internet at http://pubs.acs.org.

JA011679P

2,7-Bis(1H-pyrrol-2-yl)ethynyl-1,8naphthyridine: An Ultrasensitive Fluorescent Probe for Glucopyranoside

Jen-Hai Liao, Chao-Tsen Chen, He-Chun Chou, Chung-Chih Cheng, Pi-Tai Chou, Jim-Min Fang, Zdenek Slanina, and Tashin J. Chow

Department of Chemistry, National Taiwan University, Taipei, 106, Taiwan, and Institute of Chemistry, Academia Sinica, Nankang, 115, Taiwan, Republic of China
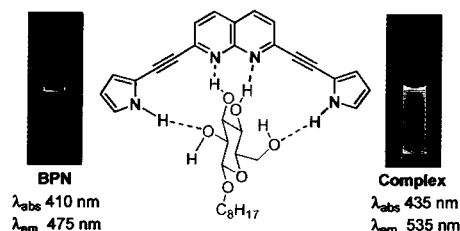
2,7-Bis(1H-pyrrol-2-yl)ethynyl-1,8-naphthyridine: An Ultrasensitive Fluorescent Probe for Glucopyranoside

Jen-Hai Liao,[†] Chao-Tsen Chen,[*,†] He-Chun Chou,[†] Chung-Chih Cheng,[†,§]
Pi-Tai Chou,[*,†] Jim-Min Fang,[*,†] Zdenek Slanina,[‡] and Tashin J. Chow[‡]

*Department of Chemistry, National Taiwan University, Taipei, 106, Taiwan,
and Institute of Chemistry, Academia Sinica, Nankang, 115, Taiwan, Republic of China*

jmfang@ccms.ntu.edu.tw

Received June 21, 2002

ABSTRACT

BPN
λ_{abs} 410 nm
λ_{em} 475 nm

Complex
λ_{abs} 435 nm
λ_{em} 535 nm

A push–pull conjugated molecule, 2,7-bis(1H-pyrrol-2-yl)ethynyl-1,8-naphthyridine (BPN), has been designed to bind selectively with octyl glucopyranoside (OGU). The BPN/OGU quadruple hydrogen-bonding complex adopts a rigid BPN conformation in which the *proton donor (d) and acceptor (a)* relays (*daad*) are resonantly conjugated through the ethynyl bridge, inducing π-electron delocalization, i.e., a charge transfer effect. The excellent photophysical properties make BPN a highly sensitive probe for monitoring glucopyranoside to a detection limit of ~100 pM.

The hydrogen-bonding recognition for carbohydrates[1,2] affords an advantage of geometrical flexibility over that of the covalent type.[3] Multiple hydrogen bonding interactions provide a general method for the protein-carbohydrate recognition, in which most water molecules are often excluded from the cleft of the protein in order to avoid their possible hydrogen-bonding competition. Thus, many artificial receptors have been designed to mimic biotic carbohydrate recognition by using hydrogen bondings in aprotic solvents.[1b] Unfortunately, the detecting method generally relies on ^{1}H NMR chemical shift changes and hence is limited in its sensitivity. To circumvent this problem, fluorescence spec-

troscopic and circular dichroic methods have been utilized as the detection tools in several examples.[4] We report here

---

* Fax for Prof. Jim-Min Fang: (8862)-2363-6359.
† National Taiwan University.
‡ Academia Sinica.
§ Current address: Department of Chemistry, Fu-Jen Catholic University, No. 510, Chung Cheng Road, Shih Chuang, Taiwan.

(1) For general reviews, see: (a) Aoyama, Y. In *Comprehensive Supramolecular Chemistry*; Atwood, J. L., Davies, J. E. D., MacNicol, D. D., Vögtle, F., Eds.; Elsevier: Oxford, 1996; Vol. 2, Chapter 9, pp 279–307. (b) Davis, A. P.; Wareham, R. S. *Angew. Chem., Int. Ed.* **1999**, *38*, 2978.

(2) (a) Kobayashi, K.; Asakawa, Y.; Kato, Y.; Aoyama, Y. *J. Am. Chem. Soc.* **1992**, *114*, 1030. (b) Bhattarai, K. M.; Bonar-Law, R. P.; Davis, A. P.; Murray, B. A. *Chem. Commun.* **1992**, 752. (c) Liu, R.; Still, W. C. *Tetrahedron Lett.* **1993**, *34*, 2573. (d) Huang, C.-Y.; Cabell, L. A.; Anslyn, E. V. *J. Am. Chem. Soc.* **1994**, *116*, 2778. (e) Das, G.; Hamilton, A. D. *J. Am. Chem. Soc.* **1994**, *116*, 11139. (f) Anderson, S.; Neidlein, U.; Gramlich, V.; Diederich, F. *Angew. Chem., Int. Ed. Engl.* **1995**, *34*, 1596. (g) Jiménez-Barbero, J.; Junquera, E.; Martín-Pastor, M.; Sharma, S.; Vicent, C.; Penadés, S. *J. Am. Chem. Soc.* **1995**, *117*, 11198. (h) Mizutani, T.; Kurahashi, K.; Murakami, T.; Matsumi, N.; Ogoshi, H. *J. Am. Chem. Soc.* **1997**, *119*, 8991. (i) Davis, A. P.; Wareham, R. S. *Angew. Chem., Int. Ed.* **1998**, *37*, 2270. (j) Inouye, M.; Takahashi, K.; Nakazumi, H. *J. Am. Chem. Soc.* **1999**, *121*, 341. (k) Mazik, M.; Sicking, W. *Chem. Eur. J.* **2001**, *7*, 664. (l) Král, V.; Rusin, O.; Schmidtchen, F. P. *Org. Lett.* **2001**, *3*, 873. (m) Bitta, J.; Kubik, S. *Org. Lett.* **2001**, *3*, 2637. (n) Benito, J. M.; Gómez-García, M.; Blanco, J. L. J.; Mellet, C. O.; Fernández, J. M. G. *J. Org. Chem.* **2001**, *66*, 1366.

(3) (a) James, T. D.; Sandanayake, K. R. A. S.; Shinkai, S. *Angew. Chem., Int. Ed. Engl.* **1996**, *35*, 1910. (b) Eggert, H.; Frederiksen, J.; Morin, C.; Norrild, J. C. *J. Org. Chem.* **1999**, *64*, 3846. (c) Kukrer, B.; Akkaya, E. U. *Tetrahedron Lett.* **1999**, *40*, 9125. (d) DiCesare, N.; Lakowicz, J. R. *Chem. Commun.* **2001**, 2022. (e) DiCesare, N.; Lakowicz, J. R. *J. Phys. Chem.* **2001**, *105*, 6834. (f) Yang, W.; He, H.; Drueckhammer, D. G. *Angew. Chem., Int. Ed.* **2001**, *40*, 1714.

a novel saccharide probe, 2,7-bis(1H-pyrrol-2-yl)ethynyl-1,8-naphthyridine (BPN, Figure 1).[5] BPN exhibits a unique
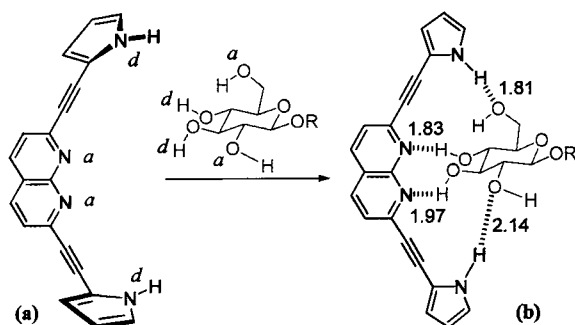

Figure 1. (a) Free BPN showing the conjugated *daad* array with two pyrrole rings slightly tilted toward opposite directions. (b) BPN and its associated BPN/β-D-glucoside hydrogen-bonding complex. The geometrically optimized complex (R = CH₃) derived by the B3LYP/6-31G** method shows the distances (Å) of the hydrogen bonds.
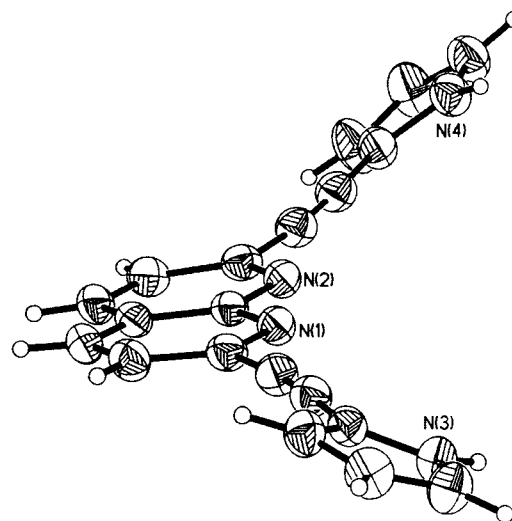
property among the hydrogen-bonding type of artificial receptors in which the conjugated *daad* array acts intrinsically as a saccharide receptor as well as a sensing chromophore. As an alternative to the extensively studied boronic acid receptors,[3] we brought noncovalent recognition and direct visual detection of carbohydrate into an integral system. The new concept evokes monosaccharide as an *adda* molecule complementary to the *daad* array of BPN to form a complex with quadruple hydrogen bondings.

Synthesis of BPN incorporated the coupling reaction of 2,7-dichloro-1,8-naphthyridine with 2 equiv of (1-*tert*-butoxycarbonyl-pyrrol-2-yl)acetylene, followed by removal of the Boc protective group (Scheme 1). Two pyrrole rings

Scheme 1. Synthetic of 2,7-Bis(1H-pyrrol-2-yl)ethynyl-1,8-naphthyridine (BPN)
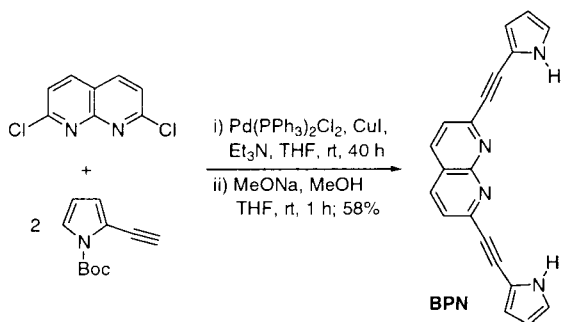
in BPN are slightly tilted toward opposite directions (X-ray analysis, Figure 2), but reorganize to a rigid inward conformation upon binding with a chairlike pyranoside (Figure 1). The pyrrole and naphthyridine moieties function as the proton donor (*d*) and acceptor (*a*), respectively, and also develop an ideal V-shaped cleft to provide as many as

Figure 2. ORTEP drawing of BPN (side view).

four hydrogen-bonding sites. Through the multiple hydrogen bonds effect the unusual push−pull *daad* relay conjugated through the ethynyl bridge induces the π-electron delocalization.[7b] Furthermore, rigidification upon formation of the BPN/pyranoside complex might also contribute a role in enhanced fluorescence, as shown in previous studies on the bindings of ions[6] and carbohydrates.[7] In combination, ultrasensitive detection can thus be achieved via the remarkable change of the electronic spectroscopy.

Upon adding octyl β-D-glucopyranoside (OGU), the 410-nm free BPN band (log ϵ ≈ 4.65) in CH₂Cl₂ solution decreased significantly along with the growth of a new absorption band at ∼435 nm (Figure 3). An isosbestic point at ∼415 nm throughout the titration was attributed to the formation of BPN/OGU hydrogen-bonding complexes in equilibrium with free BPN. The measured absorbance [A_0/($A - A_0$)] as a function of the inverse of OGU concentrations fit a linear relationship, indicating the 1:1 stoichiometry of the BPN/OGU complex.[8] On the basis of 1:1 stoichiometry of BPN/OGU, the relationship between the measured ab-

(4) (a) Kikuchi, Y.; Kobayashi, K.; Aoyama, Y. *J. Am. Chem. Soc.* 1992, *114*, 1351. (b) Inouye, M.; Miyake, T.; Furusyo, M.; Nakazumi, H. *J. Am. Chem. Soc.* 1995, *117*, 12416. (c) Mizutani, T.; Kurahashi, T.; Murakami, T.; Matsumi, N.; Ogoshi, H. *J. Am. Chem. Soc.* 1997, *119*, 8991. (d) Tamaru, S.-i.; Yamamoto, M.; Shinkai, S.; Khasanov, A. B.; Bell, T. W. *Chem. Eur. J.* 2001, *7*, 5270. (e) Tamaru, S.-i.; Shinkai, S.; Khasanov, A. B.; Bell, T. W. *Proc. Natl. Acad. Sci.* 2002, *99*, 4972.

(5) (a) Newkome, G. R.; Garbis, S. J.; Majestic, V. K.; Fronczek, F. R.; Chiari, G. *J. Org. Chem.* 1981, *46*, 833. (b) Ziessel, R.; Suffert, J.; Youinou, M.-T. *J. Org. Chem.* 1996, *61*, 6535. The carbohydrate recognition properties of some naphthyridine derivatives have been demonstrated in refs 2k, 4d, and 4e. Compounds containing pyrrole moieties have been used to bind fluoride ion. See a recent example: (c) Mizuno, T.; Wei, W.-H.; Eller, L. R.; Sessler, J. L. *J. Am. Chem. Soc.* 2002, *124*, 1134.

(6) (a) McFarland, S. A.; Finney, N. S. *J. Am. Chem. Soc.* 2001, *123*, 1260. (b) Mello, J. V.; Finney, N. S. *Angew. Chem., Int. Ed.* 2001, *40*, 1536. (c) Choi, K.; Hamilton, A. D. *Angew. Chem., Int. Ed.* 2001, *40*, 3912. (d) McFarland, S. A.; Finney, N. S. *J. Am. Chem. Soc.* 2002, *124*, 1178.

(7) (a) Sandanayaka, K. R. A. S.; Nakashima, K.; Shinkai, S. *Chem. Commun.* 1994, 1621. (b) Takeuchi, M.; Yoda, S.; Imada, T.; Shinkai, S. *Tetrahedron* 1997, *53*, 8335.
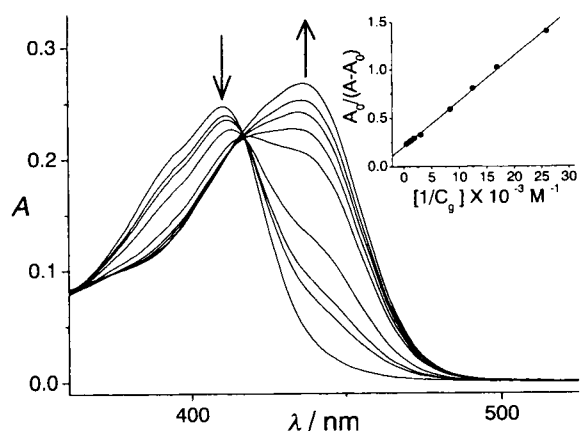
Figure 3. Absorption spectra of BPN (5.4×10^{-6} M) in CH_2Cl_2 by adding various concentrations (C_g) of octyl glucopyranoside. Insert: the plot at 435 nm shows a linear relationship of $[A_0/(A - A_0)]$ vs $1/C_g$, indicating the 1:1 stoichiometry of BPN/OGU.

Figure 4. Fluorescence spectra of BPN (1.2×10^{-5} M) in CH_2Cl_2 by adding various concentrations (C_g) of octyl glucopyranoside. The fluorescence spectra ($\lambda_{ex} = 430$ nm) show the growth of a 535-nm emission band on complexation, accompanied by decrease of the 475-nm band for uncomplexed BPN. $*$ denotes Raleigh scattering. Insert: the plot at 535 nm shows a linear relationship of $[F_0/(F - F_0)]$ vs $1/C_g$, indicating the 1:1 stoichiometry of BPN/OGU.

sorbance A as a function of the added OGU concentration, C_g, can be expressed by $A_0/(A - A_0) = [\epsilon_M/(\epsilon_C - \epsilon_M)](K_a^{-1}C_g^{-1} + 1)$ where ϵ_M and ϵ_C are molar extinction coefficients of the BPN monomer and hydrogen-bonding complex, respectively, at a selected wavelength.[8] A_0 denotes the absorbance of the free BPN at that specific wavelength. The ratio for the intercept versus slope deduced the association constant K_a of $(4.8 \pm 0.8) \times 10^3$ M^{-1}.

Dual spectral features were observed in the fluorescence titration study. The characteristic uncomplexed BPN emission band at 475 nm ($\tau_f \approx 1.25$ ns) decreased, accompanied by the growth of a 535-nm ($\tau_f \approx 0.95$ ns) emission band. The results in combination with different excitation spectra between monitoring at, e.g., 450 and 550 nm led us to conclude that dual fluorescence originates from different ground-state precursors, namely, the uncomplexed BPN and BPN/OGU complex, respectively (Figure 4). The plot of $[F_0/(F - F_0)]$ at 535 nm versus the inverse of OGU concentrations reconfirmed a 1:1 BPN/OGU complex.[8] The relationship between the measured fluorescence intensity F and C_g in a selected wavelength can be expressed by $F_0/(F - F_0) = [\Phi_M\epsilon_M/(\Phi_M\epsilon_M - \Phi_C\epsilon_C)](K_a^{-1}C_g^{-1} + 1)$, where F_0 denotes the fluorescence intensity of free BPN. Φ_M and Φ_C are fluorescence quantum yields of the free BPN and complex, respectively, and are assumed to be constant throughout the titration.[8] The ratio for the intercept versus slope gave a K_a value of $(5.5 \pm 0.5) \times 10^3$ M^{-1}, which within experimental error is consistent with the value deduced from the absorption titration.

The fluorescence yields for BPN (i.e., the 475 nm band) and the BPN/OGU complex (i.e., the 535-nm band) were measured to be as high as 0.35 ± 0.01 and 0.23 ± 0.02 in CH_2Cl_2, respectively. By selecting the excitation wavelength
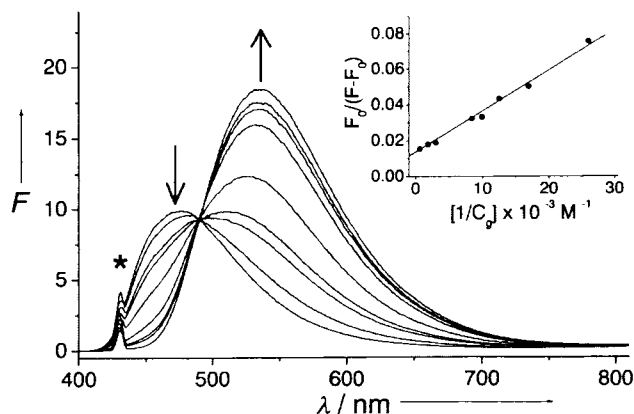
at >460 nm where the absorbance was solely attributed to the BPN/OGU complex, a detection limit as low as ~100 pM OGU could be achieved on the basis of the nearly background (i.e., the uncomplexed BPN)-free 535-nm emission. The ratiometric fluorescence proved to be a reliable and ultrasensitive method for the real time detection of BPN/OGU complexation.

The 1:1 BPN/OGU complexation was further supported by the NMR study using a continuous variation method (Job plot),[9] in which the chemical shift changes of pyrrol-NH as a function of sugar concentrations were monitored. The temperature-dependent (285−315 K) ^{1}H NMR study indicated that the formation of the BPN/OGU complex was thermodynamically favored ($\Delta G_{300} = -5.79$ kcal/mol), in agreement with the proposed quadruple hydrogen bond formation. The association constants and thermodynamic parameters are collected in Table 1. A molecular modeling of BPN/methyl β-D-glucoside complex (Figure 1b) implied

Table 1. Association Constants and Thermodynamic Parameters for the Complexes of BPN with Octyl Glucoside (OGU), Octyl Galactoside (OGA), and Octyl Furanoside (OFU)

complex	K_a (M^{-1})	ΔH_{300} (kcal/mol)	ΔS_{300} (cal/mol)	ΔG_{300} (kcal/mol)
BPN/OGU	5000^a $(20000)^b$	-12.3^c	-21.8^c	-5.79^c
BPN/OGA	1600^a $(6200)^b$			-5.21^d
BPN/OFU	190^a $(490)^b$			-3.69^d

[a] The association constant was derived from the absorption and fluorescence titrations in CH_2Cl_2 solution. Estimated errors are within ±20%. [b] The association constant was derived from the ^{1}N MR titrations in $CDCl_3$ solution. [c] The thermodynamic data were deduced from the temperature-dependent ^{1}H NMR studies. $\Delta G = \Delta H - T\Delta S$. [d] The value was derived from $\Delta G = -RT \ln K_a$ (in $CDCl_3$ solution).

(8) Chou, P. T.; Wu, G. R.; Wei, C. Y.; Cheng, C. C.; Chang, C. P.; Hung, F. T. *J. Phys. Chem. B* **2000**, *104*, 7818. A_0, F_0, A, and F denote, respectively, the absorbance and fluorescent intensity of free BPN and in solution after adding monosaccharides at a selective wavelength.

the importance of multiple hydrogen bond formation as well as the geometrical fitness to accommodate each hydrogen bond. All calculated OH···N and NH···O distances are significantly shorter than the sum of van der Waals radii of H and N (2.7 Å) and H and O (2.6 Å).

The intrinsic conjugated *daad* type chromophore[2d,j,k,10] in BPN is of key importance to account for the remarkable spectral differences. The acidity of pyrrole and basicity of naphthyridine could be enhanced at the excited state through the conjugated dual hydrogen-bonding effect.[8] The complexation with saccharide thus provides multiple hydrogen bond induced charge transfer to account for a drastic alternation on the fluorescent property. To support this viewpoint, a nonconjugated *daad* molecule of 2,7-bis(3-hydroxy-3-methylbutynyl)-1,8-naphthyridine (BHN) was prepared (Figure 5). Upon forming the BHN/OGU complex (K_a
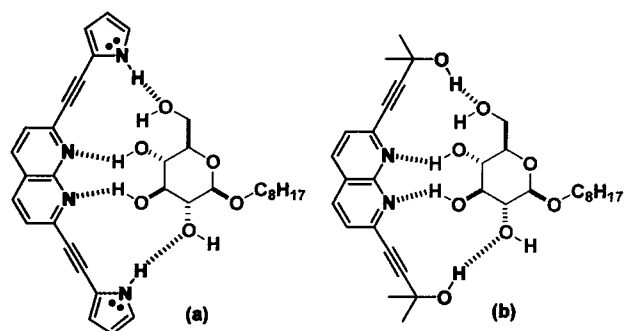
Figure 5. (a) A large Stoke shift (60 nm) in the fluorescence spectrum of BPN/OGU complex is attributed to the multiple hydrogen bond induced charge transfer. (b) Complexation of BHN with OGU does not show significant spectral shift because BHN lacks a continuous push−pull π-system to account for charge transfer.

≈ 1000 M^{-1} measured by ^{1}H NMR in CDCl$_3$) the fluorescence intensity (λ_{max} 387 nm) did increase, albeit no significant spectral shift was observed in either absorption

or fluorescence spectra. The enhanced fluorescence could be rationalized by the conformational rigidification, whereas the lack of a continuous push−pull π-system prohibits the multiple hydrogen bond induced charge-transfer effect.

The preferable 1:1 complexation of BPN with octyl β-D-galactopyranoside (OGA) or octyl β-L-fucopyranoside (OFU) was similarly determined by absorption, fluorescence, and ^{1}H NMR titrations (see Table 1 and Supporting Information). While the only structural difference between OGA and OGU is the spatial orientation of 4-OH, the association constant for OGA is smaller than that of OGU by ca. 3-fold. This binding selectivity of BPN/OGU over BPN/OGA is comparable or superior to those reported in the literature.[2,4e] For OFU in which one hydrogen bond is eliminated by modifying the C(6)CH$_2$OH to CH$_3$ group, K_a decreases by a factor of ∼35 in comparison with that of the BPN/OGU complex.

In summary, our results demonstrate the selective affinity and ultrasensitivity for probing the BPN/OGU complex. Visual change of free BPN (cyanic color) in CH$_2$Cl$_2$ (1.2 × 10^{-5} M) to green color upon addition of octyl glucopyranoside (5.2 × 10^{-4} M) was obvious (see Abstract graphic). Since the synthesis of BPN was straightforward, chemical modification including the preparation of water-soluble derivatives would be feasible. We are currently engaged in the research of such aspects in order to develop practical carbohydrate sensors.

Supporting Information Available: Detailed experimental procedures, absorption, fluorescence, and ^{1}H NMR spectra, molecular calculations, and X-ray diffraction data. This material is available free of charge via the Internet at http://pubs.acs.org.

(9) Connors, K. A. *Binding Constants*; Wiley: New York, 1987.

(10) (a) Bell, T. W.; Beckles, D. L.; Cragg, P. J.; Liu, J.; Maioriello, J.; Papoulis, A. T.; Santora, V. J. In *Fluorescent Chemosensors for Ion and Molecular Recognition*; Czarnik, A. W., Ed.; American Chemical Society: Washington, DC, 1993; Chapter 7, pp 85−103. (b) Bell, Z. T.; Hou, W.; Luo, Y.; Drew, M. G. B.; Chapoteau, E.; Czech, B. P.; Kumar, A. *Science* **1995**, *269*, 671. (c) Lüning, U.; Kühl, C. *Tetrahedron Lett.* **1998**, *39*, 5735. (d) Corbin, P. S.; Zimmerman, S. C. *J. Am. Chem. Soc.* **2000**, *122*, 3779.

Syntheses and spectroscopic studies of spirobifluorene-bridged bipolar systems; photoinduced electron transfer reactions†

Yuh-Yih Chien, Ken-Tsung Wong,* Pi-Tai Chou* and Yi-Ming Cheng

*Department of Chemistry, National Taiwan University, 106 Taipei, Taiwan, ROC.
E-mail: kenwong@ccms.ntu.edu.tw, chop@ccms.ntu.edu.tw; Fax: +886 2-2363-6359; Tel: +886 2-2363-0231 ext. 3315*

Some 9,9′-spirobifluorene-bridged bipolar systems 1–3 containing 1,3,4-oxadiazole-conjugated oligoaryl and triarylamine moieties have been synthesized, in which 1 exhibits remarkable solvent-polarity dependent fluorescence properties due to a highly efficient photoinduced electron transfer reaction.

Bipolar (*i.e.* dual chromophores) organic materials have received considerable attention due to their potential uses in molecular devices such as molecular rectifiers,[1] switches,[2] electrochemical sensors,[3] photovoltaic cells,[4] and nonlinear optical materials,[5a] etc. It has been a central interest to integrate such composite materials (or devices) *via* the modification of chromophores and linker structures so that the physical properties can be fine-tuned to a designated function. Recently, syntheses of materials aimed at increasing the dimensionality have been explored, among which the three-dimensional design based on spiro-bridged conjugated systems is of particular interest.[5] In this communication, we report the synthesis and photophysical studies of another new type of 9,9′-spirobifluorene-bridged bipolar system. In this bipolar molecule, the 1,3,4-oxadiazole-containing conjugated oligoaryl system, serves as the electron acceptor, while the triarylamine moiety acts as the donor counterpart. Such a configuration may conceptually lead to the development of new materials with an interfacial layer of bifunctional properties.

The synthetic pathways of 9,9′-spirobifluorene-bridged bipolar molecule 1 and model compounds 2 and 3 are shown in Scheme 1. Treatment of 2,7-dibromo-9,9′-spirobifluorene with CuCN in DMF at the reflux temperature gave the dicyano derivative 4 in a 90% yield. The unsubstituted branch of the 9,9′-spirobifluorene was then regioselectively brominated at C-2′ and C-7′ positions with Br₂ solution (in CH₂Cl₂) in the presence of Lewis acid, AlCl₃, which was used as a promoter. The dibrominated crude product was directly subjected to a Pd-catalysed amination with diphenylamine in the presence of a catalytic amount of P*Bu₃ to give an 80% yield of 5. The cyano groups in 5 were further converted to tetrazoles by treatment with NaN₃ and NH₄Cl in DMF at reflux temperature to form bis-tetrazole 6 in an 80% yield. Subsequently, treating 6 with 4-*tert*-butylbenzoyl chloride in pyridine leads to the formation of the final spiro-configured bipolar compound 1 in a 73% yield. In addition to the elemental analysis of 1, which assigned the designated structural composition, the structure of 1 was further confirmed by single crystal X-ray diffraction analysis.[6] For comparison, two model compounds, 2 and 3 were synthesized from 2,7-dibromo-9,9′-spirobifluorene *via* a similar synthetic pathway. Compounds 1–3 sublime at a relatively low temperature, providing the feasibility in their integration into molecular devices.

As shown in Fig. 1 the absorption spectral features of 1 in THF exhibit a composite characteristic of 2and 3. Careful spectral analyses indicate that the absorption extinction coefficients, ε(λ), within experimental error, are identical with those of 2 plus 3 (see Fig. 1). Thus, the merging of 2 and 3 into bipolar

molecule 1 causes negligible interactions among chromophores in the electronic ground state. In contrast, the incorporation of chromophores provokes strong interactions in the excited state. Fluorescence maxima at 392 and 373 nm were observed for 2 and 3 in THF (see Fig. 1), of which the Stokes shift was calculated to be as small as ~ 670 and 365 cm^{-1}, respectively. Similar normal Stokes shifted fluorescence was observed for 2
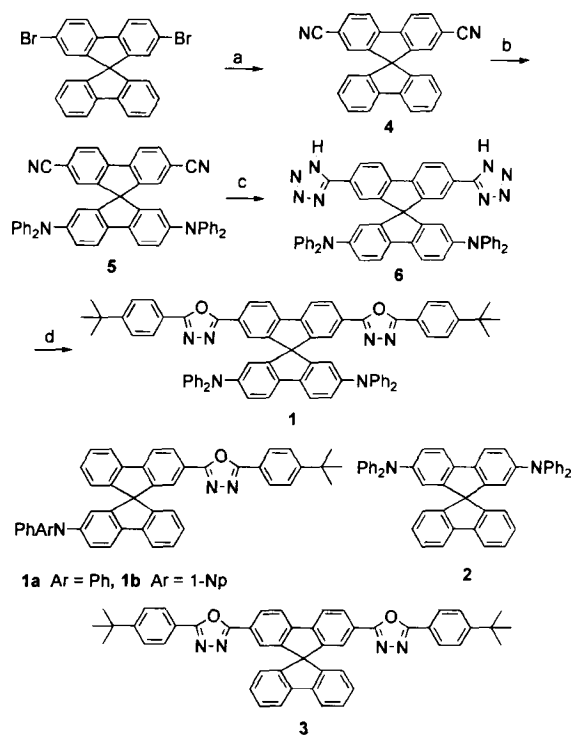
Scheme 1 *Reagents and condition*: a, CuCN, DMF, reflux; b, i, Br₂, AlCl₃, CH₂Cl₂, reflux; ii, Ph₂NH, Pd(OAc)₂, PtBu₃, NaOtBu, PhCH₃, reflux; c, NaN₃, NH₄Cl, DMF, reflux; d, 4-ᵗBuPhCOCl, pyridine, reflux.

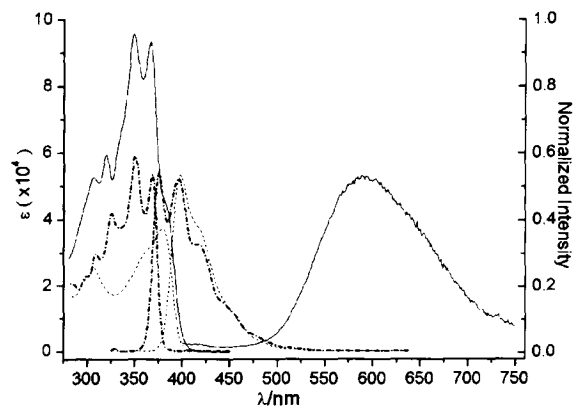**Fig. 1** Absorption and emission spectra of 1 (—), 2 (-----) and 3 (—·—·—) in THF. The emission intensities for 1–3 have been normalized for clarity.

and **3** in other studied solvents. Conversely, **1** in THF exhibited exclusively a new emission band maximized at ~590 nm (a Stokes shift of ~9000 cm^{-1}), while the normal emission attributed to **2** or **3** individually was too weak to be resolved. The excitation spectrum is effectively identical to the absorption profile, excluding its origin from traces of impurity. Detailed analyses revealed that the intensity of the 590-nm emission was linearly proportional to the studied concentrations in the range of 10^{-5}–10^{-4} mol dm^{-3}. Thus, the possibility of the emission resulting from the aggregation effect can also be eliminated. Alternatively, the results can be more plausibly rationalized by a mechanism incorporating a photoinduced electron transfer (ET) process. This viewpoint can first of all be supported by the strong solvent-dependent spectral properties shown in Fig. 2. The spectral shift of the fluorescence upon increasing solvent polarity (Δf) depends on the difference in permanent dipole moments between ground and excited states, which can be quantitatively expressed as:

$$\tilde{v}_f = \tilde{v}_f^{vac} - (2|\vec{\mu}_e - \vec{\mu}_g|^2/hca_0^3)\Delta f \qquad (1)^7$$

As shown in the inset of Fig. 2, the plot of $\tilde{v}_f$ versus Δf is sufficiently linear, in which the large slope of 14 200 cm^{-1} is obtained, supporting the proposed electron-transfer mechanism in the excited state. As a result, a charge transfer (CT) emission band was observed in **1**. Secondly, the free-energy change (ΔG) for photoinduced electron transfer between an excited donor molecule (D*) and a ground-state acceptor (A) at a distance (d) can be expressed as:

$$\Delta G = E_{ox}(D) - E_{red}(A) - E_{00}(D) - (e^2/\varepsilon d)$$
$$- (e^2/2)(1/r_D^+ + 1/r_A^-)(1/\varepsilon_r - 1/\varepsilon) \qquad (2)$$

where $E_{ox}(D)$ and $E_{red}(A)$ are the oxidation and reduction potentials of triarylamine and 1,3,4-oxadiazole moieties, respectively, $E_{00}(D)$ is the energy of zero–zero transition, r_D^+ and r_A^- are effective ionic radii, ε is the dielectric constant of solvent, and d is the center-to-center distance between D and A. E_{ox} and E_{red} for **1**, measured by cyclic voltammetry experiments (see ESI†), were measured to be 0.88 and −1.69 V, respectively in THF. E_{00} of 3.25 eV (~382 nm) was obtained from the first vibronic peak of the UV spectrum. According to the X-ray structure, the center-to-center distance between D and A of **1** was estimated to be ~7.7 Å. A semi-empirical PM3 approximation was further made on r_D^+ ~ r_A^- = 5.3 Å. With all values substituted into eqn. (2), the free energies of ET (ΔG) were calculated and shown in Table 1. As indicated by the ΔG values of < −0.63 eV, the excited state ET reaction is apparently an exergonic process in all solvents applied. This viewpoint can be further supported by the corresponding ET dynamics for **1** in various solvents. The fluorescence rise and decay dynamics were measured by a time-correlated photon counting system, rendering a temporal resolution of ~15 ps (see ESI†). The results listed in Table 1 clearly showed that except for the well-
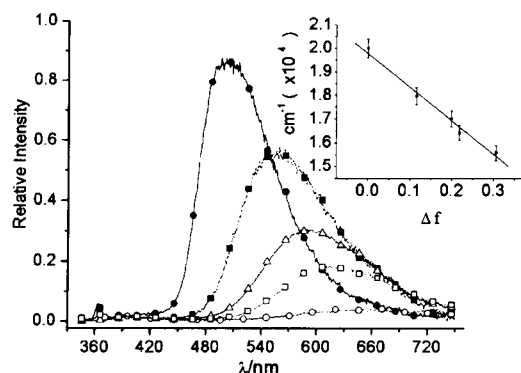

Fig. 2 The emission spectra of **1** in cyclohexane (●), benzene (■), tetrahydrofuran (△), dichloromethane (□) and acetonitrile (○). The optical density at the excitation wavelength (330 nm) was prepared to be 0.2 in all studied solvents. Inset: the plot of emission peak frequencies as a function of solvent polarities.

Table 1 Photophysical properties of **1–3** in various solvents

	Solvent	λ_{max}/nm^a	PL λ_{max}/ nm	Φ	τ/ns^b	ΔG^c
1	CYC	382	500	4.49 × 10^{-2}	18.25	−0.63
	BEN	384	557	3.57 × 10^{-2}	42.09	−0.68
	THF	382	588	1.08 × 10^{-2}	37.77	−0.94
	DCM	383	609	5.20 × 10^{-3}	20.66	−0.96
	ACN	378	642	1.08 × 10^{-3}	6.45	−1.03
2	THF	382	392	0.58	1.05	
3	THF	368	373	~1.0	0.91	

^{a} Absorption, data was taken from the first vibronic peak. ^{b} Samples for the lifetime measurements were degassed via three freeze–pump–thaw cycles. ^{c} Free energies (ΔG) of the electron transfer for **1** in various solvents were calculated according to eqn. (2). See text for the detailed description.

fitted single exponential decay, the rise dynamics of the emission for **1** was irresolvable (≪15 ps), indicating the occurrence of a fast ET process.

Attempts have also been made by synthesizing two analogues **1a** and **1b** (Scheme 1, see ESI†), in which the molecular symmetry is lowered by bearing only a pair of D(triarylamine)/ A(1,3,4-oxadizaole) chromophore rather than two D/A pairs in **1**. Our preliminary results revealed a similar highly efficient ET process, resulting in an anomalous CT band (not shown here). Thus, under a decent driving force (ΔG) the ET process can be generalized among the spirobifluorene-conjugated D/A systems.

Assuming an ET efficiency of approximately unity, the solvent-polarity dependent yields ranging from 10^{-3} to 0.05 for **1** (see Table 1) are relatively smaller than those of parent molecules **2** and **3** (Table 1). This can be rationalized by the facts that back electron transfer is considered a forbidden process and is normally dominated by the radiationless deactivation. In addition, as the local excitation (LE)-ET zero-order gap increases by increasing the solvent polarity, the radiative decay rate of the ET band decreases due to the reduction in LE/ET interaction.[8] The combination of these two factors rationalizes the decrease of the emission yield as the solvent polarity increases.

Theoretically, it is feasible to adjust the D/A strength as well as the number of spirobifluorene conjugation so that the flow of electrons can be precisely regulated. Such a conceptual design may be advantageously exploited in e.g. photovoltaic devices. To achieve this goal, focus on poly-spirobifluorene conjugated bipolar or triad systems is currently in progress.

Notes and references

1 R. M. Metzger, J. Mater. Chem., 2000, **10**, 55.
2 A. P. de Silva, H. Q. N. Gunaratne, T. Gunnlaugsson, A. J. M. Huxley, C. P. McCoy, J. T. Rademacher and T. E. Rice, Chem. Rev., 1997, **97**, 1515.
3 F. D. Lewis, T. Wu, Y. Zhang, R. L. Letsinger, S. R. Greenfield and M. R. Wasielewski, Science, 1997, **277**, 673.
4 D. Gust, T. A. Moore and A. L. Moore, Acc. Chem. Res., 1993, **26**, 198.
5 (a) S. Y. Kim, M. Lee and B. H. Boo, J. Chem. Phys., 1998, **109**, 2593; (b) P. Malask, Adv. Mater., 1994, **6**, 405.
6 Crystal data for **1**: C$_{78.50}$H$_{70}$Cl$_5$N$_6$O$_2$, M = 1306.66, monoclinic, space group $P2_1/n$, a = 13.7737(1), b = 27.0557(3), c = 20.0245(2) Å, β = 105.0516(4)°, U = 7206.26(12) Å^3, Z = 4, D c = 1.204 Mg m^{-3}, μ = 0.251 mm^{-1}, $F(000)$ = 2736, T = 150 K, wavelength 0.71073 Å, crystal size 0.25 × 0.22 × 0.15 mm, θ_{max} 25.00°, 41176 reflections measured, final R [$I > 2\sigma(I)$] = 0.1091, CCDC 192594. See http://www.rsc.org/suppdata/cc/b2/b208269a/ for electronic files in CIF or other electronic format.
7 $\tilde{v}_f$ and $\tilde{v}_f^{vac}$ in eqn. (1) are the spectral position of the solvation equilibrated fluorescence maxima and the value extrapolated to the diluted gas-phase, respectively, a_0 denotes the radius of solute, $\vec{\mu}_g$ and $\vec{\mu}_e$ are the dipole moment vectors of the ground and excited states, and Δf is the Lippert solvent polarity parameter expressed as $\Delta f = (\varepsilon - 1)/(2\varepsilon + 1) - (n^2 - 1)/(2n^2 + 1)$.
8 T. J. Kang, M. A. Kahlow, M. D. Giser, S. Swallen, V. Nagarajan, W. Jarzeba and P. F. Barbara, J. Phys. Chem., 1988, **92**, 6800.

Photoinduced electron transfer reactions across rigid linear spacer groups of high symmetry

Kew-Yu Chen,[b] Tahsin J. Chow,[a,]* Pi-Tai Chou,[b,]* Yi-Ming Cheng[b] and Sheng-Heng Tsai[a]

[a]*Institute of Chemistry, Academia Sinica, 115 Taipei, Taiwan, ROC*
[b]*Department of Chemistry, National Taiwan University, 106 Taipei, Taiwan, ROC*

Abstract—A series of highly symmetrical dienes 1–3 were prepared through [2+2] cyclo-addition of norbornadiene (NBD) in an *exo–trans–exo* geometry. These molecules can be utilized as spacer groups in donor(D)–spacer(S)–acceptor(A) types of electronic dyads possessing strictly linear rigidity. The electronic coupling between D and A was promoted effectively by the σ-bonds through the all-*trans* spacer groups so that a highly efficient photoinduced electron transfer process takes place. The even–odd NBD dependent alternation of the D/A orientation is intriguing, which leads to an unusual correlation in the spacer tuning electron transfer process. © 2002 Elsevier Science Ltd. All rights reserved.

Long range intramolecular electron transfer (ET) reaction has been the subject of intensive study for its direct relationship with the redox processes in photosynthesis and certain biological systems.[1,2] In recent years, electron donor (D)–acceptor (A) chromophores linked by rigid, covalent spacers (S), forming D–S–A dyads, have attracted considerable attention due to their potential applications in the design of molecular devices, among which are molecular rectifiers,[3] switches,[4] electrochemical sensors,[5] photovoltaic cells,[6] and nonlinear optical materials,[7] etc. Spacer groups that have been utilized are versatile, including small molecules, e.g. cyclohexane,[8] adamantane,[2] bicyclo[2.2.2]octane,[9] steroids,[10] and oligomers of various sizes, e.g. polynorbornanes,[11] and ladderanes,[12] etc. Among numerous types of spacers, rigid linear rod-shaped structures, however, are not commonly observed.[13,14] The highly symmetrical structures reduce the complexity which is due to geometrical and conformational variations. In this study, we report the preparation of a series of linear, rigid, rod-shaped molecules based on an *exo–trans–exo* configuration of norbornanes. Both D and A groups are then attached onto the terminals of these bridging molecules with a fixed linear conformation. Preliminary spectroscopic and dynamic studies on ET processes have been performed in various solvents. The intriguing 'all-*trans* rule' as well as a D/A orientation governed ET process are reported herein.

Dimerization and trimerization of norbornadiene (NBD) were accomplished though a prototypical $Co_2(CO)_6(PPh_3)_2$ catalyzed reaction.[15] Compounds **1** and **2** were then purified by column chromatography (eluent: *n*-hexane), followed by recrystallization in hexanes and distillation under reduced pressure. Syntheses of **3** using $Ni(cod)_2$ as a catalyst have been reported with a yield as low as 3%. Alternatively, **3** was prepared via dimerization of **1** upon UV photolysis in the presence of cuprous triflate,[16] increasing the yield to ~30%. Compounds **1**, **2** and **3** represent the first three members of NBD oligomers sharing the same characteristic of all NBD units being connected by an *exo–trans–exo* geometry. For the application as spacers, the length of the structure can be finely tuned via adding different numbers of NBD units so that upon the elongation of molecular sizes, the geometry maintains linearity with two terminal double bonds being parallel and equivalent in symmetry. Electron donor and acceptor groups were then added to molecules **1–3** to form the respective dyads. A naphthalene moiety was fused onto the double bond by placing **1** through a reaction with tetrabromo-*o*-xylene according to a known procedure.[17] Compound **4** obtained was then subjected to another [2+2] cycloaddition with dimethyl acetylenedicarboxylate (DMAD), catalyzed by $RuH_2(CO)(PhPh_3)_3$, to give **5** in 85% yield.[18] The same reaction sequence was applied onto **2**, while **6** and **7** were prepared subsequently.
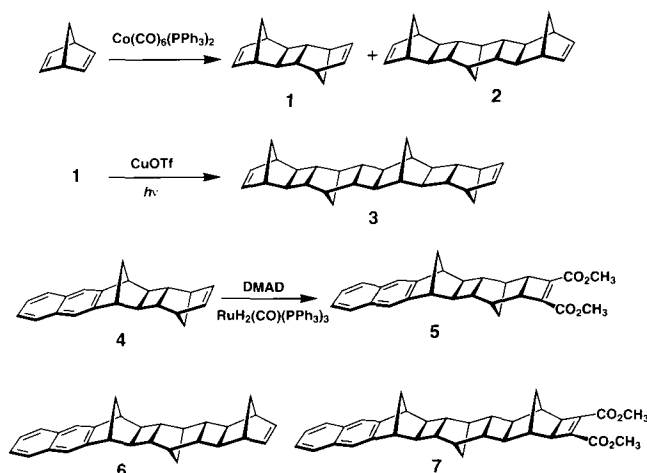
The absorption spectra of 4–7 exhibit a typical characteristic of the naphthalene chromophore. The two absorption bands at 250–290 and 300–330 nm with vibronic progressions are ascribed to ^1L_a and ^1L_b transitions, respectively, of the naphthalene moiety (Fig. 1). The absorption of 1,2-dimethoxycarbonylethyl moiety exhibits an onset at ~260 nm, which should cause negligible interference upon >266 nm excitation. As shown in Fig. 1, in comparison to 6, the naphthalene-like fluorescence (λ_{max} ~335 nm) in THF was substantially reduced in 7 where a D A pair is incorporated, indicating that the ET process is operative in the excited state. Further evidence is given by the resolution of a charge transfer (CT) band for 7 maximized at ~500 nm in THF. The peak frequency of the CT band shows strong solvent-polarity dependence (see insert of Fig. 1), being red shifted by ~1800 cm^{-1} from THF to CH_2Cl_2.

The excited-state relaxation dynamics were measured by a time-correlated photon counting system described previously,[19] rendering a temporal resolution of ~15 ps. The dynamics of decay (or rise) of 5 and 7 for both

normal (F_1) and CT (F_2) bands are listed in Table 1. As shown in Fig. 2 and Table 1, the lifetime of the F_1 band, within experimental error, correlates well with the rise time of the F_2 band, unambiguously supporting the photoinduced ET process. Table 1 also lists kinetic data for the corresponding non-ET-transfer models 4 and 6. The rate of ET, k_{ET}, can thus be calculated by the equation $k_{ET} = 1/\tau(D A) - 1/\tau(D)$ where $\tau(D A)$ and $\tau(D)$ denote the lifetime of the F_1 (normal) band for molecules possessing D/A and D functional groups, respectively. Alternatively, the ET rate constant can be accessed by a Stern–Volmer equation expressed as $k'_{ET} = \{[\Phi_f(D)/\Phi_f(D A)] - 1\}(1/\tau(D))$ where Φ_f is the fluorescence yield of the F_1 band. The results listed in Table 1 for k_{ET} are k'_{ET} show the same trend: an increase in the ET rate upon increasing the solvent polarity. The systematically smaller k'_{ET} values probably result from traces of naphthalene precursors existing in the D A dyads. Due to the very weak F_1 intensity in the studied D A dyads, any emission caused by traces of the precursor impurity may interfere with steady-state analyses.

In comparison to previously reported NBD systems, two intriguing remarks can be pointed out. Firstly, the increase in the ET rate was generally observed in these exo–trans–exo systems. The free-energy change (ΔG) for photo-induced ET between an excited donor molecule (D*) and a ground-state acceptor (A) at a distance (d) can be expressed as:

$$\Delta G(d) = E_{ox}(D) - E_{red}(A) - E_{00}(D) - (e^2/\varepsilon d) - (e^2/2)(1/r_D^+$$
$$+ 1/r_A^-)(1/37 - 1/\varepsilon) \tag{1}$$

where $E_{ox}(D)$ and $E_{red}(A)$ are the oxidation and reduction potentials of D and A molecules in acetonitrile, respectively, $E_{00}(D)$ is the energy of zero–zero transition, r_D^+ and r_A^- are effective ionic radii, ε is the dielectric constant of solvent, and d is the center-to-center distance between D and A. For example, E_{ox} and E_{red} for 6 and 7 were measured to be 1.60 and −1.50 V,
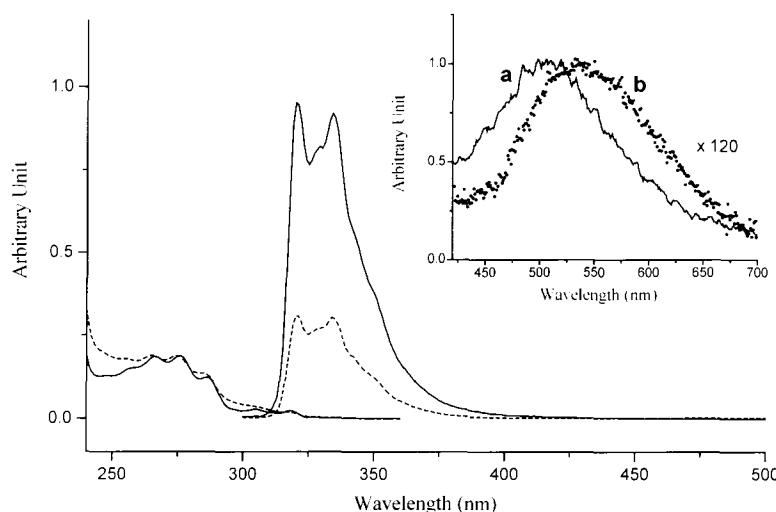
Figure 1. The absorption and emission spectra of compounds 6 (—) and 7 (----) in THF. The absorption spectra are normalized at ~290 nm, whereas the emission spectra are shown in proportion to their relative intensities. Insert: the appearance of a weak CT fluorescence in (a) THF, and (b) CH_2Cl_2.

Table 1. The relaxation dynamics of the fluorescence[a], k_{ET}, k'_{ET} and free energies (ΔG) of the ET reaction for 4–7 in various solvents

|	$\tau(4)$ (ns)	$\tau(5)$ (ns)	$\Delta G(5)$ (eV)	k_{ET} (s^{-1})[c]	$\tau(6)$ (ns)	$\tau(7)$ (ns)	k_{ET} (k'_{ET}) (s^{-1})	$\Delta G(7)$ (eV)	$\Delta G(8)$[d] (eV)
Et₂O	40.83	F₁: 0.18	−0.11	5.53 × 10⁹	56.5	F₁: 13.94	5.41 (1.86) × 10⁷	−0.07	−0.24
		F₂: 0.14 (rise) 3.78				F₂: 12.2 (rise) 13.2			
EtOAc	60.55	F₁: 0.12	−0.27	8.32 × 10⁹	51.16	F₁: 8.32	10.08 (4.34) × 10⁷	−0.23	−0.38
		F₂: 0.15 (rise) 3.28				F₂: 7.31 (rise) 9.78			
THF	57.88	F₁: 0.10	−0.34	9.98 × 10⁹	57.07	F₁: 6.78	13.01 (8.41) × 10⁷	−0.30	−0.45
		F₂: 0.09 (rise) 3.04				F₂: 6.31 (rise) 9.66			
CH₂Cl₂	36.83	F₁: 0.085	−0.39	1.2 × 10¹⁰	48.10	F₁: 2.25	42.5 (31.3) × 10⁷	−0.35	−0.50
		F₂: 2.31[b]				F₂: 1.95 (rise) 3.73			

The free energy of ET in compound **8** ($\Delta G(8)$) is listed for comparison

[a] All measurements were performed in the degassed solution.
[b] Rise dynamics could not be resolved due to the weak signal.
[c] k'_{ET} is not available due to the presence of traces of naphthalene precursor.
[d] Data from Ref. 21.
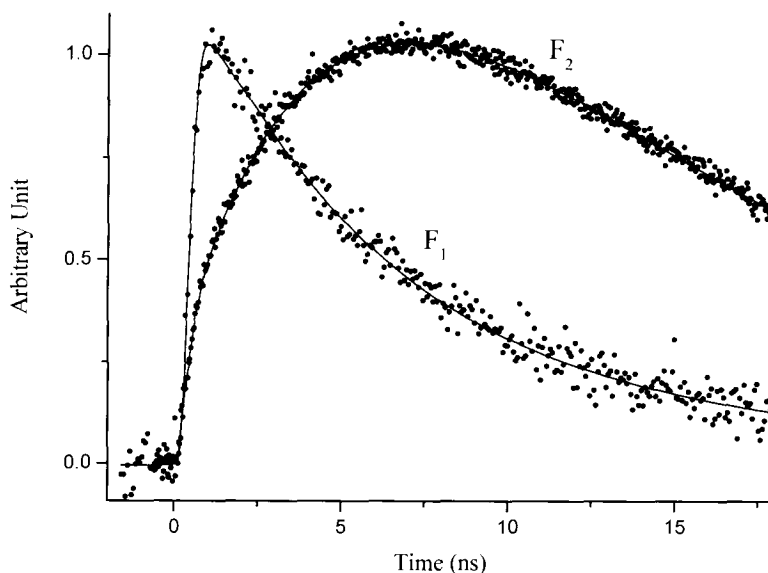
Figure 2. The time-dependent fluorescence of F_1 and F_2 bands for **7** in THF ($\lambda_{ex} = 266$ nm). For F_1: $\tau = 6.8$ ns, F_2: $\tau(\text{rise}) = 6.31$ ns, $\tau(\text{decay}) = 9.66$ ns.

respectively in CH₃CN. E_{00} was obtained from the absorption edge of UV spectrum at 318 nm (3.91 eV). An approximation was further made on $r = r_D^+ = r_A^- = 4.5$ Å.[20] Consequently, the center-to-center distance between D (midpoint of the central bond of naphthalene) and A (midpoint of the line connecting the carbonyl carbons) of **7** was estimated to be 14.7 Å. With all of the values substituted into Eq. (1), the free energies of ET (ΔG) for **7** (or **5**) were calculated and shown in Table 1.

The kinetic data were compared with an analogous system published previously. The structure of **8** is similar to that of **7**, yet with only eight σ-bonds intervening between the D and A chromophores. In THF, the rate of ET measured for **7** was about twice as fast as those reported for **8** (6.5×10⁷ s⁻¹),[21] albeit a more endergonic reaction was expected for **7** (see Table 1 for comparison), and the D–A distance of **7** (14.7 Å)[22] is even longer than that of **8** (11.4 Å due to a bent shape). Although differences in the inner shell nuclear motion

cannot be neglected, the results may implicate the differentiation in the through σ-bond overlap, and hence the differences in the electron coupling matrix, between 7 and 8. It is well known that electron tunneling can be effectively accelerated through coupling with the σ-bonds of the spacer group. The highly symmetrical geometry of 1–3 fits the 'all-*trans* rule' in a nearly perfect fashion, which may account for the higher efficiency of ET appearing in 7.[23] This phenomenon was not unprecedented though, since a recent report showed that photo-induced ET in 10 proceeded with five orders of magnitude faster than that predicted for 9.[24] With the same number of intervening σ-bonds (10 for each), the little variation in the geometries of 9 and 10 can result in an enormous difference in the rates of ET processes.

8

9

10
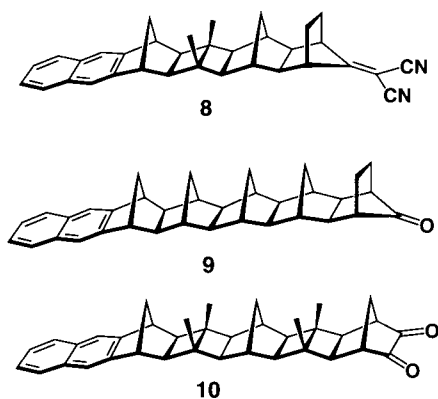
In another approach, it is interesting to note that under the same solvent polarity, e.g. in THF, the ET rate ($\sim 1.0 \times 10^{10}$ s^{-1}) in 5 is ca. two orders of magnitude as fast as that in 7 (1.3×10^8 s^{-1}). Empirically, the electron coupling matrix H_{el} can be estimated by $H_{el} = H_{el}^0 \exp[-\beta(d_{cc}-d_0)]^{25}$ where β is a measure of the ability of orbitals to extend into space and interact with another orbital, d_{cc} and d_0, denote the actual center-to-center separation distance and van der Waals distance or separation distance within the encounter complex, respectively. For D/A dyads with the same configuration of the NBD bridge, the addition of one more NBD distance generally leads to an increment of ca. one order in the rate of the ET reaction published by Paddon-Row and co-workers.[26] Certainly, an NBD unit (2-σ-bonds) in Paddon-Row's is different from an 'NBD' unit (3-σ-bonds) in the series studied here due to the way NBD is fused. Nevertheless, except for the distance of separation, there are also other parameters that might affect the interaction between two chromophores. Spin changes, symmetry factors, and the relative orientation of two reactants may influence the magnitude of H_{el}. For the *exo–trans–exo* system reported in this study, depending on even or odd number of the NBD unit, the orientation between D and A is expected to switch alternatively between 0 and $\sim 60°$. Accordingly, it is plausible that the unusually large difference in the ET rate, in part, may result from the relative difference in the D/A orientation between 5 and 7. However, since derivation of H_{el} depends sensibly on the shape, nodal character, and mutual orientation of

the orbitals and is even more complicated in the excited state, detailed calculations were not performed in this preliminary study.

In conclusion, a series of highly symmetrical dienes 1–3 were prepared through [2+2] cyclo-addition of NBD in *exo–trans–exo* geometry. These molecules can be utilized as spacer groups in the D–S–A type of electronic dyads possessing a strictly linear rigidity. The electronic coupling between D and A was promoted effectively by the σ-bonds through the all-*trans* spacer groups so that a highly efficient photoinduced ET process takes place. The linearity of the dyads should also be a key-contributing factor to the ET efficiency in comparison to previously reported bent structures. This, in combination with the even–odd NBD dependent alternation of the D/A orientation, initiates a perspective aiming at elongating the *exo–trans–exo* system so that a detailed insight of the ET dynamics can be examined. Design and syntheses toward this goal are currently in progress.

Acknowledgements

References

1. (a) Speiser, S. *Chem. Rev.* 1996, 96, 1953 and references cited therein; (b) Wasielewski, M. *Chem. Rev.* 1992, 92, 435.

2. Balzani, V.; Juris, A.; Venturi, M. *Chem. Rev.* 1996, 96, 759.

3. (a) Metzger, R. M. *J. Mater. Chem.* 2000, 10, 55; (b) Scheib, S.; Cava, M. P.; Baldwin, J. W.; Metzger, R. M. *J. Org. Chem.* 1998, 63, 1198; (c) Aviram, A.; Ratner, M. A. *Chem. Phys. Lett.* 1974, 29, 277.

4. (a) Chen, J.; Reed, M. A.; Rawlett, A. M.; Tour, J. M. *Science* 1999, 286, 1550; (b) de Silva, A. P.; Gunaratne, H. Q. N.; Gunnlaugsson, T.; Huxley, A. J. M.; McCoy, C. P.; Rademacher, J. T.; Rice, T. E. *Chem. Rev.* 1997, 97, 1515.

5. (a) Yu, C. J.; Chong, Y.; Kayyem, J. F.; Gozin, M. *J. Org. Chem.* 1999, 64, 2070; (b) Lewis, F. D.; Wu, T.; Zhang, Y.; Letsinger, R. L.; Greenfield, S. R.; Wasielewski, M. R. *Science* 1997, 277, 673.

6. (a) Gust, D.; Moore, T. A.; Moore, A. L. *Acc. Chem. Res.* 1992, 26, 198; (b) Roest, M. R.; Verhoeven, J. W.; Schuddeboom, W.; Warman, J. M.; Lawson, J. M.; Paddon-Row, M. N. *J. Am. Chem. Soc.* 1996, 118, 1762.

7. (a) Boyd, R. W. *Nonlinear Optics*; Academic: New York, 1992; (b) Prasad, P. N.; Williams, D. J. *Introduction to Nonlinear Optical Effects in Molecular and Polymers*; Wiley: New York, 1991.

8. (a) Chattoraj, M.; Paulson, B.; Shi, Y.; Closs, G. L.; Levy, D. H. *J. Phys. Chem.* 1994, 98, 3361; (b) Chattoraj,

M.; Bal, B.; Closs, G. L.; Levy, D. H. *J. Phys. Chem.* **1992**, *95*, 9666.

9. Zimmerman, H. E.; Goldman, T. D.; Hirzel, T. K.; Schmidt, S. P. *J. Org. Chem.* **1980**, *45*, 3934.

10. (a) Tung, C. H.; Zhang, L. P.; Li, Y.; Cao, H.; Tanimoto, Y. *J. Am. Chem. Soc.* **1997**, *119*, 5348; (b) Agyin, J. K.; Timberlake, L. D.; Morrison, H. *J. Am. Chem. Soc.* **1997**, *119*, 7945.

11. Warrener, R. N. *Eur. J. Org. Chem.* **2000**, 3363.

12. Warrener, R. N.; Pitt, I. G.; Butler, D. N. *J. Chem. Soc., Chem. Commun.* **1983**, 1340.

13. Warrener, R. N.; Abbenante, G.; Kennard, C. H. L. *J. Am. Chem. Soc.* **1994**, *116*, 3645.

14. (a) Chiou, N. R.; Chow, T. J.; Chen, C. Y.; Hsu, M. A.; Chen, H. C. *Tetrahedron Lett.* **2001**, *42*, 29; (b) Chow, T. J.; Hon, Y. S.; Chen, C. Y.; Huang, M. S. *Tetrahedron Lett.* **1999**, *40*, 7799.

15. (a) Hieber, W.; Sedlmeier, J. *Chem. Ber.* **1954**, *87*, 789; (b) Arnold, D. R.; Trecker, D. J.; Whipple, E. B. *J. Am. Chem. Soc.* **1965**, *87*, 2596.

16. (a) Salomon, R. G. *Tetrahedron* **1986**, *42*, 5753; (b) Chebolu, R.; Zhang, W.; Galoppini, E.; Gilardi, R. *Tetrahedron Lett.* **2000**, *41*, 2831.

17. (a) Cava, M. P.; Deana, A. A.; Muth, K. *J. Am. Chem. Soc.* **1959**, *81*, 6458; (b) Mcomie, J. F. W.; Perry, D. H. *Synthesis* **1973**, 416.

18. (a) Ahmad, N.; Levison, J. J.; Robinson, S. D.; Uttley, M. G. *Inorg. Synth.* **1974**, *15*, 45; (b) Kumar, K.; Tepper, R. J.; Zeng, Y.; Zimmt, M. B. *J. Org. Chem.* **1995**, *60*, 4051.

19. Chou, P. T.; Chen, Y. C.; Yu, W. S.; Chou, Y. H.; Wei, C. Y.; Cheng, Y. M. *J. Phys. Chem. A* **2001**, *105*, 1731.

20. Oevering, H.; Paddon-Row, M. N.; Heppener, M.; Oliver, A. M.; Cotsaris, E.; Verhoeven, J. A.; Hush, N. S. *J. Am. Chem. Soc.* **1987**, *109*, 3258.

21. Kroon, J.; Verhoeven, J. W.; Paddon-Row, M. N.; Oliver, A. M. *Angew. Chem., Int. Ed. Engl.* **1991**, *30*, 1358.

22. The distance was measured from the central bond of naphthalene to the mid-point of a line connecting the carbonyl groups. It will be reduced to 13.5 Å if the bond distance was measured to the ethylene double bond.

23. (a) Paddon-Row, M. N. *Acc. Chem. Res.* **1994**, *27*, 18; (b) Paddon-Row, M. N.; Shephard, M. J.; Jordan, K. D. *J. Phys. Chem.* **1993**, *97*, 1743; (c) Jordan, K. D.; Paddon-Row, M. N. *Chem. Rev.* **1992**, *92*, 395.

24. Lokan, N.; Paddon-Row, M. N.; Smith, T. A.; Rosa, M. L.; Ghiggino, K. P.; Speiser, S. *J. Am. Chem. Soc.* **1999**, *121*, 2917.

25. For example, see: Closs, G. L.; Calcaterra, L. T.; Green, N. J.; Penfield, K. W.; Miller, J. R. *J. Phys. Chem.* **1986**, *90*, 3673.

26. For example, see: (a) Oevering, H.; Paddon-Row, M. N.; Heppener, H.; Oliver, A. M.; Cotsaris, E.; Verhoeven, J. W.; Hush, N. S. *J. Am. Chem. Soc.* **1987**, *109*, 3258; (b) Paddon-Row, M. N.; Oliver, A. M.; Warman, J. M.; Smit, K. J.; de Haas, M. P.; Oevering, H.; Verhoeven, J. W. *J. Phys. Chem.* **1988**, *92*, 6958.